Effect of unloading rate on surface crack growth during underload cycles in X-65 pipeline steel exposed to near-neutral pH environments

by

Jerome Ang

A thesis submitted in partial fulfilment of the requirements for the degree of

Master of Science

in

Materials Engineering

Department of Chemical and Materials Engineering

University of Alberta

Abstract

Effect of unloading rate on surface crack growth during underload cycles in X-65 pipeline steel exposed to near-neutral pH environments

This thesis has studied the crack growth behaviour of fully-coated, partially-coated, and fully-exposed semi-elliptical cracks immersed in a near-neutral pH environment with an applied cathodic potential. The effects of adding a one-hour monotonic hold and waveform shape were explored.

The addition of a one-hour hold was shown to cause crack arrest at the surface of the cracks for fully-coated specimens due to room-temperature creep. Similarly, crack arrest was observed in the fully-exposed specimen due to room-temperature creep, anodic dissolution, and hydrogen-enhanced localized plasticity. Enhanced crack growth from increased hydrogen concentrations at the crack tip due to crack morphology and applied cathodic potentials may overcome retardation effects expected from a static hold.

Rapid unloading was found to enhance crack growth due to enhanced hydrogen segregation associated with reduced screw dislocation mobility and reduced time for hydrogen diffusion out of the fracture process zone during elastic lattice relaxation. Greater hydrogen effects were observed in the depth compared with the surface of the cracks due to differences higher crack tip stresses. Sufficiently high unloading rates may allow for cracks to enter an active growth state.

Pipeline operators can optimize their hydrostatic test programs to minimize the amount of potential crack growth during operations and fitness-for-service testing. A static hold at maximum operating pressure can retard subsequent crack growth in the length direction, especially following a significant depressurization-repressurization event. However, crack growth may still occur in the depth direction. Further, the lifetime of the pipelines can be extended by reducing the number of rapid depressurization events.

Acknowledgements

First and foremost, I would like to extend my utmost thanks to Dr. Weixing Chen for his immense patience and mentorship during my cyclic learning throughout the entire process, as well as all of the opportunities he has kindly given in the time I have spent with him. The multiple discussions to clear up new questions has been key to fostering a sound understanding of near-neutral pH cracking, as well as general concepts related to the broader field of materials engineering. I cannot count the number of times that he has refocused my attention to the bigger picture to deepen my understanding of how a crack propagates or how hydrogen will preferentially segregate. Even if he is abroad for conferences or busy on the weekends, he still manages to set aside some time to meet or provide key feedback. I would not have come close to developing the skills and knowledge I now have without his help and support. Thank you.

Many thanks to the members in the examination committee, Dr. Hao Zhang and Dr. Doug Ivey. Thank you both for your input in ensuring that my work is complete and my ideas are refined. Dr. Zhang has been a great help with guiding my understanding of hydrogen diffusion and its effects on enhancing crack propagation. Dr. Ivey has been incredibly helpful with his detailed feedback on the thesis and on characterization of my cracked specimens. I would also like to thank Dr. Reg Eadie for his guidance and fruitful discussions. His input during the group meetings have helped tremendously in clarifying my research direction and improving my experiments and results. Further, I would like to thank Dr. Tonya Wolfe, Dr. John Nychka, Scott Pavelich, Kevin Hodder, Chris Kirchen, and Kimberley Meszaros for developing critical thinking and problem solving skills in my time with the MAT E 465 class. Not only was this a great opportunity to directly work with undergraduate students, but the classes were helpful with taking a broader perspective on my research.

I would like to thank Devin Engel for help with experimental setup, continual mentorship, fruitful discussions, and plenty of his support (both research-related and otherwise). You always know how to make working in the lab a little more lighter and have improved and maintained the experimental setups on innumerable occasions. Mengshan Yu has also been a great guide with many discussions and his mentorship, and for setting the foundation for his CP work and variable amplitude loading with the CT specimens. Zeynab Shirband has helped with corrosion fundamentals, as well as with experimental setup of the CP system. Xing Xiao has been a mentor for the fundamentals for hydrogen diffusion and modeling of hydrogen assisted cracking. Thank you for your guidance with modeling hydrogen concentrations ahead of the crack tip. Discussions with Olayinka Tehinse has allowed for a deeper understanding of variable amplitude loading and the effect of loading waveform on crack growth behaviour. You are always

a joy to work with in the lab. Jiaxi Zhao has been a tremendous help with validation and modeling as well as helpful discussions regarding the influence of stresses on crack growth as well as considering the effect of T stress and crack tip constraint. I would also like to thank Zhezhu Xu, Keqiang (Cooper) Hu, and Ray Li for their helpful input for experimental setup.

The many experiments would not have been possible for the technical staff: Herb Green, Bob Smith, James McKinnon, Clark Bicknell, Dave Parlin, and Walter Boddez. Thank you all for creating test specimens with quick turnaround times and also for working with our group to create and improve our solution cells. Nathan Gerein has been instrumental in our SEM work – it is always a great pleasure to discuss how we can improve our characterization methods for our testing. I would also like to take the time to thank Kevin Heidebrecht, Lily Laser, Marion Pritchard, and Jack Gibeau for keeping things running smoothly and always being there for a myriad of requests.

Of course, I would like to thank my parents, Lawrence and Eugenia Ang, as well as my siblings Marc and Joyce for their continual support during my ups and downs during my research. You always found a way to pull me out of my head and look at things from another perspective whenever I had a writing or research block. I would also like to thank Erica and Mikey for being the best possible kinds of distractions and for being an inspiration to continue with my research. The list of people to thank would be incomplete without mentioning Steffen, Lydia, Thomas, Jordan, Jake, Ryan, Sean, Lindsay, Bryar, Will, Tylor, and Mike, to name a few – you have all been a breath of fresh air to get my mind off of research and to recharge my batteries whenever I was running on empty. Finally, I could not have been able to complete this research without Rose – you have not only been able to keep my head above water, but have helped me keep my focus and see this work through to completion. I cannot thank you enough.

I would like to take the time to thank the industrial sponsors. Specifically, Karina Chevil from TransCanada Pipelines Ltd., and Colin Scott and Lyndon Lamborn from Enbridge Pipelines Inc. Working with you have been a great opportunity to see how our research fits in with the greater industrial context. Further, I would like to thank the Natural Science and Engineering Research Council of Canada (NSERC) and Pipeline Research Council International (PRCI) for their support. Additionally, I would like to thank the NSERC CGS-M, and QEII Scholarships for their financial support.

Sunil Patel and Steven Gunn developed this LaTeX template. Thank you for your contribution in the formatting of this thesis.

Contents

List of Tables

List of Figures

Abbreviations

AIDE	**A**dsorption **I**nduced **D**islocation **E**mission
CA	**C**onstant **A**mplitude
CF	**C**orrosion **F**atigue
CGR	**C**rack **G**rowth **R**ate
CP	**C**athodic **P**rotection
CTOD	**C**rack **T**ip **O**pening **D**isplacement
EAC	**E**nvironmentally **A**ssisted **C**racking
EDM	**E**lectrical **D**ischarge **M**achining
EMAT	**E**lectro **M**agnetic **A**coustic **T**ransducer
EPFM	**E**lastic **P**lastic **F**racture **M**echanics
FPZ	**F**racture **P**rocess **Z**one
GND	**G**eometrically **N**ecessary **D**islocations
HAC	**H**ydrogen **A**ssisted **C**racking
HE	**H**ydrogen **E**mbrittlement
HEDE	**H**ydrogen **E**nhanced **DE**cohesion
HELP	**H**ydrogen **E**nhanced **L**ocalized **P**lasticity
ILI	**I**n-**L**ine **I**nspection
LEFM	**L**inear **E**lastic **F**racture **M**echanics
MFM	**M**icrostructural **F**racture **M**echanics
NNpH	**N**ear **N**eutral **pH**
OCP	**O**pen **C**ircuit **P**otential
RTC	**R**oom **T**emperature **C**reep
SCC	**S**tress **C**orrosion **C**racking
SEM	**S**canning **E**lectron **M**icroscopy
SGP	**S**train **G**radient **P**lasticity

SMYS	**S**pecific **M**inimum **Y**ield **S**tress
UTS	**U**ltimate **T**ensile **S**tress
VA	**V**ariable **A**mplitude
YS	**Y**ield **S**tress

Symbols

a	crack depth	m
c	crack length	m
C	Paris Law coefficient	$\mathrm{N\,mm^{3/2}}$
f	loading frequency	Hz
ΔK	stress intensity range	$\mathrm{MPa}\sqrt{m}$
K_{IC}	mode I critical fracture toughness	$\mathrm{MPa}\sqrt{m}$
K_{IH}	mode I threshold fracture toughness value for a hydrogen environment	$\mathrm{MPa}\sqrt{m}$
K_{ISCC}	threshold fracture toughness value for stress corrosion cracking	$\mathrm{MPa}\sqrt{m}$
K_{max}	maximum stress intensity	$\mathrm{MPa}\sqrt{m}$
k_t	stress concentration factor	-
m	Paris Law exponent	-
R	stress ratio	-
r_p	plastic zone	m
γ	factor representing the influence of the corrosion environment on the CGR	-
ρ	radius of curvature at the tip of the blunt crack	m
σ_a	applied stress	MPa
$\frac{da}{dN}$	depth crack growth rate	m/s
$\frac{dc}{dN}$	surface crack growth rate	m/s
$\frac{\Delta K^{\alpha} \cdot {K_{max}}^{\beta}}{f^{\gamma}}$	combined factor	$\mathrm{MPa^3\,m^{1.5}\,s^{0.1}}$

Chapter 1

Introduction

1.1 Introduction

Within Canada, there is more than 840,000 km of transmission, gathering, and distribution pipelines [1]. Of these, approximately 117,000 km of large-diameter transmission lines exist with about 73,000 km being federally regulated [1]. Pipelines act as a key delivery system for Canadians to heat their homes and for fuel used in travel by cars, bus, ship, train, and air [1]. In addition to delivering fuel, oil and gas act as a critical feedstock in creating household products such as toiletries, electronics, and clothing [1]. Furthermore, the oil and gas sector contributes to nearly 11 percent of Canada's GDP, providing Canadians with jobs and economic prosperity [1].

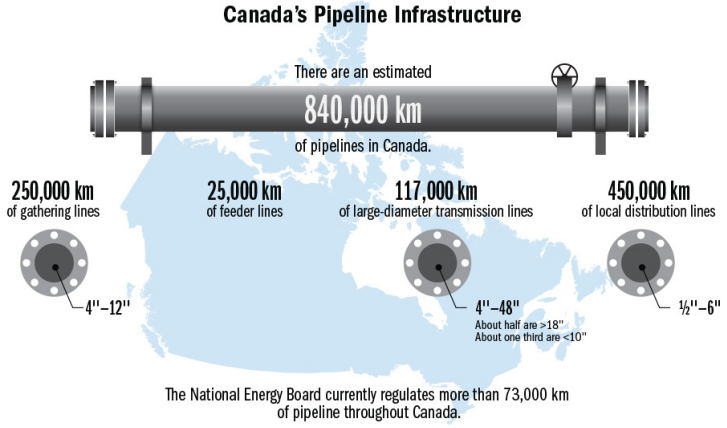

Figure 1.1: Approximate quantity of pipelines in Canada, broken down by gathering, feeder, transmission, and distribution lines [1].

In order to maintain the integrity of liquids and gas pipelines, it is critical to understand the various threats that can compromise safe transport. Some major threat categories include cracking, corrosion, and deformations. While a large body of work has been devoted to each individual threat category, much work is left to fully understand the interactions between defect types and their respective mechanisms. Environmentally-assisted crack growth is one of many threats that remains an integrity challenge to pipelines. The multivariate nature of corrosion interacting with localized stresses at a crack within a susceptible material poses a complex and complicated problem to the oil and gas industry. This thesis will act to address one subset of environmentally-assisted cracking: specifically, the depressurization rate during near-neutral pH corrosion fatigue. The following section outlines the structure of the thesis.

1.2 Thesis Overview

- Chapter 2 will provide an overview of near-neutral pH corrosion fatigue (NNpHCF), as well as the relevant mechanics and mechanisms associated with fatigue crack propagation. Time- and cycle-dependent fatigue crack growth will be discussed, as well as the pertinent variables that affect cracking.

- Chapter 3 will outline the experimental methods taken to better understand the time- and cycle-dependent fatigue crack growth phenomena specific to the unloading rate during underload cycles for semi-elliptical surface cracks in X-65 pipeline steel.

- Chapter 4 will focus on chemical contributions and hydrogen damage mechanisms associated with time-dependent crack growth, specifically the effect of adding a static hold to constant amplitude loading.

- Chapter 5 will focus on the effect of the unloading rate on crack growth during underload cycles of pipeline steel undergoing NNpHCF. Both time- and cycle-dependent crack growth will be discussed.

- Chapter 6 will provide the major conclusions taken from the work, as well as recommendations and potential future work for understanding and mitigating NNpHCF.

Chapter 2

Background

2.1 Overview

This chapter will act as a broad, but not exhaustive, review of near-neutral pH environment-assisted cracking (NNpHEAC). The aim of this chapter is to categorize the parameters that affect crack growth in pipeline steels exposed to near-neutral pH solutions, with a focus on strain rate and hydrogen-assisted cracking. A brief overview of NNpHEAC is shown, as well as background on inert fatigue and environmentally-enhanced fatigue cracking. Following the SCC 'triangle', three broad categories affecting NNpHEAC will be discussed: mechanical loading, corrosive environments, and susceptible materials. These three variables are discussed separately but act synergistically to drive crack growth. Further, key mechanisms are discussed herein: the environmentally short crack effect, anodic dissolution, hydrogen-assisted damage, and room temperature creep.

2.2 Introduction to Near-Neutral pH Environmentally- Assisted Cracking

2.2.1 Brief History of Environmentally-Assisted Cracking

As early as 1950, Harwood conducted an early study on stress corrosion cracking and summarized the effects of stress on localized damage in a corrosive environment [2, 3]. In 1965, the first reports of stress corrosion cracking (SCC) in high pH environments

arose [4]; however, a new form of "SCC" called near-neutral pH stress corrosion cracking (NNpHSCC) was discovered in Canada in 1986 [5]. Not only were the crack morphologies different between the high pH and near-neutral pH cracking types, but the mechanisms driving crack growth differed as well. Some distinctions between solution chemistry and crack characteristics from each type of SCC are summarized in Table 2.1; Beavers and Harle also contrast the two types of SCC [6]. Please note that from here on, we will refer to NNpHSCC as near-neutral pH corrosion fatigue (NNpHCF) in order to highlight key mechanistic differences between classical, high pH SCC and NNpHCF. High pH SCC has crack growth as a result of film formation and subsequent film rupture under sufficiently high stresses; however, no crack growth has been observed for NNpHCF cracks under monotonic loading [6]. Additional information for high pH SCC is discussed by Beavers [4] and Lu et al. [7, 8]. Further details regarding NNpHCF are discussed in the below sections.

Table 2.1: Comparison between high pH and near-neutral pH stress corrosion crack and solution characteristics.

Variable	**Near-Neutral pH [9]**	**High pH [10]**
pH	5.5 to 7.5	9 to 13
Electrolyte	dilute HCO_3^-	carbonate / bicarbonate
Crack Width	wide	narrow
Cracking Mode	transgranular	intergranular
Aspect Ratio	high length:depth ratio	typically semi-circular
Branching	little	typically branched
Crack Orientation	Longitudinal	Longitudinal
Crack Wall Corrosion	Yes	No

Some factors that are related to SCC failuresare the proximity to a pump/compressor station, the magnitude of operating stresses, and coating types. Further details regarding these parameters are shown in Table 2.2. In a study by Parkins and Beavers, it is noted that SCC is typically associated with areas of low cathodic current flow at the pipe surface [11]. Further details and statistics of failures are shown in a study by Batte et al. [12, 13].

2.2.2 Pressure Fluctuations in Pipelines

Pipelines used in the transmission of both oil and gas products undergo several pressure fluctuations during regular operations. These pressure fluctuations can interact with

Table 2.2: Factors linked to the occurrence of near-neutral pH and high pH SCC [12].

Criterion	**Near-Neutral pH SCC**	**High pH SCC**
Distance downstream from compressors	70% are within 20 miles	90% are within 20 miles
Operating stress	95% are at $>$ 60% SMYS	85% are at $>$ 60% SMYS
Coating type	40% in asphalt lines, 35% in tape-wrap lines, 20% in uncoated lines	70% in coal tar lines, 25% in tape-wrap lines

stress raisers such as manufacturing defects, third-party damage, and corrosion attack to initiate a crack. Subsequent crack growth can become a leak or rupture threat and may cause significant environmental and economic damage. Generally, there are 3 types of pressure fluctuations: underload, mean load, and overload pressure fluctuations [9, 14]. Typical pressure data for each type of pressure fluctuation are shown in Figure 2.1. Additionally, some key differences between the three loading types are summarized in Table 2.3.

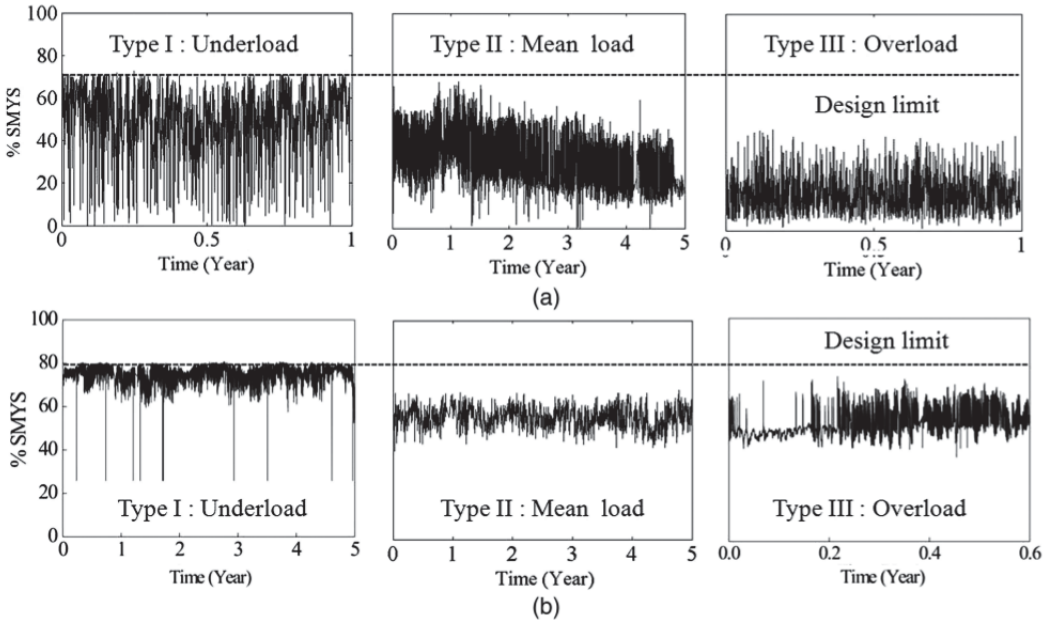

Figure 2.1: Classification of pressure fluctuation spectra: (a) oil pipeline spectra; (b) gas pipeline spectra [14].

Because underload spectra are most severe due to the relatively high maximum pressures and large amplitudes of pressure fluctuations, this aggressive loading type has been most studied for pipeline steels subjected to NNpHCF [9]. A schematic of the pressure

Table 2.3: Types of pressure fluctuations observed in pipelines and their typical characteristics [9].

	Type I Underload	**Type II Mean Load**	**Type III Overload**
Location	< 30km downstream of compressor/pump stations	Further down from compressor/pump stations	At or near suction sites
Pressure	Max pressure at or near design limit	Lower mean pressure	Relatively lower mean pressure
Fluctuations	Only allowed to be lower than design limit	Some underloads, some overloads (lower than design limit)	Pressure spikes common

variation over time for an underload-type waveform is shown in Figure 2.2. A "minor cycle" would be any pressure fluctuation acting below the threshold for cracking, i.e. the mechanical driving force would be insufficient to propagate the crack, even under environmentally-assisted conditions [15].

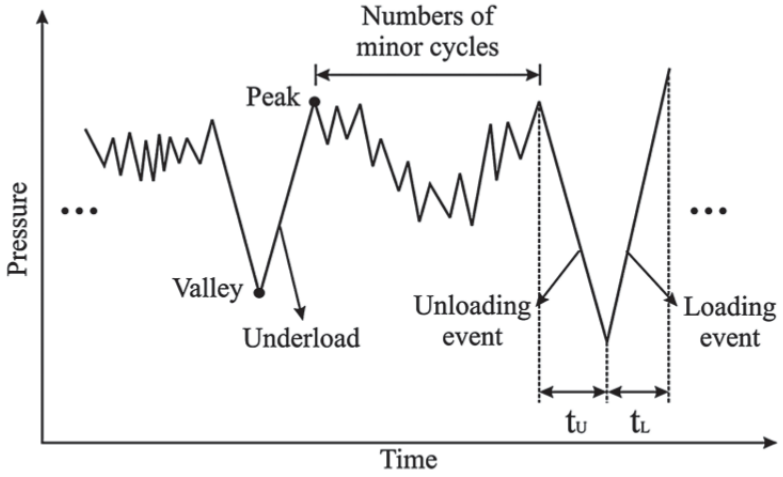

Figure 2.2: Schematic illustration of an underload spectrum [14].

Key differences between underload pressure fluctuations found in oil and gas pipelines are summarized in Table 2.4. One relevant parameter is the stress ratio R, which is the ratio of the minimum stress over the maximum stress. The loading frequency shown in Table 2.4 represents the rate at which pipelines increase pressure, assuming a symmetrical triangular waveform; similarly, the unloading frequency represents te rate at which pipelines decrease pressure. The maximum stress intensity factor $K_{\max}$ is related to the maximum pressure that the pipeline experiences. Likewise, the range of stress intensity factor ΔK is related to the stress ratio and the range of pressure fluctuations.

Crack growth is generally lower in gas pipelines than in oil pipelines due to typically less underloads in a given year and slower pressure changes in gas pipelines. However, due to the compressibility of gases, rupture consequences can be severe and the integrity threat of ductile running fractures should be considered.

Table 2.4: Characteristics of underload pressure fluctuations observed in oil and gas pipelines.

	Oil Pipelines	**Gas Pipelines**	**Ref**
Stress Ratio R	Lower R	Higher R	[9]
# Underloads per Year	537	8	[14, 16]
Loading Frequency f_L [Hz]	5.1×10^{-6} – 1.0×10^{-2}	1.3×10^{-6} – 5.3×10^{-6}	[16]
Unloading Frequency f_U [Hz]	6.9×10^{-6} – 1.0×10^{-1}	1.3×10^{-6} – 9.2×10^{-5}	[16]
# of minor cycles	$0 \sim 26$	$0 \sim 37$	[14, 16]
$K_{\max}$ [MPa $\mathrm{m}^{0,5}$]	11.6–22.5	23.1–24.6	[14]
ΔK [MPa $\mathrm{m}^{0,5}$]	3.3–13.7	3.4–4.3	[14]
Rate of Pressure Change	Higher	Lower	[9]

2.3 Fatigue

Pressure fluctuations and dynamic loading will act as a source of damage accumulation in a stressed material. Fatigue damage in an inert environment is discussed here, followed by general corrosion fatigue principles. Finally, fatigue during NNpHCF is discussed.

2.3.1 Inert Fatigue

The three main regimes of crack growth for inert fatigue is shown in Figure 2.3. Note that da/dN represents the crack growth rate per pressure cycle. It is important to note that crack initiation and early-stage growth (Regime A) actually consist of two parts: microstructural crack growth and physically short crack growth, as shown schematically in Figure 2.4. As seen in Figure 2.4, ΔK_{th} represents the threshold stress intensity factor range, below which a crack will not propagate. Once a crack is initiated, non-continuum mechanisms govern crack growth, especially related to the microstructure, mean stress, and environmental conditions. Since linear elastic fracture mechanics (LEFM) principles begin to break down at these size scales, microstructural fracture mechanics (MFM) and elastic-plastic fracture mechanics (EPFM) must be considered [17]. Table 2.5 contrasts the various crack regimes. As summarized by Davidson, a "small" surface crack will have both its length and depth small in comparison to the relevant length scale; alternatively, a "short" surface crack will only be small in the depth, for example [18].

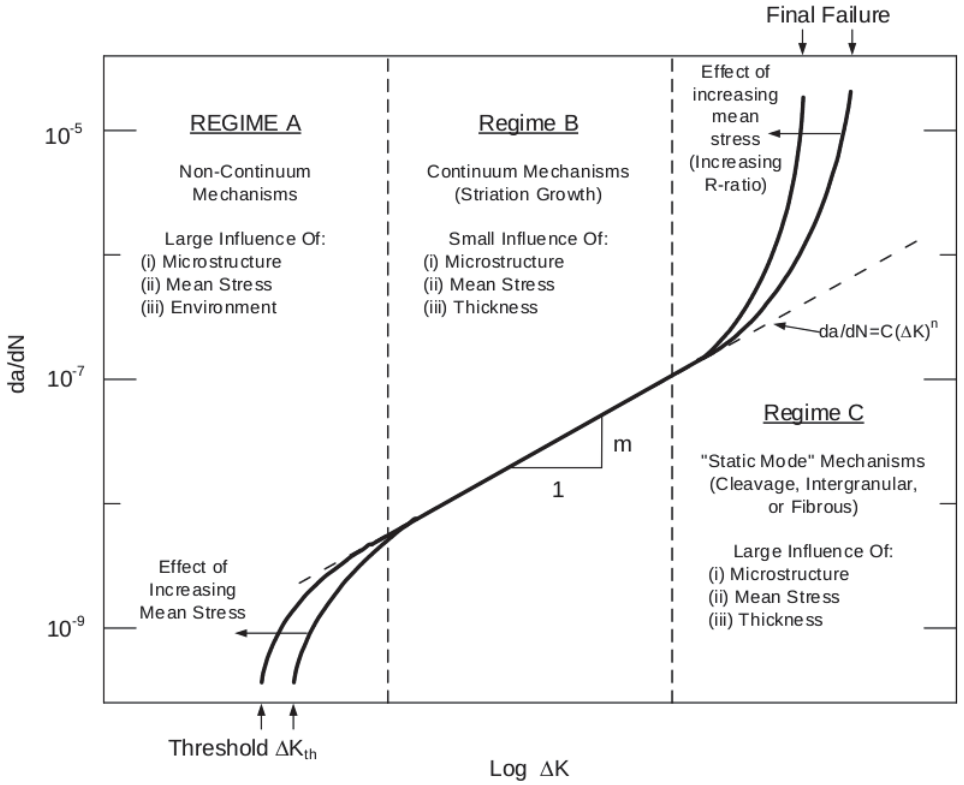

Figure 2.3: General fatigue crack growth (da/dN) behavior as a function of ΔK. The influence of mean stress, microstructure, environment, thickness, and R-ratio are shown [19].

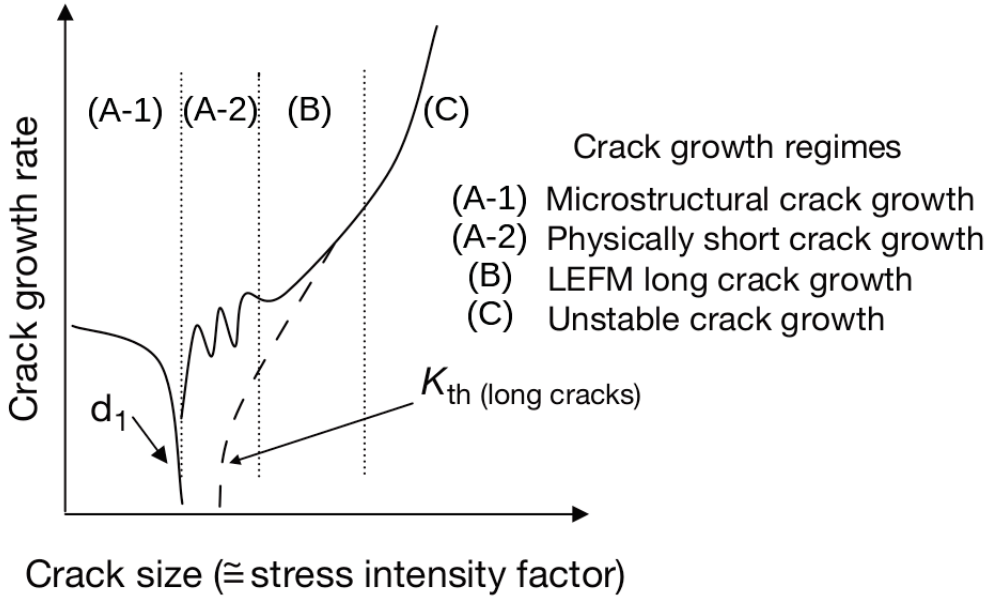

Figure 2.4: Fatigue crack growth rate as a function of crack size. Adapted from Akid (2010) [20].

Table 2.5: Three distinct regimes of long cracks, physically small cracks, and microstructurally short cracks: each type of crack requires its own form of mechanics to characterize propagation behavior (a is crack length and r_p is plastic zone size), adapted from Miller [21].

	Microstructurally Small Crack	**Physically Small Crack**	**Long Crack**
Typical Size	$a \sim 1\,\mu m$	$a \sim 0.1\,mm$	$a \sim 10\,mm$
	$a <$ 1 grain	$a <$ 10 grains	$a >$ 100 grains
Stress	High	High	Low
Mechanics	MFM	EPFM	LEFM
	Mode II and III	Modes I, II, and III	Mode I (Stage II)
Crack Type	Stage I (Shear) Crack	Stage II Crack	Stage II Crack
a/r_p ratio	Low (< 1)	Intermediate	High ($>> 1$)

A schematic of the development of a crack from a free surface is shown in Figure 2.5, where the growth behavior is shown for each stage of growth.

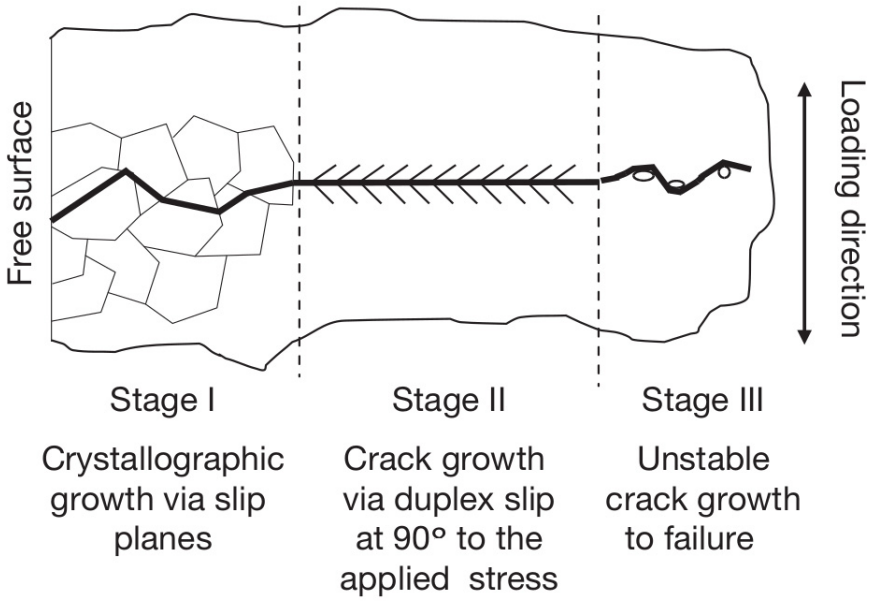

Figure 2.5: Schematic illustrating different fatigue crack growth stages [20].

The main corollary from the above figures and tables is that depending on the size of the crack, fatigue crack growth behavior will change. Taylor and Knott discuss short crack growth under cyclic loading, denoting two critical lengths: the first below which crack growth rate is unaffected by the crack length (Stage I), and the second where the microstructure is largely ineffective in impeding crack growth (Stage II) [22]. Essentially, the two critical crack lengths would define the boundaries between microstructurally-

and mechanically-controlled crack growth, with a transition period between [22]. This thesis will focus primarily on Stage II crack growth.

A microstructurally short crack will have its growth heavily influenced by microstructure, environment, and stress ratio [20]. As the crack grows, its plastic zone size will also increase and therefore any microstructural barriers will offer less resistance to the advancing crack front [21]. The crack speed will fluctuate as microstructural barriers are encountered and eventually overcome. Upon reaching a critical size, the crack will become insensitive to microstructural barriers and develop two mutually perpendicular shear planes, based on the theory proposed by Tomkins [23].

Once the crack is sufficiently large (i.e. less hindered by microstructural barriers due to the larger plastic zone size), the crack can be classified as physically small. Here, elastic-plastic fracture mechanics (EPFM) dominates since the stress required for propagation may be on the order of the bulk yield stress [21]. Similarly, even if the stress required for propagation is significantly lower than the bulk yield stress, the plastic zone would be of a comparable size to the crack itself and thus the assumption of small-scale yielding will no longer be applicable [21]. Fatigue resistance, according to Miller, is primarily related to the difficulty of a Stage I crack becoming a Stage II crack [21]. Kim et al. determined the fatigue threshold values for X65, X70, and X80 steels for a frequency of 20 Hz and a load ratio of 0.1 in compact tension specimens [24]. Further details regarding crack tip mechanics and the stress states ahead of a crack tip will be discussed in a later section.

Eventually, the crack grows to a size sufficiently large ($a/r_p >> 1$ [21]) such that linear elastic fracture mechanics dominates (LEFM). At this point, the crack length is much larger than the plastic zone size and the majority of the crack-tip fracture process zone (FPZ) behaves elastically during crack propagation. Akid defines this boundary at $a/r_p \approx 50$ [20]. The Paris-Erdogan equation is commonly used in describing stable Stage II crack growth: [25].

$$\frac{da}{dN} = C(\Delta K)^m \tag{2.1}$$

where $\Delta K = K_{\max} - K_{\min}$, and A and m are material-, temperature-, microstructure-, and stress-ratio-dependent constants. Values of m are typically in the range of $2 \leq m \leq 5$ [20]. A study by Tiku et al. [26] uses $C = 4.68 \times 10^{-13}\,\mathrm{N\,mm^{3/2}}$ and $m = 2.91$,

noting that these constants applied to electric resistance welded (ERW) pipe for axially oriented flaws result in fatigue lives approximately 2 to 3 times greater than fatigue lives calculated using BS 7910 Paris Law parameters.

Once the crack is a mechanically-driven Stage-II crack, the propagation mode changes from a primarily shear-driven mechanism (in Stage-I) to striation growth. Davidson and Lankford provide a good overview on the mechanisms behind striation formation [27]. Basically, the crack generates a sufficiently large plastic zone and stress concentration such that microscopic plastic flow is achieved on both sides of the crack tip at 45 degrees, creating ridges otherwise referred to as striations. Due to rising and falling stresses, the crack tip undergoes cycles of blunting and resharpening as a result of plastic flow and striation growth. Early researchers such as Pelloux and Forsyth showed that one striation formed on each loading cycle [27]. However, subsequent experimental and numerical research have shown that it may take tens to thousands of cycles to generate a single striation, depending on local stress levels [27].

Grinberg et al. demonstrated that striation spacing can be completely independent of ΔK during near-threshold growth [28]. The minimum striation spacing was found to be approximately 100 nm, regardless of material [28]. Other studies agreed with these findings, including for Al and its alloys, Mg, Ni, Ti alloys, and for many steels [27]. During striation growth, the local strain rate and therefore striation spacing is expected to vary by at least a factor of 2 due to variations in crack tip sharpness [27]. Generally, it is possible for striation spacing to exceed measured crack growth rates by several orders of magnitude, especially for near-threshold crack growth [27].

Mughrabi provided a detailed summary on microstructural fatigue mechanisms [29]. Fatigue damage can be simply described as irreversible slip events. Some key mechanisms for cyclic slip irreversibilities include cross slip of screw dislocations, mutual annihilation of dislocations, random to-and-fro glide of dislocations (leading to surface roughening), and the slip-asymmetry in BCC metals [29]. A large body of work has related cyclic slip irreversibility to slip plane asymmetry. According to Mughrabi, slip plane asymmetry is related to incompatible shape changes of neighboring grains due to glide of screw dislocations on different planes [29]. While Magnin and Driver studied the asymmetry in slip systems in BCC iron alloys [30], it is important to note that the asymmetry effect would be less pronounced in polycrystals due to grain misorientation. In single crystals,

however, slip asymmetry is more pronounced at higher strain rates [30]. Magnin et al. also observed the formation of fatigue-induced shear bands, which had a different structure than classical persistent slip bands [31]. These shear bands may be important at lower temperatures and / or higher strain rates, since persistent slip band formation is less favorable under these conditions [31]. Magnin et al. also discuss slip-twinning interactions under monotonic and cyclic deformation in BCC stainless steels [32].

Since some plastic deformation occurs at the crack tip, it is important to consider the flow stress of a material. The flow stress is defined as the stress required for plastic flow to continue or the stress required to move a significant number of dislocations [33]. The flow stress has athermal and thermal components: the internal stress (related to long-range interactions between, for example, forest dislocations) and the effective stress (related to short range interactions such as moving a dislocation through the atomic lattice) [30]. At lower strain rates, the flow stress is mainly governed by the internal stress component [30]. Because short range interactions (and therefore the effective stress) is related to thermally-activated motion of screw dislocations, lower temperatures or high strain rates will hinder screw dislocation motion [30]. The strain rate dependence of screw dislocation mobility is significant in affecting crack growth during inert fatigue; as will be discussed in later sections, the effect of strain rate on crack growth can be further influenced by the presence of hydrogen.

2.3.2 Corrosion Fatigue

Figure 2.6 shows the differences between inert fatigue and environmentally-assisted fatigue in terms of da/dN with respect to ΔK. There is a clear acceleration due to environmentally-assisted crack growth, and further contributions from SCC-related mechanisms can lead to enhanced crack growth. As long as ΔK is greater than the threshold for cracking (represented as ΔK_O in Figure 2.6), crack initiation and growth will occur. Crack growth will follow a similar three-stage progress akin to inert fatigue as described in the previous section.

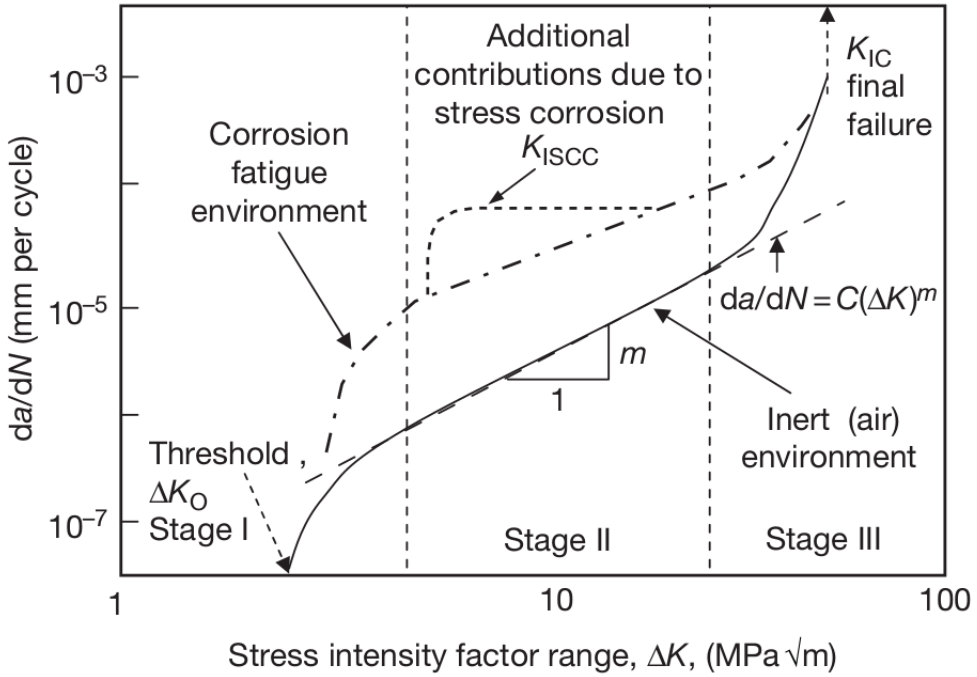

Figure 2.6: LEFM fatigue crack growth curves showing behaviour for air, corrosion fatigue, and corrosion fatigue plus stress-corrosion interactions [20].

During initiation and early-stage growth of corrosion fatigue cracks, several key events occur: surface film breakdown or local microgalvanic activity, pit growth, pit-to-crack transition, and cracking [20]. Figure 2.7 summarizes initiation and early-stage growth of defects under cyclic loading in a corrosive environment. Leis et al. also discuss crack initiation under corrosion fatigue conditions in further detail [34].

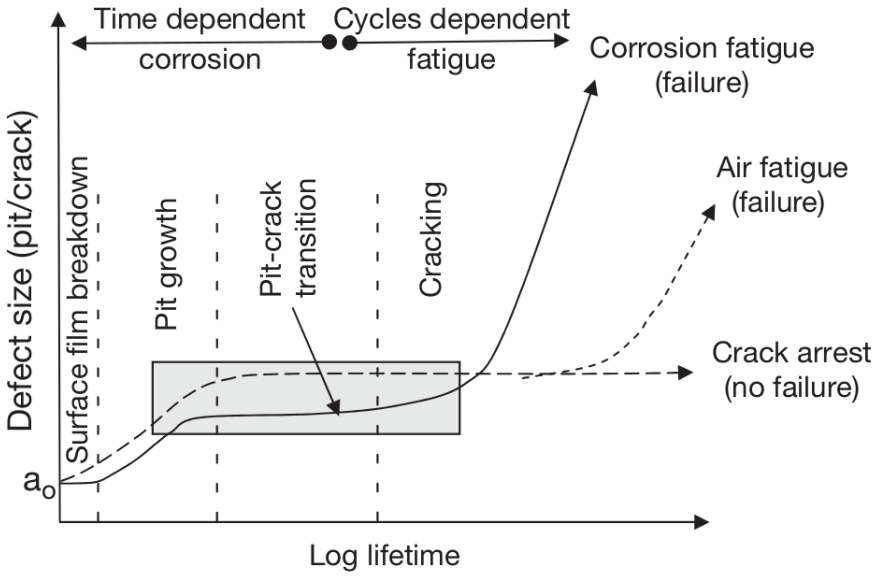

Figure 2.7: Schematic showing the behavior of fatigue cracks under air and corrosion fatigue conditions. Note that the stress level for the corrosion fatigue curve is less than the in-air fatigue limit of the material. Individual annotated regimes are for corrosion fatigue only. Reproduced from Akid, R. In *Effects of Environment on the Initiation of Crack Growth*; Van der Sluys, W. A., Piascik, R.S., Zawiercha, R., Eds.; ASTM STP 1298, **1997**, pp 1–17 [20].

Table 2.6 outlines the various damage regimes pertinent to early-stage corrosion fatigue, along with key factors that contribute significantly to each stage. Similar to crack growth in inert fatigue, the factors significantly impacting crack growth rates change as a corrosion fatigue crack grows from pit, transitions to a crack, and grows in length from an environmentally short crack to a physically short crack, and beyond into a sufficient length governed by Stage II growth and eventual failure as the stress intensity approaches the critical stress intensity for failure, K_Ic.

Comparing inert fatigue with corrosion fatigue, several analogs can be drawn between the two phenomena. The pit-to-crack transition in corrosion fatigue is similar to the critical length in inert fatigue whereby both mark an onset of mechanically-controlled crack growth. For a mechanically long crack, propagation rates will be generally higher

Table 2.6: Designated damage regimes relating to the early stages of corrosion fatigue. Adapted from Akid 2010 [20].

Process	**Influential Factors**
Pitting	Solution composition, pH, applied stress
Pit/crack transition	Pit shape / local pit environment, applied stress state
Environmentally short crack growth	Local crack tip chemistry, applied stress state
Physically short crack growth	Applied stress state (ΔK)

in a corrosion fatigue scenario than in inert fatigue, assuming no crack arrest occurs. Effectiveness of crack arrest sites can be expected to be reduced in corrosion fatigue, e.g. due to the dissolution of microstructural barriers.

In one study by Akid, it is noted that a simple linear damage summation approach is unsuitable for estimating fatigue life under corrosion fatigue conditions since early-stage crack growth can have profound effects on the overall lifetime of a specimen under corrosion fatigue conditions [35]. Considering the overall corrosion fatigue life, 90% of the crack life may be spent during initiation and early-stage growth [36]. The study by Leis et al. notes that the mechanism for environmental cracking will change as crack length varies through initiation, microcrack growth, and macrocrack growth [34]. Corrosion was noted to have most of its effects dominant during early-stage short crack growth in corrosion fatigue scenarios, and mechanical driving forces become predominant at longer crack lengths [37]. Miller and Akid provide a comprehensive review on the various stages of corrosion fatigue growth [38].

2.3.3 Near-Neutral pH Corrosion Fatigue

The general process of a pipeline becoming exposed to a near-neutral pH environment conducive to cracking is outlined in Figure 2.8. For NNpHCF to occur, the soil chemistry must allow for the formation of a near-neutral pH environment, sufficient residual stresses and pressure fluctuations must allow for localized crack formation, and a high enough lattice hydrogen content and sufficiently severe pressure fluctuations must allow for repeated crack growth. Additionally, a summary of key factors affecting NNpHCF are shown in Figures 2.9 and 2.10. Under static stresses, only stress corrosion cracking will occur and in a near-neutral pH environment, crack tip blunting as a result of anodic dissolution at the crack tip and room temperature creep will overcome crack tip

sharpening from potential hydrogen-assisted cracking. However, when sufficiently high pressure fluctuations exist, cyclic stresses will synergize with atomic hydrogen generated by corrosion of the metal and hydrogen-enhanced crack growth will occur.

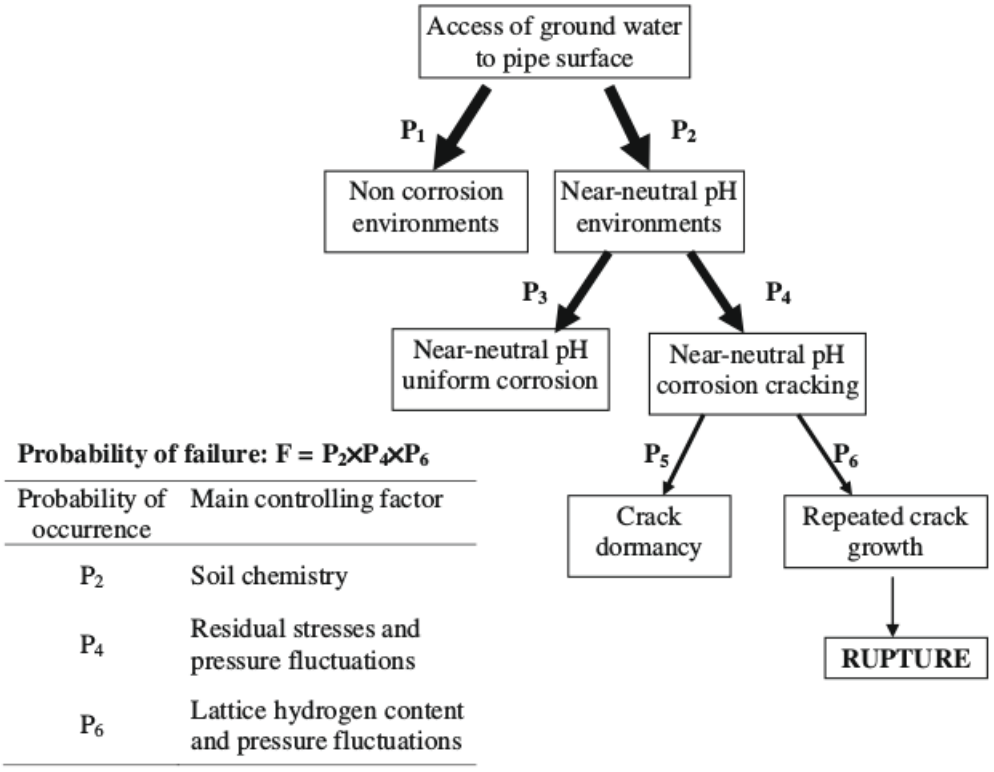

Probability of failure: $F = P_2 \times P_4 \times P_6$

Probability of occurrence	Main controlling factor
P_2	Soil chemistry
P_4	Residual stresses and pressure fluctuations
P_6	Lattice hydrogen content and pressure fluctuations

Figure 2.8: A schematic showing various events leading to the final rupture of pipeline steels exposed to near-neutral pH soil environments [39].

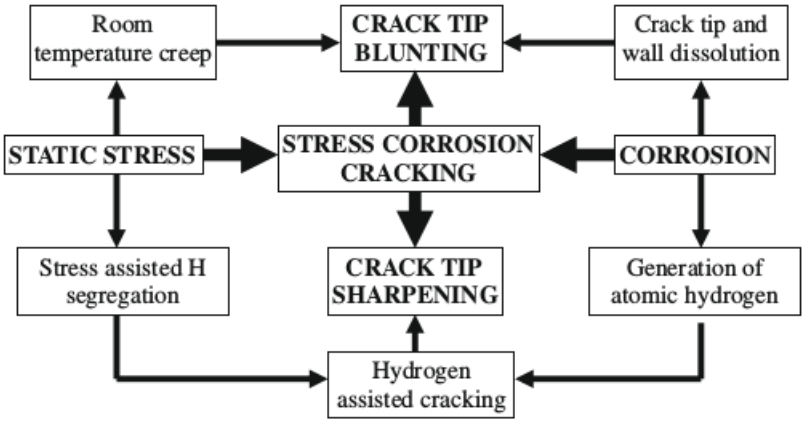

Figure 2.9: A schematic showing the competition between crack tip blunting and crack tip sharpening in pipeline steels exposed to near-neutral pH environments under constant stresses (conducive to SCC) [39].

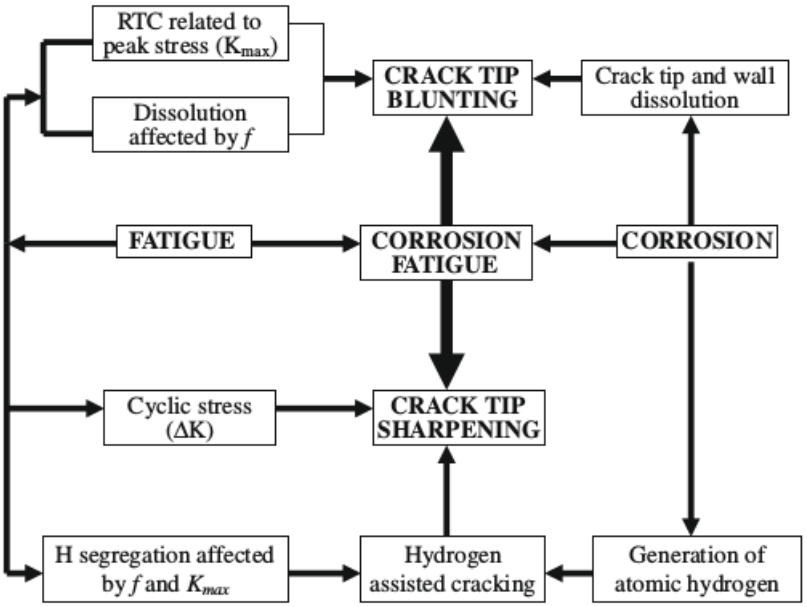

Figure 2.10: A schematic showing the competition between crack tip blunting and crack tip sharpening in pipeline steels exposed to near-neutral pH environments under cyclic loading conditions (conducive to corrosion fatigue) [39].

The bulk of this thesis will focus on the corrosion fatigue aspects, since NNpH cracking is primarily driven by dynamic loading. Mechanical loading (as a result of pressure fluctuations), corrosive environment (related to soil chemistry and hydrogen content), and susceptible materials (related to residual stresses and hydrogen diffusivity) are all key factors when considering the probability of failure to NNpHCF. Broadly speaking, multiple variables can manifest in competing mechanisms. For example, crack growth rates will be a function of crack tip blunting (due to dissolution and/or room-temperature creep) and crack tip sharpening (due to cyclic stresses and hydrogen-assisted cracking).

Per Gangloff's definitions, NNpHCF growth follows a time-cycle dependence; time-dependent processes such as hydrogen diffusion and anodic dissolution as well as cycle-dependent processes such as cumulative damage due to dynamic loading both act to sharpen and/or blunt the crack tip [40]. To account for both mechanical and environmental driving forces to crack growth, Chen and Sutherby developed the following equation, analogous to Paris-law crack growth [40]:

$$\frac{da}{dN} = A\left(\frac{\Delta K^{\alpha} K_{\max}^{\beta}}{f^{\gamma}}\right)^{n} + h \tag{2.2}$$

where A is a parameter related to hydrogen diffusion, $n = 3$, $\alpha = 0.67$, $\beta = 0.33$, and $\gamma = 0.033$, $\alpha + \beta = 1$, and h represents the crack growth rate in the depth by dissolution during Stage II crack growth [41]. Considering the work by Sadananda et al., a higher dependence of crack growth during NNpH cracking on ΔK compared with $K_{\max}$ suggests true corrosion fatigue behavior [42]. As stated in the review by Chen, hydrogen plays a key role in NNpHCF [9]. Thus, hydrogen-enhanced corrosion fatigue is the dominant cracking mode.

h can be experimentally determined and is typically one order of magnitude lower than the first term in Stage II crack growth [40]. Crack growth rates are typically on the order of $1 \times 10^{-8}\,\mathrm{mm\,s^{-1}}$ [10]. Further, crack velocities were found to be at least two orders of magnitude higher in constant displacement rate testing of precracked specimens when compared with the maximum crack velocity based on Faraday's law [6]. Crack growth rate due to pure anodic dissolution is shown as:

$$da/dt = i_a \cdot M/z \cdot F \cdot d \tag{2.3}$$

where da/dt is the crack velocity, i_a is the anodic current density, m is the atomic weight, z is the oxidation state of the solvated species, d is the density, and F is Faraday's constant [6]. The maximum crack velocity calculated by Equation 2.3 results in a crack velocity of approximately $4 \times 10^{-8}\,\mathrm{mm/s}$, based on a current density of approximately $100\,\mu\mathrm{A/cm^2}$ [6]. The study by Egbewande et al. showed that the overall crack growth rate during NNpHCF is much higher than the rate of dissolution [43]. King et al. also showed that the crack propagation rates does not support a primarily dissolution-based SCC mechanism [44]. Further, dissolution rates were found to be lower in dilute near-neutral pH solutions when compared with higher pH solutions [44].

No cracking was shown under constant load or constant displacement conditions for NNpH cracks, and cracking was observed only under cyclic loading [6]. Since crack growth does not occur under monotonic loading in NNpHCF, hydrogen-related crack tip sharpening mechanisms cannot act alone to resharpen an otherwise dormant crack [39]. Crack growth due to exposure to a near-neutral pH environment under monotonic loading has never been observed; possible crack initiation may still occur if the applied stresses are high or if the steel is dynamically loaded (as in slow-strain rate loading) [40,

45]. Crack resharpening is neither a purely fatigue- nor hydrogen-related phenomenon, but most likely a synergistic interaction of both [39]. Although contributions to crack growth from fatigue would be common to all cracks in a given system, contributions to crack growth from hydrogen-related mechanisms would be highly location-dependent [39]. Note that Gu et al. studied hydrogen-facilitated anodic dissolution using slow-strain rate testing of pipeline steels, showing that enhanced dissolution rates are not caused by this mechanism [46].

The work by Zhang et al. predicted a maximum crack growth rate of 1.1×10^{-7} mm/s at the surface, based on enhancement from galvanic coupling and/or residual stresses [41]. Chen and Sutherby showed that the dissolution rate was 1.4×10^{-9} mm/s, which is much lower than observed rates in the field [40]. Based on these results, it is likely that there is a high dissolution rate at the surface and a reduced crack growth rate due to dissolution at the crack tip [9]. Generally speaking, this differential in dissolution rates can be related to concentration gradients and restricted mass/ion transport. Also, linked cracks show much more significant growth in the length vs the depth as a result of prior crack coalescence [47].

Considering the many variables affecting Stage II crack growth, cracks in the field (even under consistent and constant mechanical and environmental conditions) may continually cycle through active growth, dormancy, and reactivation of growth, especially when mechanical driving forces are low [9, 39]. Due to the compressibility of gases, high-pressure gas transmission pipelines may be more prone to cycling between growth and dormancy phases [39]. Per the work by Chen et al. [9] and Egbewande et al. [43], there are two thresholds for continuous crack growth: a lower threshold for continuous growth of a sharp crack tip, and a higher threshold for continuous growth of a blunt crack tip. Discontinuous crack growth is also discussed by Beavers et al. [48]. The study by Parkins et al. also found some evidence of new cracks nucleating ahead of the tip of existing cracks [10]. Discontinuous crack growth behavior has also been observed in Al alloys [49]. Additionally, Been et al. noted two different growth regimes based on crack size and stress intensity factor [50]. Heavy dependence on environment was observed for small cracks and/or low cyclic loads but for larger cracks and/or high cyclic loads corrosion fatigue and mechanical driving forces were dominant [50].

2.4 Key Factors influencing NNpHCF

This section will follow a parameter breakdown similar to stress corrosion cracking – mechanical loading, corrosive environment, and susceptible materials will be discussed here. Please note that although listed separately, each factor typically interacts with one another to produce a profound effect on crack growth behavior. Variables pertinent to inert fatigue and general corrosion fatigue are discussed, with a focus on the NNpHCF system studied.

2.4.1 Mechanical Driving Forces

When considering the mechanical driving forces that propagate a growing crack, it is important to consider the stress and strain distributions ahead of the crack tip. At increasing maximum stresses, a larger plastic zone will form and the material within the plastic zone will cease to behave linearly with respect to the stress-strain curve. Newman and Raju developed several empirical stress-intensity factor equations pertinent to embedded and surface-breaking elliptical cracks [51]. A schematic describing various crack geometries is shown in Figure 2.11.

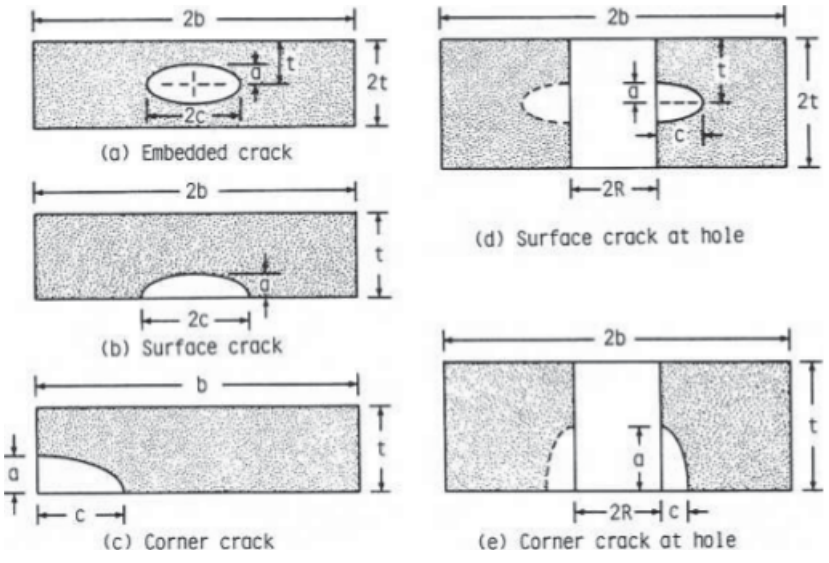

Figure 2.11: A schematic showing: (a) embedded crack, (b) semi-elliptical surface crack, (c) corner crack, (d) surface crack at hole, and (e) corner crack at hole configurations with elliptical crack fronts [51].

The stress intensity factor for a semi-elliptical surface crack is described by the equation developed by Newman and Raju [51]:

$$K_I = S\sqrt{\pi\frac{a}{Q}}F_s\left(\frac{a}{c}, \frac{a}{t}, \frac{c}{b}, \varphi\right) \tag{2.4}$$

for $0 \leq a/c \leq 2$, $c/b < 0.5$, and $0 \leq \phi \leq \pi$. S is the remote uniform tensile stress, a is the crack depth, c is the crack length, t is the plate thickness, Q is the shape factor for an elliptical crack, and F_s is a boundary-correction factor for a surface crack in a plate. Equation 2.4 is only applicable if a/t satisfies the following conditions [51]:

$$\begin{aligned} &\frac{a}{t} < 1.25\left(\frac{a}{c} + 0.6\right) \text{ for } 0 \leq \frac{a}{c} \leq 0.2 \\ &\frac{a}{t} \leq 1 \text{ for } 0.2 \leq \frac{a}{c} \leq \infty \end{aligned} \tag{2.5}$$

The shape factor for an elliptical crack is defined as [51]:

$$\begin{aligned} Q &= 11.464\left(\frac{a}{c}\right)^{1.65} \text{ for } \frac{a}{c} \leq 1 \\ Q &= 11.464\left(\frac{c}{a}\right)^{1.65} \text{ for } \frac{a}{c} > 1 \end{aligned} \tag{2.6}$$

The boundary-correction factor for a surface semi-elliptical crack is described by [51]:

$$F_s = \left[M_1 + M_2\left(\frac{a}{t}\right)^2 + M_3\left(\frac{a}{t}\right)^4\right] g f_\phi f_w \tag{2.7}$$

for $a/c \leq 1$, several curve-fitting functions as outlined by Newman and Raju are described by [51]:

$$\begin{aligned} M_1 &= 1.13 - 0.09\left(\frac{a}{c}\right) \\ M_2 &= -0.54 + \frac{0.89}{0.2 + \left(\frac{a}{c}\right)} \\ M_3 &= 0.5 - \frac{1}{0.65 + \left(\frac{a}{c}\right)} + 14\left(1 - \frac{a}{c}\right)^{24} \\ g &= 1 + \left[0.1 + 0.35\left(\frac{a}{t}\right)^2\right](1 - \sin\phi)^2 \end{aligned} \tag{2.8}$$

The finite-width correction factor is determined by [51]:

$$f_w = \left[\sec\left(\frac{\pi c}{2b}\sqrt{\frac{a}{t}}\right)\right]^{1/2} \tag{2.9}$$

for $c/b < 0.5$ where b is the half-width of the cracked plate.

The angular function derived from the embedded elliptical crack solution is shown by [51]:

$$f_\phi = \left[\left(\frac{a}{c}\right)^2 \cos^2\phi + \sin^2\phi\right]^{1/4} \tag{2.10}$$

The parametric angle ϕ is shown schematically in Figure 2.12.

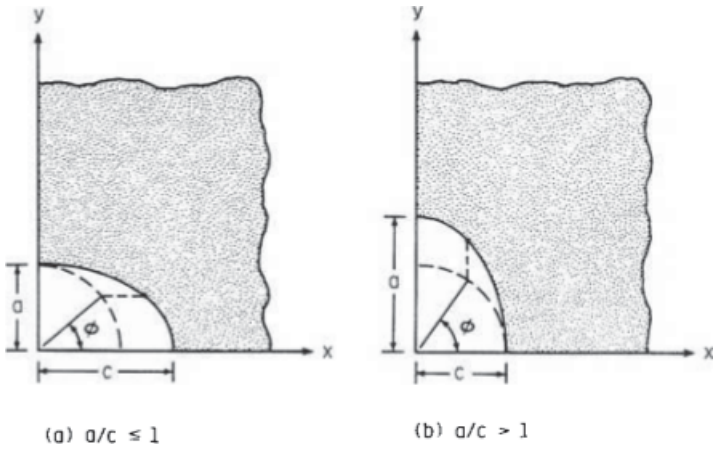

Figure 2.12: A schematic showing the coordinate system used to define the parametric angle [51].

Davidson notes that anisotropic deformation occurs within the plastic zone [18]. It is possible to resolve bulk stresses along slip systems, and this is especially critical since all strains become two- or three-dimensional in bulk materials at the microscale (within the plastic zone) [21]. Some key factors to consider are: opening direction tensile stresses (σ_{YY}), hydrostatic tensile stresses at crack tip (σ_H), and tensile-plastic strain (ε_P) [52]. Note that a branched crack will have a lower stress intensity factor than that at the tip of a straight crack [53]. In order to account for plasticity effects and hardening near the crack tip, Rice and Rosengren studied the crack-tip strain singularity [54] and also developed the J-integral to account for elastic-plastic behaviour [55].

Fleck and Hutchinson developed several theories to describe strain gradient plasticity, noting the differences in strain response based on various length scales [56, 57]. Much higher stress concentrations occur in SGP methods when compared with conventional HRR plasticity methods as a result of a sharp crack tip formed by the accommodation of a high strain gradient by geometrically-necessary dislocations (GNDs), as seen in Figure

2.13 [52]. When accounting for SGP, the crack opening profile becomes much more narrow when compared with the profile derived from conventional plasticity models.

Martinez-Paneda et al. [58] noted that GNDs are significant between 2.5 to 12 microns ahead of the crack tip even if the plastic zone size is much larger, while Gangloff [52] noted that SGP theory is typically relevant for plastic zone sizes between 0.5 to 5 microns. The increased amounts of GNDs will provide more trapping sites for atomic hydrogen and can act as an additional source for H available to contribute to embrittlement effects [58]. Martinez-Paneda et al. note that the impact of SGP is less noticeable as the alloy strength increases due to changes in the plastic zone size [58]. In relation to classical plasticity models [54, 55], SGP models will predict a much steeper stress and strain gradient [58]. Further, Wei and Hutchinson described steady-state crack growth in relation to strain gradient plasticity [59]. Martinez-Paneda and Betegon [60] modelled damage and fracture behaviour within strain-gradient plasticity and found that the SGP effective length increases with load, decreases with yield strength, and decreases with the strain hardening exponent. However, contributions from Poisson's ratio or T-stress were comparatively insignificant on SGP length [60]. Further, SGP effects in general were less significant at lower strains [60].

The local stress distribution ahead of the crack tip will have a direct effect on crack growth behaviour; however, it is also important to understand the impact of stress changes over time. Turnbull notes that the stress ratio R will have a significant effect on the replenishment of solution within the crack tip, leading to lower pH values, higher currents along crack walls, and therefore a more significant potential drop along the crack depth [61]. A higher ΔK at constant R will affect the crack mouth opening displacement and therefore volume-to-area ratio within the crack, causing a slightly higher pH value [61]. Conversely, lower values of ΔK will promote the formation of hydrogen gas bubbles due to a higher amount of hydrogen ions available [61]. It is important to consider not only ΔK, but also $K_{\max}$. Been et al. note that higher ΔK leads to higher da/dN under cyclic loading; furthermore, higher $K_{\max}$ at the same ΔK leads to higher da/dN [50]. Been et al. showed the relative differences in ΔK and $K_{\max}$ for liquids and gas pipelines, as seen in Figure 2.14 [50]. Gas pipelines will likely spend a majority of their lifetimes in Regime I crack growth due to the less severe cycling, while oil pipelines will likely enter Regime II growth much sooner [50].

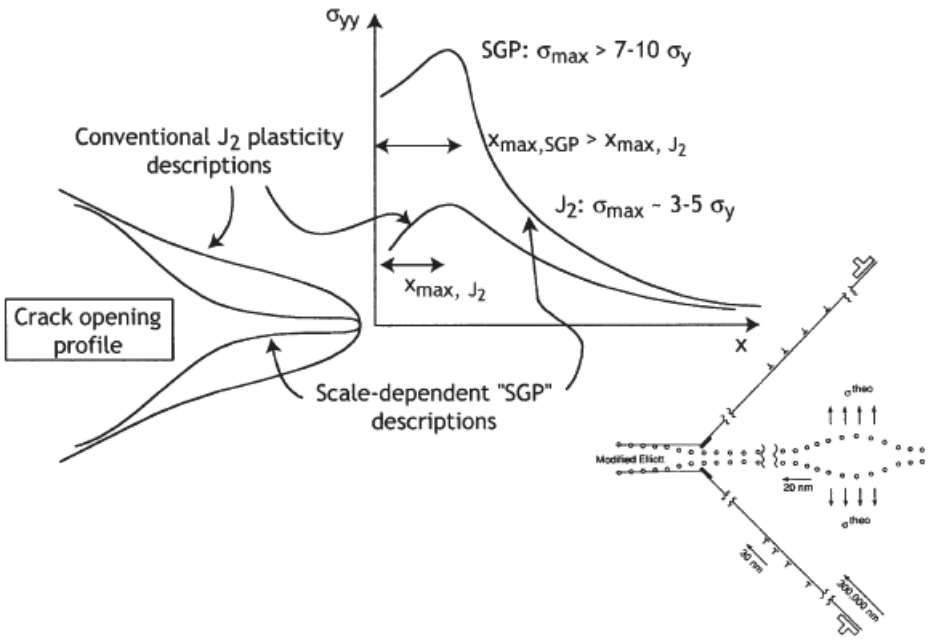

Figure 2.13: Schematic diagrams: (top) distributions of crack-tip tensile stress reflecting either conventional plasticity description of elastic-plastic deformation, or a length-scale-dependent hardening description of near-crack-tip deformation in the presence of a strong strain gradient (Wei and Hutchinson, 1997; Jiang et al., 2001), and (bottom right) the discrete dislocation model of crack-tip mechanics from Gerberich et al. (1991). (SGP refers to strain gradient plasticity) [52].

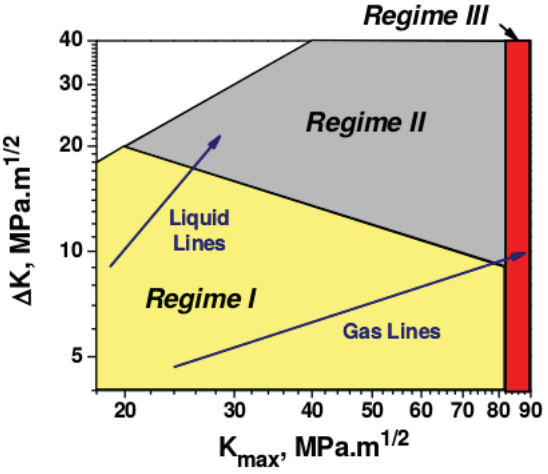

Figure 2.14: As a result of different operating conditions of gas and oil lines, these lines may occupy different quadrants of the ΔK-$K_{\max}$ domain [50].

A large proportion of fatigue crack growth studies have been performed under constant amplitude loading; however, there is still much work left to understanding the complexities associated with variable amplitude loading [9]. Load-history interaction effects

must be considered when studying variable amplitude loading [9]. Many tests on a single specimen can have changes on subsequent crack growth behavior due to load history effects [40]. Load interaction effects will result in a deviation from traditional Paris law fatigue growth since time-dependent contributions to crack growth may be modified [9]. Zhao et al. note that lifetime predictions based on constant-amplitude loading will overestimate crack growth rates for oil pipelines operating in the high-frequency range but significantly underestimate the crack growth of gas pipelines (which typically operate with low loading frequencies) [14]. Generally, constant-amplitude predictions will significantly underestimate crack growth rates due to not accounting for load interaction effects [14].

Crack growth under complex variable amplitude loading is a function of loading history, material properties, microstructure, and environmental conditions [9]. Consequently, the same variable amplitude loading sequence can produce either acceleration or retardation of fatigue crack growth [9]. Repeatedly applied block loading (or spectrum loading) will produce a less-significant load sequence effect, since a quasi-equilibrium state will establish ahead of the crack tip [62]. The effects of different variable amplitude loading spectra (underload, mean load, and overload) are compared schematically in Figure 2.15. Zhao et al. note several mechanisms related to variable amplitude loading such as crack tip blunting, cyclic plasticity-induced residual strength around the crack tip, crack tip plasticity, and plasticity-induced crack closure [9, 14]. Zhang et al. also discuss relevant mechanisms to underloading cycles, such as the tensile residual stresses formed around the crack tip, reduced ductility due to strain hardening ahead of the crack tip, higher tensile mean stresses experienced at the crack tip, and increased ΔK_{eff} due to reduced crack opening stress intensity factor [63].

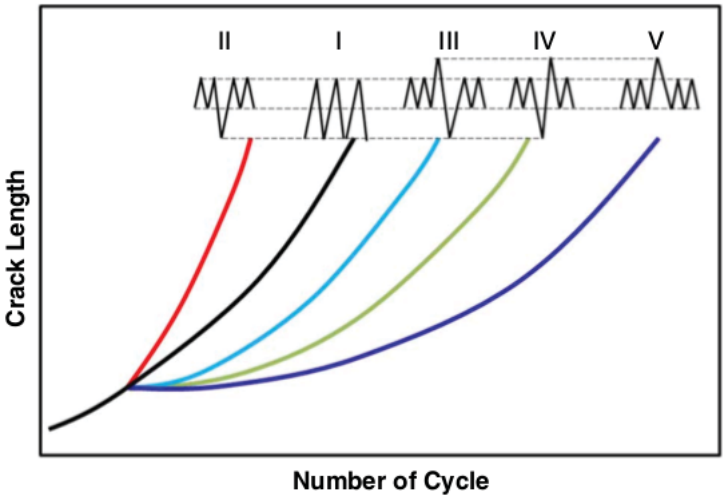

Figure 2.15: Crack growth behavior of variable and constant amplitude loading [9].

Yu et al. showed that time-dependent processes will compete, resulting in a minimum crack growth rate when a monotonic hold of 1 hour followed an underload cycle [64]. This critical value was primarily due to the competition between the gradual exhaustion of mobile dislocations over time (contributing to room-temperature creep and crack tip blunting) and the gradual increase of hydrogen segregation (contributing to hydrogen embrittlement and crack tip sharpening) [64]. Bouaeshi et al. note that as crack depth increases, the stress intensity factor will increase (and more significantly so if the crack tip remains sharp) and hydrogen-enhanced crack growth becomes ever more significant [36]. Ahmed et al. also note differences in crack tip morphologies with respect to the exposure time to a near-neutral pH environment under various loading frequencies [65].

In another study, Yu et al. demonstrated that two different crack growth regimes exist, depending on loading frequency [66]. When the loading frequency is above 1×10^{-3} Hz, crack growth rates increased as frequency decreased; however, loading frequencies below 1×10^{-3} Hz caused crack growth rates to decrease with decreasing frequency to reach a constant crack growth rate at frequencies around 1×10^{-4} Hz [66]. The critical frequency was related to the time required for hydrogen to diffuse to the weakest link in the fracture process zone and allow for crack propagation [67]. Mughrabi et al. note a similar dislocation structure between BCC iron and FCC metals when sufficiently low strain rates are used, allowing for similar mobilities of edge and screw dislocations [68]. However, at higher strain rates (beyond a transition frequency of approximately 1×10^{-3} Hz at room temperature), the mobility of screw dislocations are far less than

edge dislocations [68]. Solomon and McMahon also note that interstitial solutes reduce the relative difference in mobility between edge and screw dislocations, since these same solutes will impede edge dislocations more significantly [69]. Magnin and Coudreuse also explored the effects of strain rate on crack growth behaviour. At sufficiently low strain rates, wavy slip will induce persistent slip bands [70]. At higher strain rates, lattice friction stresses will increase and the formation of PSBs will be impeded due to the occurrence of pencil glide [70]. The study from Sutcliffe et al. shows that the typical loading strain rate for oil and gas pipelines remain lower than $1 \times 10^{-8}\,\mathrm{s}^{-1}$. The change in screw dislocation mobility [68], formation of persistent slip bands and changed lattice friction stresses [70], and contribution from hydrogen [67] as a result of varying strain rates is likely to be at play in the NNpHCF system.

On the atomic scale, Christian showed that dislocation velocity increases with higher stresses, and that dislocation velocity is directly related to strain rate [71]. Higher loading strain rates will cause higher dislocation velocity and larger number of mobile dislocations at the beginning of creep; larger creep deformation will result [72]. An interesting finding by Oehlert and Atrens is that the dislocation velocity is not only dependent on material strength and stress level, but also stress rate-dependent [73]. The amount of creep is reduced as yield strength is also reduced, due to the accompanying drop in dislocation density [73]. Sidey and Coffin note that slow loading-fast unloading triangular waveforms are more damaging than equal strain rates or fast loading-slow unloading waveforms for oxygen-free high conductivity copper at elevated temperatures (673 K) [74]. Interior damage processes are unaffected by the external environment but strongly influenced by loading and unloading strain rates [74]. However, in the case of environmentally-assisted cracking, it is expected that environment will also play a large role in determining overall fatigue lifetimes. Barsom showed that slow loading rates (negative sawtooth) were more detrimental than high loading rates (positive sawtooth) due to the time available for corrosion and crack extension during loading [75]. Further, Gücer and Capa showed that low cycle fatigue lifetimes of low-carbon steel is about twice as long at higher (compared with lower) strain rates [76]. Freund et al. [77] modelled crack growth for high strain rate elastic-plastic crack growth, noting that the flow stress depends on the plastic strain rate. The strain rate dependence of flow stress corroborates the strain rate dependence of dislocation activity.

Although loading frequency is discussed in this section, it is important to consider frequency in the context of interactions with the environment. Mass transport and electrochemical reaction rates may be affected by changed loading frequencies [20]. Parkins and Beavers showed that the crack growth rate in X65 pipeline steel had a direct relationship with crack tip strain rate [11]. Generally, increased applied strain rates will result in an increased crack tip velocity and reduced times to failures [11]. Turnbull notes that at higher loading frequencies, turbulent flow may change mass transport kinetics [78]. While loading frequency has no significant effects on advection of fluid within the crack, the time available for reaction during a cycle will be affected [61]. pH will decrease with increased frequency, and more precipitation will occur as a result of more frequent solution replenishment at higher frequencies [61]. Although general trends are observable, it is prudent to mention that a quasi-equilibrium of various time-dependent factors will be established at a given strain rate, thus resulting in a new crack growth rate.

Amazigo and Hutchinson [79] studied the stress and strain-rate fields for plastic loading and elastic unloading. Hussain et al. [80] studied the strain energy release rate under combined Mode I/Mode II loading. Hall [81] developed an alternative to the Shoji crack tip strain rate equation, incorporating the effects of strain hardening akin to a Gao-Hwang approach. Similarly, Peng et al. [82] expanded upon the Gao-Hwang formulation for crack tip strain rate, normalizing dK/dt by K. The studies by Lu [83] and Young et al. [84] distinguished two components for crack tip strain rate: first from crack tip advance under monotonic hold and the second from corrosion fatigue related to cyclic loading. Although Lu [83] focused on high pH SCC, it is important to note that cyclic loading becomes more significant in contributing to crack growth at higher loading frequencies. Moran and Shih [85] provided a general treatment of crack tip contour integrals. Gupta et al. [86] provided a fairly comprehensive review of T-stress, the shear stress acting parallel to the crack tip. One key finding was that negative T stresses increase fracture toughness [86]. Further, consideration of the T stress will change the stress-strain distributions around the crack tip [86, 87] and consequently affect hydrogen segregation behaviour and crack tip shielding effects.

2.4.2 Corrosive Environment

This section will briefly discuss the typical environment that can bring about NNpHCF. Some key points of discussion include the effects of pH, solution chemistry, electrochemistry, temperature, and coating types on crack growth behaviour. Parkins provided a detailed review of SCC in high pressure gas pipelines [88]. The formation of an environment that causes SCC cracking can be related to a combination of the following: coating deterioration leading to the formation of discontinuities and/or the diffusion of water, carbon dioxide, and other species through the coating; the disbonding of the coating from the pipe surface; the coating type; soil moisture and electrolyte content, including variations in season, terrain, chemistry, and resistance to electrical currents associated with cathodic protection systems; stresses due to soil movements; pipe surface temperature; and the initial condition of the pipe during coating application [88].

It is important to first discuss the reactions at play in the NNpHCF system prior to discussing the environment's effect on crack growth behaviour. Chen et al. summarize the effects of applying a cathodic potential on the local electrochemical environment under areas of coating disbondment [89]. Generally, a more negative applied cathodic potential increases the pH within a disbondment [89]. The rise in pH within the crevice would be the result of water reduction through the following reaction [89]:

$$2\,H_2O + 2\,e^- \longrightarrow 2\,OH^- + H_2 \tag{2.11}$$

Another reaction responsible for the increase in pH is the cathodic reduction reaction of oxygen [89]:

$$O_2 + 4\,H^+ + 4\,e^- \longrightarrow 2\,H_2O \tag{2.12}$$

In the absence of CP, steel is free to corrode per the following two hydrolysis reactions [89]:

$$Fe \longrightarrow Fe^{2+} + 2\,e^- \tag{2.13}$$

and

$$Fe^{2+} + 2\,H_2O \longrightarrow Fe(OH)_2 + 2\,H^+ \tag{2.14}$$

Note that the corrosion reactions will generate hydrogen ions and thus decrease pH over time as these ions are dissolved into the solution [39]. The steel will be anodically polarized due to the formation of an O_2 concentration cell [89]. Ferrous ions (and therefore positive charges) will build up within the crevice, causing corrosive anions (such as Cl^- and $SO_4{}^{2-}$) to migrate into the crevice and decrease pH [89]. Since oxygen is a neutral species, it will diffuse very slowly since its concentration is not affected by a change in potential [89].

The presence of CO_2 will allow for buffering of the pH due to the formation of carbonic acid [89]:

$$CO_2 + H_2O \longrightarrow H_2CO_3 \tag{2.15}$$

Carbonic acid will further dissociate per the following two reactions [89]:

$$H_2CO_3 \longrightarrow H^+ + HCO_3{}^- \tag{2.16}$$

and

$$HCO_3{}^- \longrightarrow H^+ + CO_3{}^{2-} \tag{2.17}$$

Although previous work suggests that hydrogen is primarily introduced via the reduction of water, Chen et al. suggest that the dissociation of carbonic acid acts as a primary source of hydrogen [89]. If the pH drops to between 4 and 6, the following cathodic reaction is dominant [89]:

$$H_2CO_3 + e^- \longrightarrow H^+ + HCO_3{}^- \tag{2.18}$$

Note that at low pH (between pH 4 and 6), the reduction of hydrogen ions is dominant. However, when the solution pH is greater than 6, the reduction of water is dominant. Note that iron carbonate can form as well, per the following reaction [89]:

$$Fe^{2+} + {CO_3}^{2-} \longrightarrow FeCO_3 \tag{2.19}$$

$FeCO_3$ will form as a film and reduce the surface area available for reaction, thus decreasing the corrosion rate and inhibiting access of cathodic current to the steel surface [89]. This is one mechanism that causes pH to stay near a value of 7 [89]. Chen et al. also discuss the formation of calcite (calcium carbonate) and siderite (iron carbonate) [90]. Formation of these precipitates will cause depletion of carbonate ions [44]. Turnbull and Ferriss note that the oxygen reduction reaction (which produces hydroxyl ions) was shown to be insignificant in comparison to other reactions [61]. From the above, we can infer that the formation of carbonates will be more favourable than the formation of hydroxides. Regardless of the type of surface film formed, the net effect is a change in both the rate of hydrogen generation due to corrosion of iron, as well as the rate of hydrogen ingress.

CO_2 is continually supplied by the decay of organic matter in the soil [91], and CO_2 concentrations are expected to fluctuate throughout the year as activity of decaying organic matter changes [4]. Adequate levels of CO_2 are critical to maintaining near-neutral pH during application of CP [92]. Patel showed that the presence of sulfate, chloride, and nitrate ions (listed in order of aggressiveness) caused acceleration of dissolution kinetics in mild steel exposed to aqueous solutions containing the species aforementioned [93]. Enhanced localized corrosion due to stress may occur in the active state [78]. Beavers and Harle also discuss the effect of nitrates, phosphates, and caustics on crack behaviour [91].

NNpHCF typically occurs at the free corrosion potential (between -760 $mV_{Cu/CuSO_4}$ and -790 mV

Note that NNpHCF is less sensitive to changes in cathodic potential than in high pH SCC cracking [91]. Generally, CP will restore fatigue lifetimes to that in air, but an applied potential may not have much of an effect where cracks can propagate under LEFM conditions [20]. The effect of polarization on crack growth rates will manifest in a change

in crack tip electrochemistry – specifically due to a shift in dissolution, repassivation, and hydrogen evolution kinetics [20]. An important note by Turnbull is that crack depth will not affect crack tip electrochemistry in a significant way for a constant ΔK [94]. However, at anodic potentials, the potential drop increases significantly as crack depth increases [94]. Another interesting note is that dissolution mechanisms will enhance shallow crack growth, while hydrogen-driven shallow crack growth will be hindered due to increased mixing with the bulk solution [94].

2.4.3 Susceptible Materials

Note that for the 95% of NNpHSCC failures at $> 60\%$ SMYS, no in-service or hydrostatic test failures were seen in pipelines installed after 1981, in a study by Batte et al. that covered pipeline failure data from the 1965 to 2010 [12]. Crack colonies are expected to remain dormant unless the mechanical driving force is sufficient to overcome the threshold of Stage II crack growth [9]. For cracks near the threshold of Stage II crack growth, residual stresses [95, 96] combined with a sufficient level of diffusible hydrogen [39] can reactivate a dormant crack [9]. Surfaces with high residual tensile stresses will be prone to pitting formation [95] but NNpHCF cracking is typically found at areas with an intermediate level of tensile residual stresses due to the slower transition of residual stresses through the pipe wall thickness [9].

The microstructure of a given material can have a significant impact on the corrosion fatigue crack growth behaviour in near-neutral pH environments, especially during crack initiation and early growth. As noted by Akid, metallurgical barriers to Stage I crack growth such as grain boundaries and intermetallic particles are closely tied to crack behaviour [20]. Inclusions can directly dissolve and form pits, generate microgalvanic effects, or cause a local solution chemistry change and result in pitting [78]. Furthermore, clustering of inclusions or particles can lead to pit coalescence [78]. Inclusion clustering is noted as an issue more typical to "dirtier" vintage 1960s steels due to the relatively high density of MnS inclusions [97]. Elboujdaini and Revie observed higher susceptibility to hydrogen-enhanced SCC and hydrogen-induced cracking in steels with sulfide inclusions and banded microstructures [98]. Further details of residual stress fields acting around nonmetallic inclusions is discussed by Miller [21].

Consideration of the microstructure is key in deciphering seemingly paradoxical crack growth behaviour. From a corrosion perspective, pitting is preferred in ferrite as opposed to pearlite [20]. However, in the study by Boukerrou and Cottis, crack initiation was easier in soft ferrite but pit growth was more rapid in pearlite for steels exposed to salt solutions [37]. Boukerrou and Cottis attributed easier crack initiation in ferrite due to pearlite having a higher hardness (related to higher carbon content) and requiring a larger defect to trigger crack initiation [37]. Contrasting the work from Akid [20] and Boukerrou and Cottis [37], it is not always simple to infer crack growth rates from corrosion growth rates. Further, although Sutherby and Chen [99] note that banded microstructures can cause deflection in crack growth due to changes in properties and residual stress profiles, Chen et al. [39] note that the effect of banded microstructures on early- and intermediate-stage crack growth are likely limited. In a study by Brongers et al., X65 CT specimens exhibited more ductile tearing than X52 samples [100]. Despite the higher yield strength, the X65 specimens showed a larger CTOD, indicating higher fracture toughness and therefore resulting in the larger ductile tearing extent [100].

In the context of environmentally-assisted cracking, material heterogeneity can either enhance or retard crack growth. For example, a microalloyed steel with a ferritic matrix was observed to have a lower susceptibility to SCC when compared with a microalloyed steel with a bainitic matrix [101]. Liang et al. note that strain-aged steel has increased susceptibility to hydrogen embrittlement under applied cathodic potentials [102]. A study by a committee of The Iron and Steel Institute of Japan show that thermo-mechanical controlled processing or quenched and tempered steels with fine-grained bainitic structures are more resistant to intergranular SCC when compared with controlled rolled steels with ferrite-pearlite structures (typical of X65, for example) [88]. Bainitic and acicular ferrite microstructures were generally more effective at inhibiting hydrogen diffusion when compared with ferrite-pearlite mixtures [103]. Torres-Islas et al. found that susceptibility to hydrogen embrittlement was more severe for quenched and tempered X70 pipeline steel in dilute bicarbonate solutions, while anodic dissolution and film rupture was more prevalent in as-received and water-sprayed X70 steels [104].

Further microstructural modification as a result of manufacturing and fabrication processes should also be considered in understanding crack growth behaviour. Long-seam low-frequency electric resistance welds (LFERW) have shown more susceptibility to

NNpHSCC than for double submerged arc welds (DSAW) [4]. Note that the coarse-grained heat affected zone (CGHAZ) of DSAW welds also showed accelerated crack growth rates when cyclically loaded in NS4 groundwater [6]. Per the review study by Ritchie and Suresh, the effect of grain size on crack propagation has generally been found to be negligible at intermediate crack growth rates [105]. However, during near-threshold crack growth, coarse-grained materials showed decreased growth rates and higher thresholds for propagation [105]. The residual stresses from pipe manufacturing, as well as subsequent handling and fabrication, will greatly affect the behaviour of a propagating crack. A study by Beavers et al. showed that the residual stresses can be 216 ± 104MPa at a 99.98% confidence level [106]. Combining residual stresses with maximum operating pressures (e.g. 72% SMYS) can easily result in stresses equal to or greater than SMYS, providing a significant mechanical driving force for crack propagation [9]. Residual stresses will affect the mechanical properties of the near-surface layer [107]. Also consider stress concentrations at the toe of longitudinal seam welds – a study by Eadie et al. showed that the stresses at the toe of the weld can be tensile up to the yield strength [108]. Shot peening may be a sufficient means to mitigate unfavorable stress distributions around the weld toe and thus minimize risk for cracking [108]. Andresen and Morra considered loading rates with respect to time, but also dK/da, the effects of changing stress intensities as crack depth increases [109]. Studying the stress intensity factor as a function of crack depth helps with better understanding the relative contribution of residual stresses present in the material [109].

In the work by van Boven et al., details regarding the effects of prior cyclic loading on early-stage crack growth are discussed [110]. Furthermore, residual stress profiles along the thickness of tensile specimens are shown, with a tensile residual stress between 200 MPa and 300 MPa at the surface [110]. Although a banded microstructure was observed in the specimens, microstructure heterogeneity did not play a dominant role in crack growth [110]. Residual stress profile changes following cyclic conditioning are also discussed [110]. Precyclic loading can have an effect on crack initiation by altering residual stress profiles and generating persistent slip bands, leading to preferential dissolution and thus crack formation [111]. Further, machined and also ground surfaces will typically have a near-surface microstructure with a grain size on the scale of nm with a depth that depends on machining history [107]. Surface roughness was explored by He et al., where higher surface roughness caused a more negative OCP [112]. Thus, a higher

diffusible hydrogen concentration is achieved with rougher surfaces [112]. Fatigue lifetime decreases with increased surface roughness due to local stress concentrations [20]. Also consider mill scale from welding or fabrication, which may act as a cathode and cause the formation of a galvanic cell [78].

2.5 Mechanisms of NNpHCF

This section highlights key mechanisms relevant to NNpHCF: anodic dissolution, hydrogen-enhanced crack growth, and the environmentally short crack effect.

2.5.1 Anodic Dissolution

As highlighted by Egbewande et al. [43] and King et al. [44], the overall crack growth rate during NNpHCF is much higher than the rate of dissolution. Thus, anodic dissolution will not be discussed in detail. However, there are 4 main mechanisms related to anodic reactions: slip dissoluton, anodic-reaction-induced cleavage, anodic-reaction-enhanced localized plasticity, and a variety of surface mobility models [78]. While Najjar et al. noted that there could exist a competition between anodic dissolution and hydrogen embrittlement, localized anodic dissolution can act synergistically with absorbed hydrogen to aid in localized plasticity effects [113]. Jones proposed a mechanism where corrosion-induced strain relief occurred at the crack tip for passivating metals [114]. Although the discussion was focused on stainless steels, an analog can be applied to carbon steels where localized strain relief due to anodic dissolution occurs. Jones states that the presence of a corrosive medium is able to relieve strain hardening and effectively eliminate the fatigue limit typically observed in fatigue testing of ferrous alloys [114]. Magnin et al. also discuss a similar mechanism where plasticity is locally enhanced due to anodic dissolution [115].

2.5.2 Hydrogen Enhanced Crack Growth

According to API 579-1 (2007) Annex F, hydrogen-assisted cracking (HAC) "occurs when hydrogen is absorbed by a material during a corrosion process, or by exposure to high-temperature and/or high-pressure hydrogen gas, and diffuses to a pre-existing

flaw as atomic hydrogen, and stresses are applied, including residual stresses, to the flaw" [19]. Generally, hydrogen embrittlement can be categorized as either internal-hydrogen assisted cracking (IHAC) or hydrogen-environment-assisted cracking (HEAC) [52]. Further discussion of hydrogen-enhanced fatigue crack growth can also be found in the review by Nanninga and White [116]. Regardless of the diffusion path, there are three key rate-limiting steps in hydrogen-enhanced fatigue crack growth: the rate of creation of a new crack surface, the rate of hydrogen dissociation and adsorption, and the rate of diffusion of H to the fracture process zone [116].

In IHAC, atomic hydrogen can be introduced throughout a specimen during manufacturing operations (e.g. casting, welding, surface-chemical cleaning, electrochemical machining, electroplating, and heat treatment) as well as through environmental exposure (e.g. cathodic electrochemical reactions at low temperatures and gaseous hydrogen exposure at higher temperatures) [52]. Crack growth below the threshold in inert environments can occur when the hydrogen-charged metal is subjected to loading [52]. Due to stress concentrations ahead of the crack-tip and a resulting stress and chemical potential gradient, dissolved hydrogen will segregate to the crack-tip process zone to promote crack growth [52, 117]. Note that stress is not necessary for hydrogen uptake and that the environmental hydrogen production at the crack tip during stressing is not typically significant in IHAC [52]. For HEAC however, atomic hydrogen is mainly produced on clean crack surfaces near the crack tip [52]. Atomic hydrogen (H) will be produced by dissociative chemical adsorption for H_2, chemical reactions for gases such as water vapor or H_2S, or via electrochemical cathodic reactions in acidic or alkaline electrolytes [52]. H will then diffuse into the fracture process zone (FPZ) and assist crack propagation [52]. Consequently, environmental mass transport kinetics will control rates of HEAC [52]. The diffusion paths for both IHAC and HEAC are summarized in Figure 2.16. Diaz et al. also provided a review on diffusion models related to hydrogen embrittlement [118].

Note that both IHAC and HEAC can be operative if a precharged steel is stressed in an H-producing environment [52]. The key difference between IHAC and HEAC is related to the kinetics of mobile H diffusion and resulting crack growth [52]. Microscopic FPZ damage will also change between IHAC and HEAC due to the different kinetics and dislocation density profile around the crack tip [52]. In NNpHCF, crack tip hydrogen is much less significant when compared with the amount of hydrogen generated at the bulk surface [39, 119]. While bulk amounts of hydrogen are plentiful, Turnbull notes that at

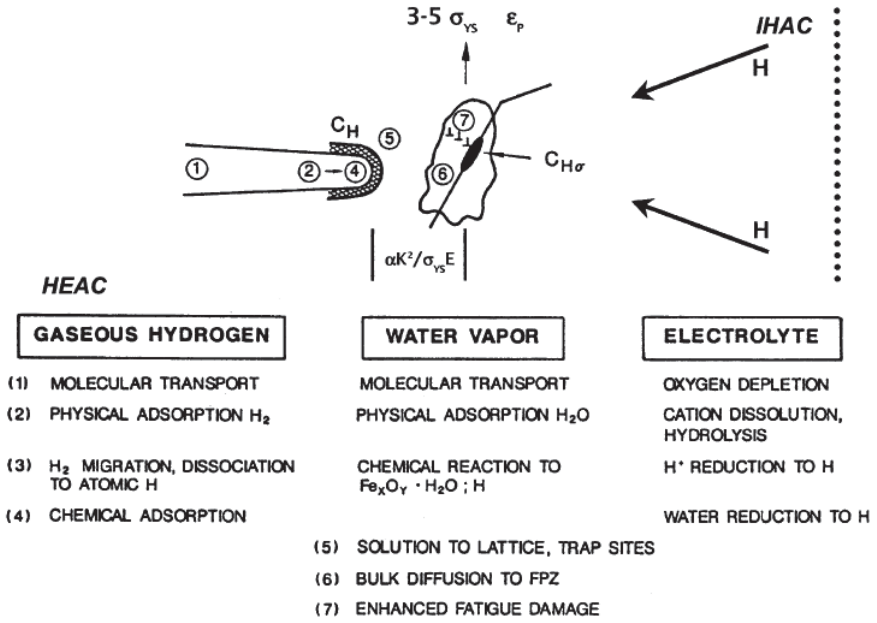

Figure 2.16: The sequence of elemental processes that supply damaging H to the crack-tip fracture process zone during either HEAC for gaseous hydrogen, water vapor or an electrolyte, or IHAC for an H precharged microstructure. The dotted line indicates the outer boundary of the plastic zone. Crack-tip tensile stresses are maximized at some distance ahead of the tip, proportional to $K^2/\sigma_{YS}E$ [52].

potentials more negative than -1000 mV(SCE), the influence of crack tip charging begins to play a more dominant role [61]. More cathodic potentials will promote H uptake as long as there is a sufficient crack tip potential drop compared with the broadly exposed surface [52]. Crack pH will become more alkaline but H production at the exposed surface will become the dominant supply of H to the crack tip FPZ [52].

Krom et al. [117] studied hydrogen transport near a blunting crack tip, building on the work by Sofronis and McMeeking [120]. It was noted that there was no clear evidence if H typically occupies the octahedral or tetrahedral lattice sites but regardless, there is a volume increase since the volume of H is greater than the interstitial site volume [117]. The number of lattice sites can be represented by

$$N_L = N_A \beta \rho / A_r \tag{2.20}$$

where β is the number of interstitial lattice sites per metal atom, N_A Avogadro's number ($6.022 \times 10^{23}\,\mathrm{mol}^{-1}$), ρ the density of the metal ($7.87 \times 10^3\,\mathrm{kg\,m}^{-3}$ for iron at 293K), and

A_r the atomic mass ($55.8 \times 10^{-3}\,\mathrm{kg\,mol^{-1}}$) [117]. Assuming tetrahedral site occupancy is preferred at room temperature in ferrite, $N_L = 5.1 \times 10^{29}\,\mathrm{m^{-3}}$ [117]. Krom et al. note that an increased loading time will provide more time for hydrogen diffusion and therefore re-filling of any depleted lattice sites [117]. Further, a higher strain rate will effectively reduce the hydrogen concentration in lattice sites as trap sites are generated and filled [117]. Hydrogen concentration in trap sites were considered to be relatively independent of strain rate, so the concentration of hydrogen in the lattice is likely to be the key determinant in the extent of embrittlement effects [117]. However, noting the work by Mughrabi et al. [68], changed screw dislocation activity may also play a role in the hydrogen transport at higher strain rates. Krom et al. also note that the effects of strain rate will decrease as the hydrogen concentration in lattice sites increase since the relative amount of hydrogen moving to trap sites will decrease [117]. In another study, Song and Curtin [121] performed molecular dynamics simulations to study hydrogen embrittlement in metals. Formulations for the velocity of H atoms moving toward the crack tip and a crack growth rate were developed [121].

Looking at loading conditions, a significant number of minor cycles will not directly induce crack growth, but will aid in hydrogen segregation to the crack tip [122]. The work by Xing et al. shows that even a few minor cycles can cause significant concentration of hydrogen near the crack tip [123]. Due to elevated stresses ahead of the crack tip and accumulating plastic damage due to minor cycles, hydrogen atoms will accumulate within the plastic zone during cyclic loading [124]. The equilibrium hydrogen concentration will be much smaller near the boundary of the plastic zone and thus hydrogen diffusion into the crack tip region during loading will be much greater than diffusion away from the crack during unloading [124]. This non-equal diffusion will serve as an added mechanism to elevate H levels within the fracture process zone.

The extent and distribution of H trapping can either increase or decrease the hydrogen embrittlement susceptibility of an alloy [52, 125]. Effectively, the net diffusivity of H would be lowered by the presence of irreversible traps, especially if a finite quantity of H is available [52, 118]. An additional effect of the presence of microstructural traps is an apparent increase in solubility [118]. The resistance to subcritical cracking can be increased if a homogeneous distribution of irreversible trap sites is achieved, due to the reduction of H segregation to the crack-tip FPZ [52]. One example is illustrated in the work by Cotterill and King [126], where fatigue crack growth rates were comparable at

lower stress intensity ranges ($\Delta K \approx 22\,\mathrm{MPa\,m^{0.5}}$) but at higher ($\Delta K \approx 40\,\mathrm{MPa\,m^{0.5}}$) there was a much larger increase in crack growth rates [116]. It is important to differentiate between the total H concentration and the diffusible H concentration. The total H concentration represents the sum of H dissolved in the alloy lattice, H in dynamic equilibrium with one or more reversible trap sites, and H trapped strongly in irreversible trapping sites [52, 125, 127]. The amount of diffusible hydrogen will depend on the energy associated with H-lattice solution and H-trap binding energy [52, 128].

Generally, a higher concentration of H dissolved in the lattice will decrease the threshold stress intensity and increase the subcritical crack growth rates for IHAC [52, 129–133]. It is important to note that reversible trap sites can act as a reservoir for diffusible H and supply the crack-tip FPZ with H, decreasing the resistance to IHAC [52, 132, 133]. Parkins and Beavers note that internal cracking within pearlite colonies may be highly related to the hydrogen trapping within said colonies [11]. Liu et al. showed that Al-rich inclusions in X70 pipeline steel act as hydrogen trapping sites and can act as crack initiation sites due to hydrogen embrittlement [134]. Bhadeshia notes the importance of time and temperature considerations when analyzing the reversibility of a given hydrogen trap [103]. At ambient conditions, a trap may be irreversible but completely reversible at higher temperatures [103]. Materials with higher tensile strength typically will have stronger H trapping due to the presence of nanoscale features that act to strengthen alloys but provide effective sites for H segregation [52]. TiC particles were shown as a strong trapping site in HSLA steels as per Stevens and Bernstein [52, 135].

Once H reaches the FPZ, three main mechanisms can occur to aid crack growth: hydrogen-enhanced decohesion (HEDE), hydrogen- enhanced localized plasticity (HELP), and adsorption- induced dislocation emission (AIDE). Regardless of the damage mechanism, it is important to separate hydrogen-assisted cracking from crack-tip fatigue when $K_{\max}$ remains below K_{HAC} [52]. Generally, sufficient levels of H will act to reduce the threshold stress intensity required for cracking. Chen and Wang discuss low-temperature creep and the effects of cyclic and static load, pre-loading strain, etc. [136]. Accelerated plastic deformation during a hold following cyclic loading was observed [136]. Higher corrosion rates have been attributed to cause more crack tip blunting, thus hindering crack propagation by reducing the stress concentrations ahead of the crack tip [43]. Although higher rates of H production and potentially higher crack growth rates would

be expected with higher corrosion rates, localized plasticity effects may work to compete with crack growth [43]. Further discussion of room-temperature creep was also put forward by Oehlert and Atrens [73].

A fully coupled cohesive zone model for environmentally assisted fatigue was developed by del Busto et al. [137], accounting for the effects of trapping, chemical potential gradients, strain hardening, and constraint conditions related to T-stress. Dadfarnia et al. [138] analyzed the hydrogen diffusion rates as a function of dislocation density in BCC and FCC metals, recapitulating that BCC metals have a higher lattice diffusivity but lower solubility for H when compared with FCC metals. It is important to note that Dadfarnia et al. studied H gradients based on equilibrium between H in the lattice and H trapped in dislocations [138]. In the case of higher strain rates, a dynamic equilibrium may be established where dislocations will carry less hydrogen [138]. In BCC steel, H transport via mobile dislocations moving 45 degrees to the crack propagation direction was significant, especially at higher dislocation densities and velocities [138]. Dadfarnia et al. note that prior cyclic loading would generate dislocation cells that can act as a source for hydrogen in subsequent damage processes [138]. When considering the overall hydrogen concentration, it is important to consider both the trap binding energy as well as the trap density [138]. With a higher trap binding energy, higher trap density, and lower lattice diffusivity, H transport via dislocations become an increasingly significant source for embrittlement effects [138]. Further details regarding trap binding energies are listed in the review by Jemblie et al. [139], but 60-70 kJ/mol is typically treated as the transition point for traps acting as reversible vs irreversible. Although irreversible traps may not release hydrogen within a relevant timescale at a given temperature, Turnbull [140] notes that H will eventually diffuse out of these traps. Higher loading rates will result in higher plastic strain rates, and therefore an increased number of mobile dislocations may transport H locked at dislocation cores [138]. From the study by Dadfarnia et al. [138], the active dislocation transport distance is many times greater than the CTOD, indicating that H can be segregated to the crack tip and fracture process zone from a relatively large sampling distance. However, it is important to note that Toribio [141] has shown that the maximum hydrostatic stress (and therefore where hydrogen segregation and embrittlement is most significant) is typically on the order of 1 micron.

2.5.3 Environmentally Short Crack Effect

As crack size becomes sufficiently small, the interaction of environment and acting stresses will cause a deviation of crack growth rates from predicted rates corresponding to a longer and deeper crack. The mass transport of species in a crack is critical in understanding the effect of reactive species interacting with the crack tip and resulting crack growth. Three main factors that must be considered for reactive species in a crack are mass transport, local volume of solution to metal area ratio (which is a function of crack opening width), and reaction rate [107]. Engelhardt and Macdonald [142] note that two main cases can be described for corrosion fatigue: one mode under diffusion control (when the crack tip species are saturated), and in mixed-case kinetics where a quasi-equilibrium is established adn dependent on current density at the crack tip, crack tip potential, and concentration of species near the crack tip [142]. Mechanisms of mass transport considered are advection due to fluid motion induced by cyclic displacement of crack walls, and diffusion and ion migration due to the electrode reactions occurring at the crack walls and crack tip [61]. In the case of corrosion fatigue cracks, a further complexity that must be considered is the effect of crack solution pumping as a result of cyclic crack opening and closing [107]. The pumping effect will be more significant for deep cracks, as noted by Turnbull [107]. Mass transport will be primarily influenced by diffusion for short cracks, and the crack depth l_{crit} below which diffusion prevails is roughly estimated as

$$l_{\text{crit}} \leq \frac{(D_N/f)^{1/2}}{1 - R^{\alpha}} \tag{2.21}$$

where D_N is a typical diffusion coefficient, f is the cyclic loading frequency, R is the stress ratio ($K_{\min}/K_{\max}$) and α is a geometry-dependent factor (approximately 0.5 for a trapezoidal-shaped crack and 1.0 for a parallel-sided crack) [107]. Other important considerations would be the thickness of the diffusion boundary layer, which is on the order of several hundred microns for actively corroding steels in marine-like environments [107].

Finally, buildup of corrosion product and precipitates within the crack may significantly reduce mass transport of reactive species as a result of limiting diffusion paths. In addition to limited mass transport, calcareous deposition can cause crack closure effects

even in short crack specimens [107, 143]. Due to limited mass transport within a crack, the metal ion concentration will gradually increase until either equilibrium is reached via mass transport, or the solubility limit of metal hydroxides, oxides, carbonates, or salts will be reached [143]. An important note from Turnbull is that the through-thickness crack nature of most fracture mechanics specimens generates an artefact of testing, since mass is not truly conserved when fluid is allowed to flow in the through-thickness direction [143]. In low-conductivity solutions, anions can be drawn into the crack as a result of differential oxidizing conditions between the crack and the bulk solution [107]. Consequently, the potential drop in the crack can be smaller than in the solution outside the crack [107, 143]. The lower potential drop in the crack can be explained by the buildup of ions within the crack, thus raising the local solution conductivity [143]. Note that the internal crack surface is consequently polarized anodically with respect to the bulk metal surface [143]. Figure 2.17 highlights the potential drop phenomenon within a constrained crack. Note that there are two potential drops typically associated with a crack exposed to a corrosive environment: one along the length of the crack towards the crack tip, and one along the bulk surface between the crack mouth and the bulk solution.

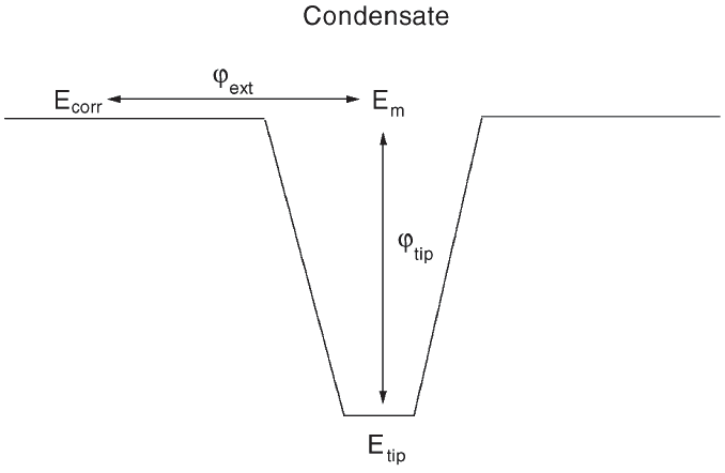

Figure 2.17: Components of potential drop in a system with low bulk conductivity or with condensate. E_{corr}, E_m, and E_{tip} are the corrosion potential, crack mouth potential, and tip potential, respectively, while ϕ_{ext} and ϕ_{tip} are the potential drops in the bulk and crack solutions, respectively [143].

2.6 Summary

To summarize, three types of fatigue: inert fatigue, corrosion fatigue, and NNpHCF were discussed. NNpHCF was noted as highly related to hydrogen-enhanced fatigue crack growth. Three main factors related to NNpHCF were also discussed: the mechanical driving forces, corrosive environment, and susceptible materials. The various factors all play a role in either sharpening or blunting the crack tip; many parameters interact with one another and may even act synergistically to promote or retard crack growth. Finally, three key mechanisms for NNpHCF were discussed: anodic dissolution, hydrogen-enhanced crack growth, and the environmental short crack effect. Similar to the factors mentioned above, the three mechanisms can either act competitively or synergistically to sharpen or blunt a propagating crack tip. Further to the above literature, this thesis will focus on understanding the role of strain rate, specifically the strain rate during unloading, for X65 pipeline steels exposed to a near-neutral pH dilute bicarbonate environment with an applied cathodic potential. The role of hydrogen during unloading will also be discussed.

Chapter 3

Experimental Methods

3.1 Overview

In this chapter, the methods used to prepare the samples for testing, as well as the steps taken to simulate the NNpH environment are outlined. The loading conditions used to simulate various unloading rates are summarized, and the characterization methods are explained. Note that much of the experimental procedure follows work from Engel and further details can be found in that thesis [144].

3.2 Sample Preparation

Samples were machined from sections of API 5L X-65 (CSA Z245.1 Grade 448) pipeline steel that was previously characterized as susceptible to NNpH cracking [145]. The composition of the steel is listed in Table 3.1 below. This proeutectoid steel tested had a microstructure primarily composed of polygonal ferrite. Semicircular notches with a length of 5.0 mm and a depth of 2.5 mm were machined via electrical-discharge machining (EDM) into each reduced section, as shown schematically in Figure 3.1a. The length of the specimen was taken parallel to the length of the pipe, with the notches being machined on the side corresponding to the outer surface of the pipe; a reference schematic of a pipe section is shown in Figure 3.1b.

Table 3.1: Composition of X65 steel tested.

Element	**Composition (wt%)**
C	0.13
Mn	1.55
Cu	0.05
Nb	0.05
Cr	0.08
Mo	0.01
V	0.002
Ni	0.05
Al	0.042
Ti	0.002
N	0.009
Fe	Bal.

The reduced sections were ground perpendicular to the crack to a 600-grit finish, cleaned (degreased in acetone and then ethanol, followed by air drying), and fatigue precracked according to ASTM E647-08 by approximately 1.5 mm on each side of the notch (0.5 mm for each load step). Note that grinding was performed in multiple steps, starting from 240-grit and followed by 320-, 400-, and 600-grit SiC paper. For brevity, all processing steps involving sectioning, grinding, polishing, and replication involved subsequent cleaning, as aforementioned, to minimize any residue interfering with the surface of the sample or crack during testing or post-test characterization. Constant amplitude loading using a triangular waveform with a stress ratio $R = 0.1$ was applied during precracking, with a maximum stress of 65%, 58.5% and 52.7% SMYS, respectively. These stresses were selected to minimize residual plastic zone effects from precracking on subsequent testing. Three stages of pre-cracking with reducing stresses were used to balance pre-cracking time with gradually reducing plastic zone sizes. A servohydraulic loading frame (MTS 612.13) controlled with Instron Wavemaker software was used for precracking. A schematic of the sample cross-section following precracking is shown in Figure 3.1c. The surface length was measured with an optical microscope attached to a Vickers microhardness tester (Buehler IndentaMet 1104). Note that the surface length was periodically measured during precracking to ensure closer dimensional control. When

necessary, individual cracks were isolated from precracking with the use of tool steel dowel pins and cyclindrical adapters.

After pre-cracking, the samples were milled down by 2.5 ± 0.1 mm in order to remove the EDM notches, leaving a semi-elliptical surface crack for testing (schematic shown in Figure 3.1d). The length/depth ($2c_0/a_0$) aspect ratios were between 4.3 and 9.0, with surface lengths ($2c_0$) between 3.3 and 5.5 mm. Pre-test dimensions are shown in Tables 3.2 to 3.4. The reduced sections of the milled specimens were ground again to a 600-grit finish. Vickers microhardness measurements were then taken; hardness indents were also used as a reference point for later characterization. Following hardness measurements, pre-test cellulose acetate replicas (with a thickness of 125 µm) were taken for characterization via SEM. The replicas were mounted on Al sample stages with Pelco carbon conductive tabs, and the replicas were trimmed to the edges of the stage. Pre-test replicas were coated with graphite prior to SEM characterization to prevent charging of the replica surface during imaging. Lower accelerating voltages (5 kV) were used in order to minimize damage from the electron beam, as well as charging of the cellulose acetate replicas in case of insufficient grounding.

Table 3.2: Initial dimensions [µm].

	Initial Depth (a_o)			**Initial Length ($2c_o$)**		
Waveform	**Hydrogen**	**Exposed**	**Air**	**Hydrogen**	**Exposed**	**Air**
10 s ULH	865	885	1000	5288	5470	5507
30 s ULH	1191	1146	1126	5092	5407	5358
60 s ULH	698	370	718	4464	3334	4743
250 s ULH	700	918	890	4473	4996	5296
500 s ULH	655	660	864	4777	4817	5334
10 s +CA	612	619	841	4676	4770	5315
500 s CA	1038	1099	1105	5063	5378	5349

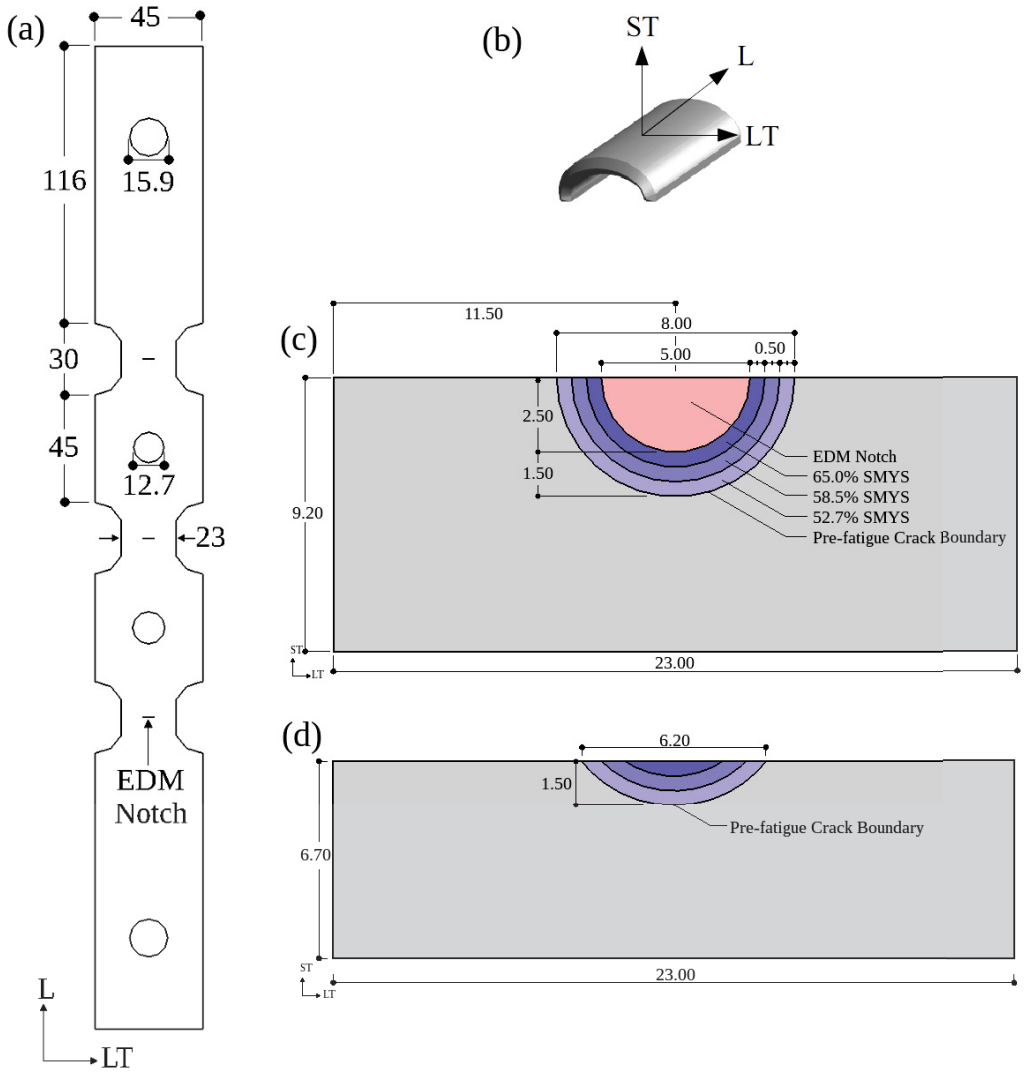

Figure 3.1: Summary of sample preparation prior to coating application. (a) Schematic of samples; (b) Pipe section with longitudinal (L), short-transverse (ST), and long-transverse (LT) directions indicated for reference; (c) Sample cross-section after EDM machining and pre-cracking (the maximum stresses used during each load step are indicated); (d) Sample cross-section after milling. Dimensions shown are in mm. Note that variability in crack length and depth was present.

Table 3.3: Sample thicknesses and widths in [mm] *Denotes prior testing with constant amplitude loading.

Waveform	**Initial Thickness** (t_o)	**Final Thickness** (t)	**Width** (W)
10 s ULH	9.2	6.4	22.9
30 s ULH*	9.2	6.8	23.0
60 s ULH	9.3	6.6	23.0
250 s ULH	9.2	6.7	23.1
500 s ULH*	9.2	6.7	23.0
Average	9.2 ± 0.1	6.6 ± 0.2	23.0 ± 0.1

Table 3.4: Initial aspect ratio $2c_0/a_0$.

Waveform	**Hydrogen**	**Exposed**	**Air**
10 s ULH	6.1	6.2	5.5
30 s ULH	4.3	4.7	4.8
60 s ULH	6.4	9.0	6.6
250 s ULH	6.4	5.4	6.0
500 s ULH	7.3	7.3	6.2
10 s +CA	7.6	7.7	6.3
500 s CA	4.9	4.9	4.8

A composite PLA/epoxy polymer coating was applied to cover the back and sides of the sample in order to better simulate exposure to only the outer surface of the pipe. Subsequently, two sets of epoxy coatings were applied to the samples in order to isolate the effects of mechanical driving forces and hydrogen ingress. The coatings are shown in Figure 3.2. The "Air" coating isolates the crack from direct exposure to solution, as well as keeping a sufficient coated area so that hydrogen diffusion lateral to the crack tip is limited. Similarly, the "Hydrogen" coating isolates the crack from direct exposure to solution, but the relatively narrow coating still allows for hydrogen absorbed into the steel to diffuse to the crack tip. "Exposed" cracks are fully exposed to solution and no coatings were applied. Stainless steel shims were spot welded onto the sample for connection to cathodic polarization during testing.

Following spot welding, the samples were sealed into a polymethyl methacrylate (PMMA) environmental chamber using silicone room-temperature vulcanization (RTV) sealant. Note that the testing cell is sealed with rubber o-rings at the top and bottom, but silicone sealant was also applied to all mating surfaces to prevent oxygen ingress. Any openings between the sample and the environmental cell was also sealed with several layers of silicone, with a minimum of 24 h between each application of sealant and a minimum of 48 h prior to solution filling. A schematic of the cell with the relevant cathodic protection connections are shown in Figure 3.3.

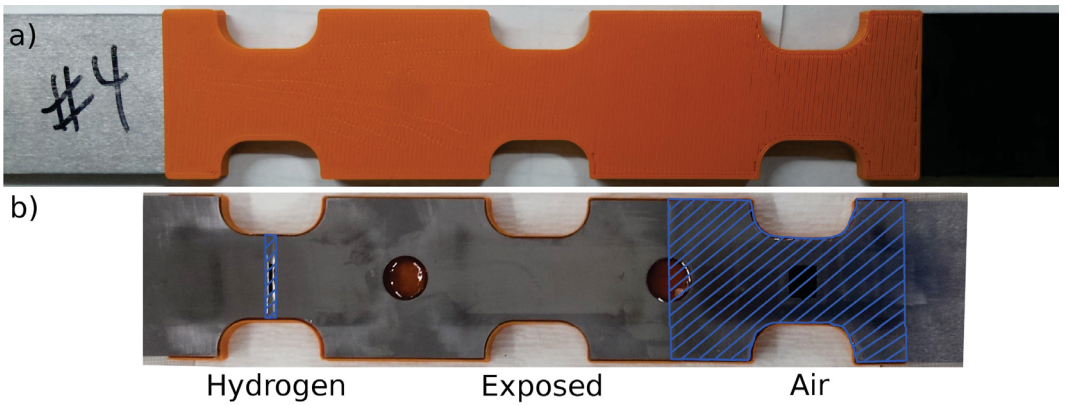

Figure 3.2: Macroscopic images of a) PLA/epoxy composite coating on back and sides of samples and b) epoxy coatings on front side of sample. Coatings to isolate the effects of hydrogen (labeled "Hydrogen") and mechanical driving forces (labeled "Air") are highlighted in blue.

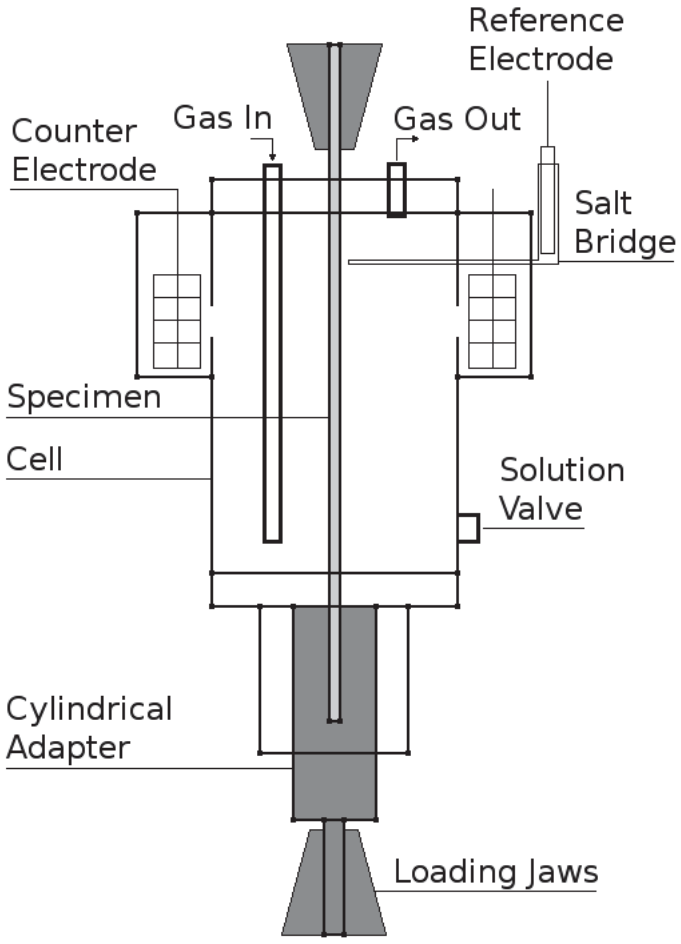

Figure 3.3: Schematic of cell used to simulate near-neutral groundwater conditions during testing.

3.3 Simulation of NNpH Environment

A dilute groundwater solution, named C2, was prepared from deionized water (with a resistivity of 18.2 MΩ·cm) in order to simulate NNpH groundwater conditions. The concentrations of species present in solution are summarized in Table 3.5. A gas mixture of 5% CO_2 balanced with N_2 was sparged into the solution for at least 48 hours prior to testing to ensure complete mixing, as well as during testing to maintain anaerobic conditions at a stable pH value of 6.29 [40]. Positive pressure was maintained throughout testing to prevent oxygen ingress. Before exposing the samples to C2, pH measurements were taken to verify compositional control using the Accumet XL60 pH meter. Prior to any pH measurements, the pH probe (accumet 13-620-530A) was calibrated in standard buffer solutions with a pH of 4, 7, and 10. To prevent cross-contamination, the pH probe was rinsed with deionized water and dried with lint-free wipes between calibrations and measurements.

Table 3.5: Composition of C2 solution. The typical value for pH is 6.29 after bubbling with 5% CO_2 / bal N_2.

Reagent	**Concentration [g/L]**
$MgSO_4 \cdot 7\ H_2O$	0.0274
$CaCl_2$	0.0255
KCl	0.0035
$NaHCO_3$	0.0195
$CaCO_3$	0.0606

3.0 M KCl-agar salt bridges were prepared in order to establish an electrical connection from the sample to the reference electrode. The saturated calomel electrode (SCE) was used as a reference (Fisher Scientific accumet 13-620-57). The sample was then connected as the working electrode to a potentiostat (Teknet EG&G-363) and Pt mesh (45 mm x 15 mm) was used as counter electrodes. The sample was then cathodically polarized at -900 mV_{SCE} and subsequently immersed in C2 solution for at least 10 days prior to loading. Exposure to solution prior to loading was performed in order to pre-charge the sample with hydrogen and minimize transient effects of hydrogen diffusing into the sample during loading. The time of pre-charging was based on the assumption of a hydrogen diffusivity $D_H = 2 \times 10^{-7}\,cm^2\,s^{-1}$ [39] reaching a minimum depth of 4.2 mm, using a simple estimate with Fick's law. See Equation 3.1 for the time calculation. Although the peak equilibrium flux would take longer to establish, the pre-charging

time was used to minimize a significant hydrogen concentration gradient during initial loading.

$$t = \frac{x^2}{D_H} \tag{3.1}$$

3.4 Loading Conditions

The sample was then loaded into an Instron 8516 servohydraulic loading frame, computer-controlled with the Instron Series IX Automated Materials Tester Software. Pinhole loading was applied at the bottom of the samples via a cylindrical adapter in order to minimize misalignment and multiaxial loading. Care was taken to maintain appropriate PIDL values in order to ensure accurate load application. Most tests performed were using an underload and hold (ULH) waveform, as shown schematically in Figure 3.4. Two constant amplitude (CA) tests were also performed to determine differences between constant amplitude loading and the addition of a hold. All loading conditions are summarized in Table 3.6 and testing durations are summarized in Table 3.7. From the work by Zhao et al. [14, 16], the typical number of underloading events in either liquids or gas transmission pipelines is approximately 500 per year. Note that the ULH loading simulated about 1 year's worth of liquids pipeline operation, while the CA loading would be equivalent to about 2 years' worth of liquids pipeline operation.

A maximum stress of 80% SMYS was chosen as a conservative estimate corresponding to the maximum allowable stress for CSA Z662-15 straight pipe in Class 1 locations with an assumed location factor, joint factor, and temperature factor of 1 [146]. Furthermore, a stress ratio of $R = 0.1$ was chosen in order to simulate highly aggressive loading conditions. The maximum stress intensity factor ($K_{\max}$) was calculated with the Newman and Raju stress intensity solution for a semielliptical surface flaw in a flat plate with $a \leq c$ [51]. The combined factor (CF) based on the work by Chen et al. [40] was also calculated. Relevant loading parameters are summarized in Tables 3.8 to 3.10.

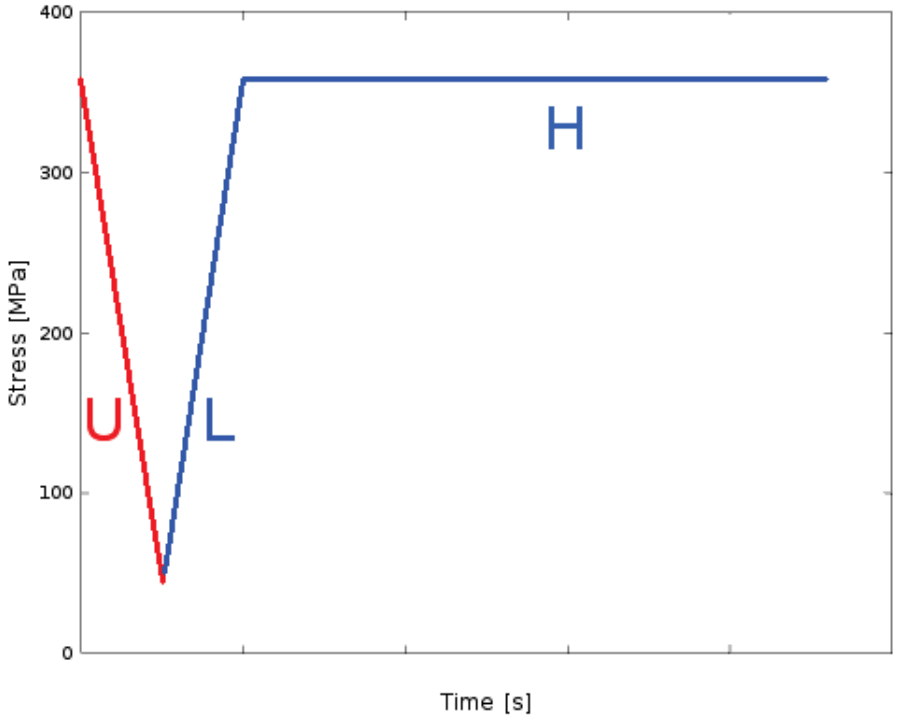

Figure 3.4: Generic underload waveform with hold. U designates unloading to a stress ratio $R = 0.1$, L designates loading over 500 s to 80% SMYS, and H designates the 1 hr hold.

Table 3.6: Loading durations and frequencies for all tests conducted. A cathodic potential of -0.9V_{SCE} was applied to all tests. *performed after testing the 500 s CA loading. **performed after testing the 10 s positive sawtooth CA loading.

Unload	Load	Frequency	Hold
10 s	500 s	1.96×10^{-3} Hz	1 hr
*30 s	500 s	1.89×10^{-3} Hz	1 hr
60 s	500 s	1.79×10^{-3} Hz	1 hr
250 s	500 s	1.33×10^{-3} Hz	1 hr
**500 s	500 s	1.00×10^{-3} Hz	1 hr
10 s	500 s	1.96×10^{-3} Hz	0
500 s	500 s	1.00×10^{-3} Hz	0

Table 3.7: Testing durations for all tests conducted.

Waveform	Precharge [days]	Sequences	Test [days]
10 s ULH	12	586	28
30 s ULH	12	436	21
60 s ULH	20	575	30
250 s ULH	13	412	21
500 s ULH	12	406	30
10 s +CA	13	1130	6
500 s CA	12	1125	13

Table 3.8: Initial stress intensity factor at the surface and in the depth $K_{\max}$ [MPa m$^{0.5}$].

	Depth $K_{\max}$			**Surface $K_{\max}$**		
Waveform	**Hydrogen**	**Exposed**	**Air**	**Hydrogen**	**Exposed**	**Air**
10 s ULH	19.0	19.3	20.1	12.0	12.1	13.4
30 s ULH	20.6	20.8	20.6	15.6	15.0	14.8
60 s ULH	17.0	12.9	17.4	10.5	6.7	10.6
250 s ULH	17.0	19.1	19.1	10.5	12.8	12.3
500 s ULH	16.8	16.9	18.9	9.7	9.8	11.9
10 s +CA	16.3	16.5	18.8	9.2	9.3	11.7
500 s CA	19.8	20.5	20.5	14.1	14.5	14.6

Table 3.9: Initial stress intensity factor range at the surface and in the depth ΔK [MPa m$^{0.5}$].

	Depth ΔK			**Surface ΔK**		
Waveform	**Hydrogen**	**Exposed**	**Air**	**Hydrogen**	**Exposed**	**Air**
10 s ULH	17.1	17.3	18.1	10.8	10.9	12.1
30 s ULH	18.5	18.7	18.5	14.1	13.5	13.3
60 s ULH	15.3	11.6	15.6	9.5	6.0	9.5
250 s ULH	15.3	17.2	17.2	9.5	11.5	11.0
500 s ULH	15.1	15.2	17.1	8.8	8.8	10.7
10 s +CA	14.7	14.8	16.9	8.3	8.3	10.5
500 s CA	17.8	18.4	18.4	12.7	13.1	13.1

Table 3.10: Combined factor in the depth and at the surface $[1 \times 10^3\,\mathrm{MPa}^3\,\mathrm{m}^{3/2}\,\mathrm{s}^{0.1}]$.

	$CF_{\mathbf{depth}}$			$CF_{\mathbf{surf}}$		
Waveform	**Hydrogen**	**Exposed**	**Air**	**Hydrogen**	**Exposed**	**Air**
10 s ULH	10.3	10.8	12.2	2.6	2.7	3.6
30 s ULH	13.2	13.6	13.3	5.8	5.1	4.9
60 s ULH	7.5	3.3	8.0	1.8	0.5	1.8
250 s ULH	7.8	10.9	11.0	1.8	3.3	2.9
500 s ULH	7.7	7.8	11.0	1.5	1.5	2.7
10 s +CA	6.6	6.7	10.0	1.2	1.2	2.4
500 s CA	12.6	13.9	13.9	4.5	5.0	5.0

3.5 Test Takedown and Post-Test Processing

After the loading sequences were completed, samples were carefully taken out of solution to minimize corrosion. Additionally, solution samples were taken from the bulk solution and the anode chambers and the pH of the solutions was then measured. The steel samples were sprayed with ethanol during test takedown to wash off any water from the cracks prior to removal from the PMMA cell. Following removal from the cell, the coatings were removed and the steel samples were immersed in an ultrasonic bath of ethanol. The sample was then placed in ultrasonic baths in acetone and a second round of ethanol to remove any water and loosely-adhered oxides from the crack surfaces. The samples were then sectioned for later SEM analysis with an approximate length and width of 30 x 8 mm, respectively.

3.6 Surface Crack Characterization

The Zeiss EVO LS15 EP-SEM (EVO) was used for imaging the post-test crack at the sample surfaces. The secondary electron (SE) mode was primarily used for post-test cracks in order to more accurately characterize the surface topography. Post-test cellulose acetate replicas were taken for future reference.

Following SE-mode characterization, the samples were lightly polished with Buehler MetaDi 1 µm oil-based diamond suspension in order to remove any surface oxides and expose the crack tip more clearly. The samples were re-imaged in the EVO. The backscattered electron (BSE) mode was primarily used to image polished cracks for higher-contrast imaging of the crack morphology. After imaging of the lightly-polished samples, the samples were subsequently polished to a 1 µm finish to show the crack morphology. The samples were re-imaged in the EVO using the BSE mode. Cellulose acetate replicas were taken of the polished surfaces for future reference.

The samples were then cross-sectioned at approximately 2/3 of the crack length (taken from the left side). The left-hand side (LHS) was taken for later fractographic analysis and the right-hand side (RHS) was taken for characterization of the depth profile. A schematic is shown in Figure 3.5a.

3.7 Fractographic Analysis

The LHS samples were first cut perpendicular to the crack length as close to the crack tip as possible in order to minimize the total fracture area. Furthermore, the samples were reduced to a final length (parallel to the sample length) and thickness of 30 mm x 1.5 mm, respectively, as shown in Figure 3.5b. Samples were notched with a diamond-tipped scribe along the crack length on the back side of the crack. Following immersion in liquid nitrogen for at least 3 hours, the samples were fractured with a cold chisel. Fractured samples were promptly placed in an ultrasonic bath in acetone and then ethanol to prevent oxidation and remove any debris on the surface.

The EVO was used in both BSE and SE mode to image the crack fracture surfaces. Furthermore, energy dispersive x-ray spectroscopy (EDX) analysis was conducted using the Bruker EDX system outfitted onto the EVO. EDX point scans were taken with an accelerating voltage of 20 kV, resulting in typical counts between 2 kcps and 7 kcps. The Bruker software's Bremsstrahlung filter was used to remove background noise. Additional imaging using the Zeiss Sigma 300 VP-FESEM (Sigma) was performed for high-magnification imaging of microscopic features using the secondary electron in-lens detector. The in-lens mode was used to reduce noise from electrons interacting with the SEM walls and specimen stage that are subsequently detected by the SEII detector.

Oxide removal was performed on fracture surfaces corresponding to Side A (see Figure 3.5b) to remove any corrosion product from testing and allow for clearer imaging of the fracture surfaces. The oxide removal solution consisted of 6N HCl and 3.5 g/L hexamethylenetetramine in an aqueous solution [147]. The oxide removal solution was used in the work by Engel [144] and follows ASTM Standard G1-03, solution C.3.5. Samples were immersed in oxide remover for only a few seconds (between 1 s and 4 s) to ensure minimal damage of microscopic features. Following oxide removal, the cracks were rinsed with ethanol, sonicated in an ethanol bath, and then air-dried. Further imaging using the Sigma was performed in SE and InLens modes for resolving microstructurally fine features.

3.8 Depth Profile Characterization

Following sectioning (schematic shown in Figure 3.5c), the RHS samples were subsequently polished to a 1 µm finished to expose the crack morphology in the depth. The depth profiles were imaged using the EVO in BSE mode. The surface profiles were re-imaged in order to obtain the remaining crack length at the surface. The length fraction x was calculated as the ratio between the remaining surface length in the corresponding cross-section relative to the total surface length. After imaging the depth profiles, samples were etched in 2% nital and re-imaged using the EVO in BSE mode.

3.9 Measurement Methods

This section will outline some finer details with how measurements were performed in order to minimize measurement errors. Key criteria to define growth regions and microstructures are also outlined. Fiji, based off of ImageJ, was used to take all measurements from micrographs [148].

3.9.1 Depth Growth

Using low-magnification SEM micrographs of the full crack, the distance from the top surface to the crack wall was used to determine the final depth. Higher-magnification

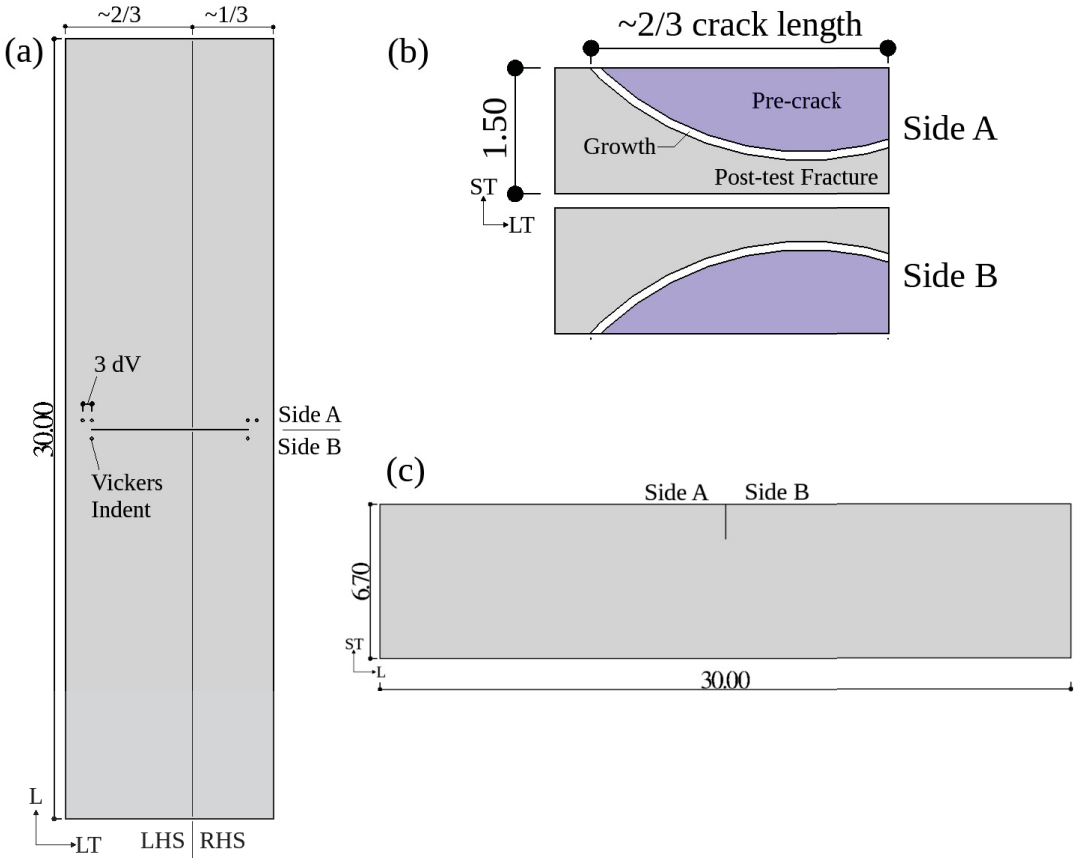

Figure 3.5: Schematics of (a) sample surface after testing and subsequent sectioning; (b) fracture surfaces from the LHS; and (c) depth profiles taken from the RHS. dV in Figure (a) denotes the end-to-end distance of a Vickers indent. dV was typically on the order of 100 µm. Dimensions shown are in mm.

images were used to directly measure the growth region and the initial depth was calculated based on the difference between the final depth and the depth growth.

3.9.2 Surface Growth

Similarly, a combination of low- and high-magnification images were used to determine the surface growth. Using a series of high-magnification SEM micrographs taken from replicas, post-testing, and post-polishing (see Figure 3.6), several control points were taken as a reference on the low-magnification micrographs stitched together to generate a full-crack image (see Figure 3.7). In order to account for shrinkage or stretching of the replicas, indent-to-indent lengths were used to apply a correction factor to the replicas, in a process similar to Engel [144]. Equation 3.2 shows the adjusted pretest measurement.

$$2c_{0,\mathrm{adj}} = 2c_{0,\mathrm{meas}} \cdot \left(\frac{1}{3}\right)\left(\left[\frac{d_{1,\mathrm{pre}}}{d_{1,\mathrm{post}}}\right] + \left[\frac{d_{2,\mathrm{pre}}}{d_{2,\mathrm{post}}}\right] + \left[\frac{d_{3,\mathrm{pre}}}{d_{3,\mathrm{post}}}\right]\right) \tag{3.2}$$

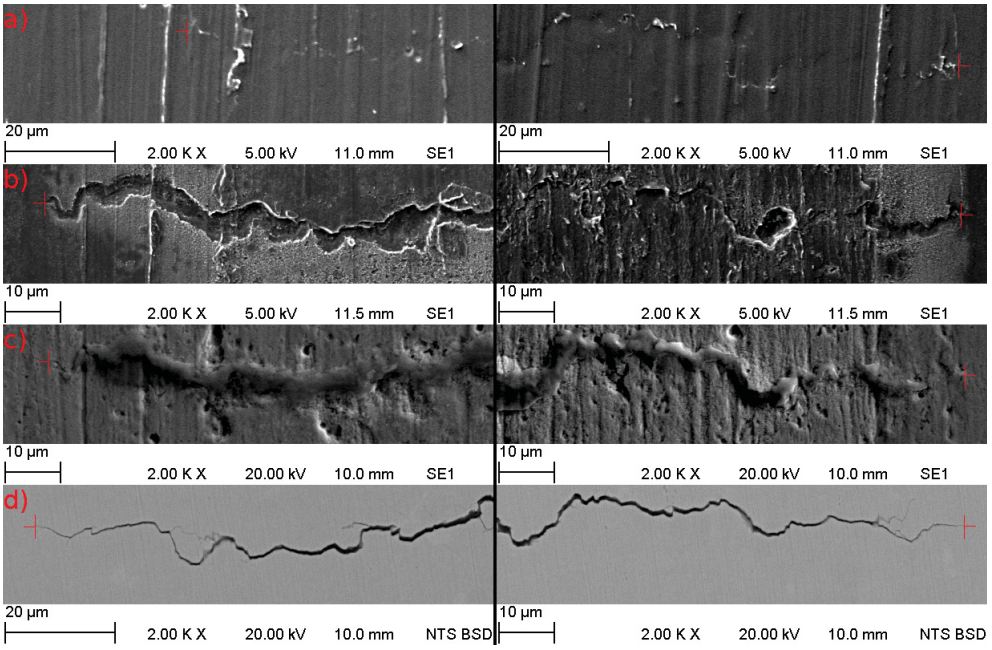

Figure 3.6: SEM micrographs of (a) pre-test replicas; (b) post-test replicas following 10 s CA loading; (c) post-test image following 500 s ULH loading; and (d) post-polishing image for the "Air" crack. Red crosshairs indicate crack tip.

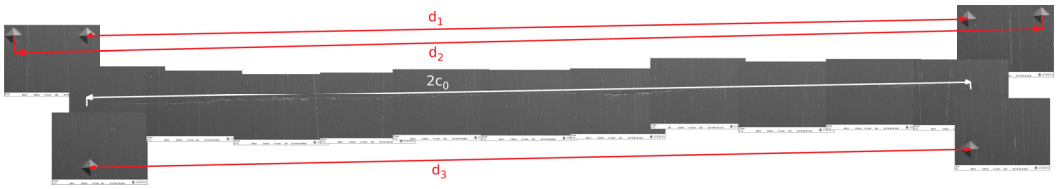

Figure 3.7: SEM-SE stitched micrograph of pre-test replica prior to 10 s CA loading and subsequent 500 s ULH loading for the "Air" crack.

Chapter 4

Effect of Hold

4.1 Overview

This chapter will focus on the effect of a monotonic hold at the maximum stress, with intermittent cyclic loading. Crack growth rates as a function of the combined factor [39], fractography micrographs, energy-dispersive x-ray spectroscopy (EDX), and crack morphologies will be used to compare crack behaviour in a simulated inert environment (fully coated), near-neutral pH dilute bicarbonate solution (fully exposed), and a thinly coated specimen to simulate a hydrogen-rich environment with no anodic dissolution. Tabulated data corresponding to the graphs can be found in Appendix A and additional micrographs can be found in Appendix B.

4.2 Results

4.2.1 Crack Growth Rates vs Combined Factor

Figure 4.1 shows the crack growth rates per cycle as a function of the combined factor within various environments. In air, the depth crack growth rates show minimal variations with respect to the respective mechanical driving force. However, the symmetrical, 500 s ULH showed no observable growth at the surface. Please note that the 10 s +CA waveform showed some growth at the surface, despite having a slightly lower combined factor. The crack growth for fully exposed cracks shows a similar trend as observed in air

– depth growth rates are comparable for similar combined factors regardless of waveform type. Further, the 500 s ULH waveform did not show appreciable growth at the surface while the 10 s +CA waveform showed growth. In the partially-coated cracks, increased crack growth in the depth was observed as the combined factor increases. Conversely, crack growth at the surface decreases as the combined factor increases.

4.2.2 Fractographic Images

For reference, the scanning electron microscopy back-scattered electron (SEM-BSE) micrographs of the fracture surfaces resulting from full exposure to C2 solution are shown in Figures 4.2, 4.3, and 4.4. Please note the differences in morphology of the darker regions (Region 1) from the micrographs. The fracture surface from Figure 4.2 shows a larger spread of darker regions (Region 1), while Figures 4.3 and 4.4 show a darker region near the outer surface. The chemical compositions from EDX point analysis corresponding to the numbered regions in the annotated fractographs will be discussed in a later section.

Figures 4.5 to 4.7 show typical medium magnification SEM-SE micrographs of the fracture surfaces corresponding to the "Air", "Exposed", and "Hydrogen" environments. The remainder of the fracture surface micrographs are shown in Appendix B. Due to the larger number of cycles performed in the constant amplitude waveforms, a larger growth region was observed when compared with the underload and hold waveforms. This section will outline the various microscopic features used as criteria to determine where the growth zones end and begin.

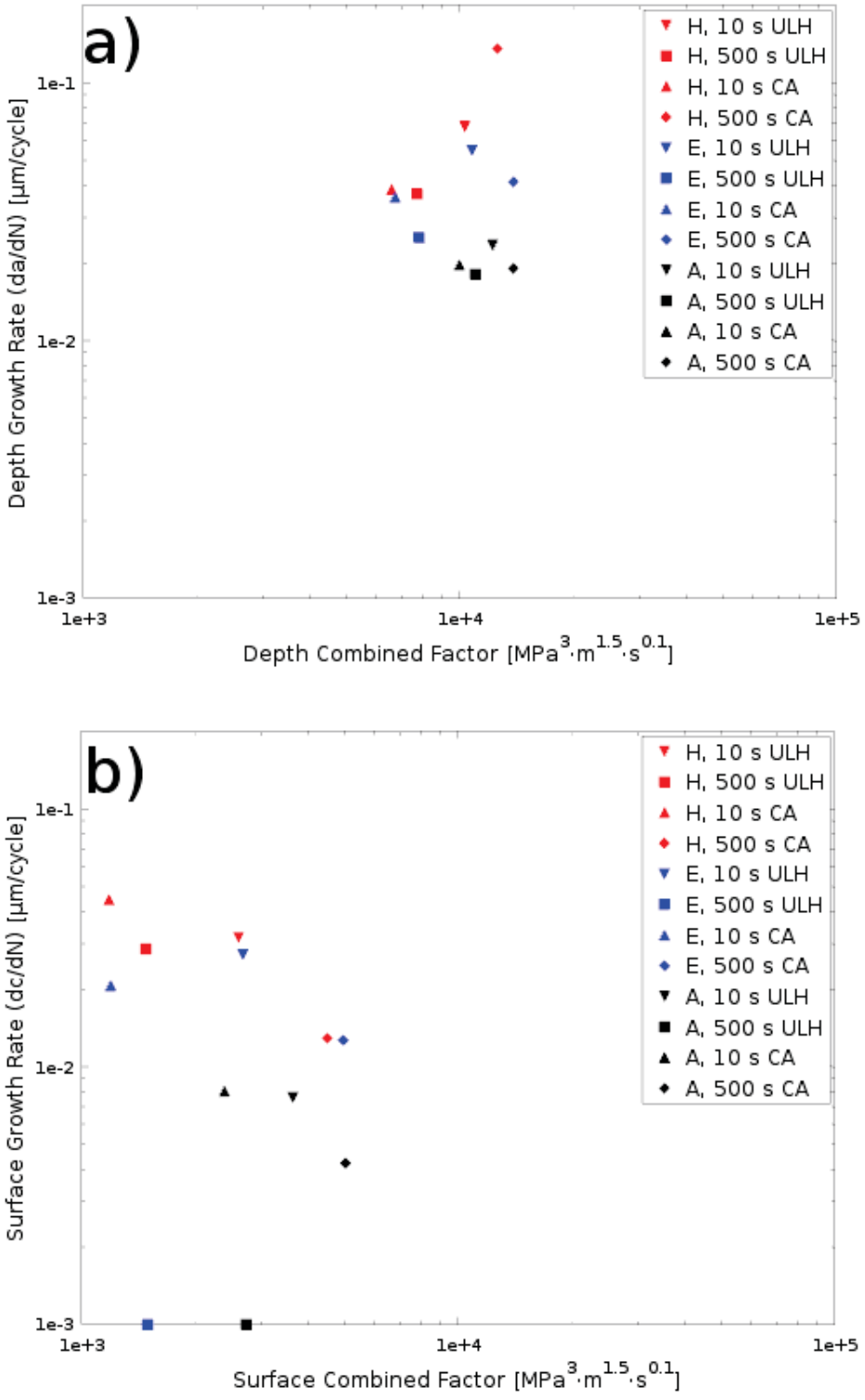

Figure 4.1: Growth per cycle as a function of combined factor a) in the depth and b) at the surface for the "Hydrogen", "Exposed", and "Air" environments.

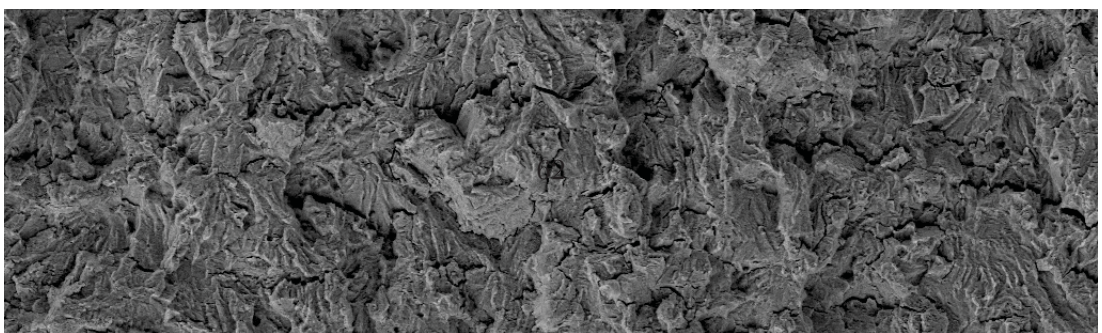

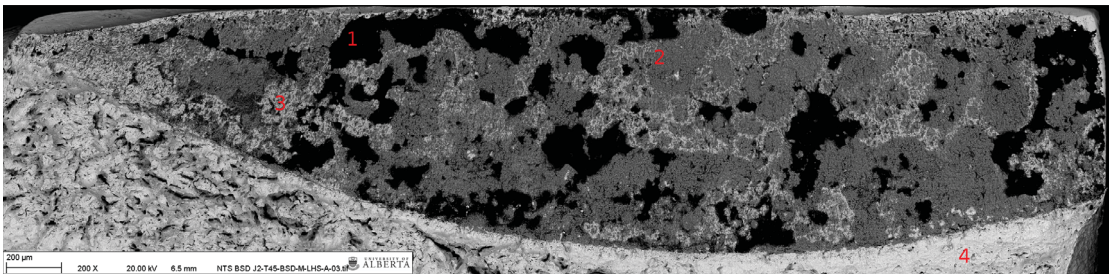

Figure 4.2: SEM-BSE micrograph of "Exposed" fracture surface loaded with 10 s unloading, 500 s ramp, and 1 h static hold.

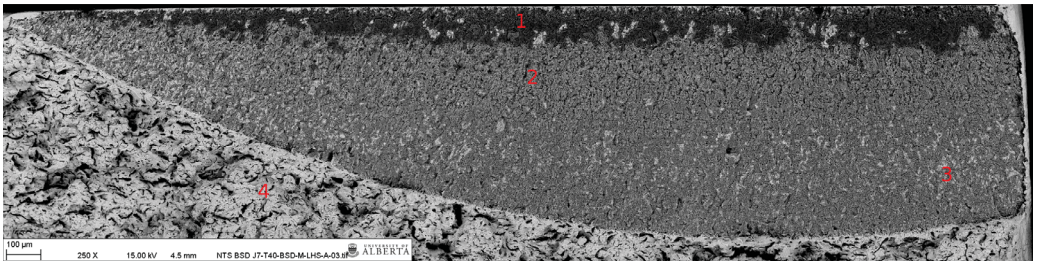

Figure 4.3: SEM-BSE micrograph of "Exposed" fracture surface loaded with 10 s unloading and 500 s constant amplitude loading; subsequent testing with 500 s unloading, 500 s ramp, and 1 h static hold was performed.

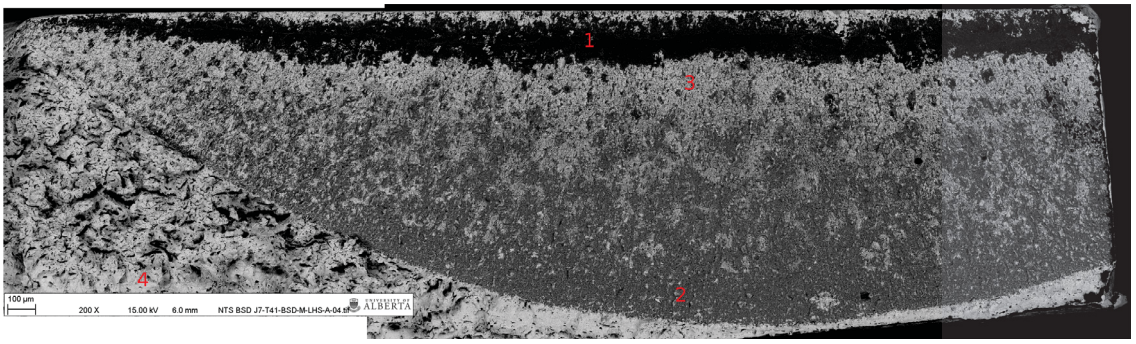

Figure 4.4: SEM-BSE micrograph of "Exposed" fracture surface loaded with 500 s constant amplitude loading; subsequent testing with 30 s unloading, 500 s ramp, and 1 h static hold was performed.

Because the pre-fatigue crack growth was performed in air, growth in the "Air" environment is expected to have similar features, as seen in Figure 4.5. Significant changes in the surface topography or sudden changes in the step patterns of growth were used as a reference to separate pre-fatigue crack growth and crack growth from testing in the simulated "Air" environment.

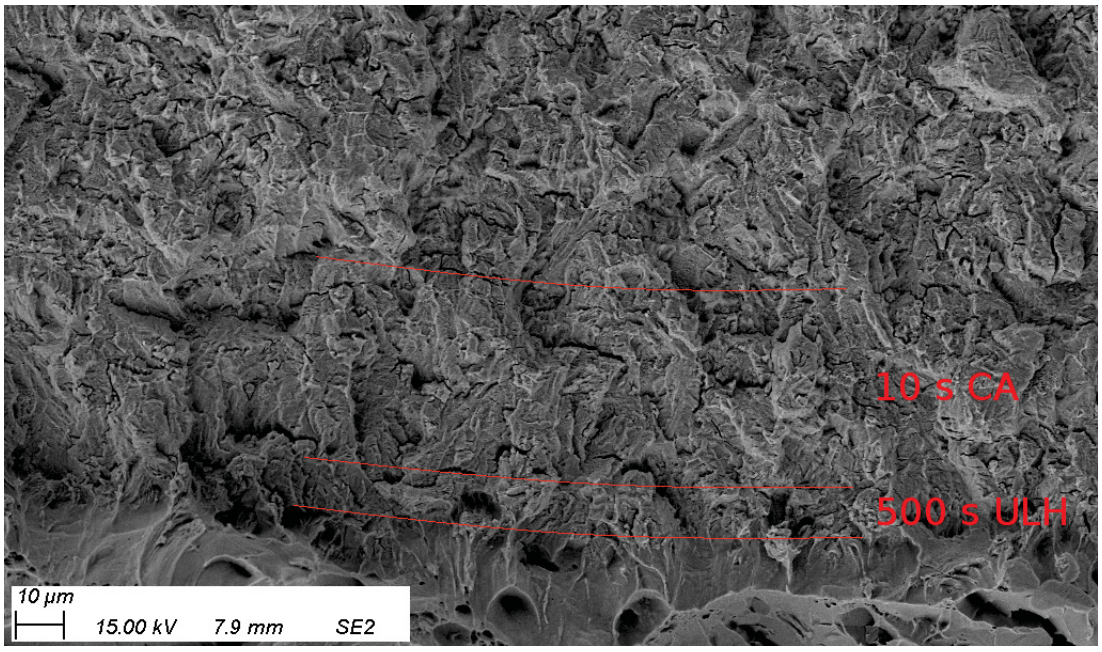

Figure 4.6: SEM-SE micrograph of "Exposed" crack growth band at the depth. Loading conditions are indicated on the image. Red lines indicate growth. Micrograph was taken after oxide removal.

After the minimum 12 day hydrogen pre-charging and at least 21 days of loading in the underload and hold spectra, corrosion product and/or calcareous deposits were observed in all "Exposed" cracks. Please note that Figure 4.6 was taken after oxide removal. Because the "Hydrogen" cracks (example shown in Figure 4.7) were isolated from direct exposure from C2 solution, little phase contrast was detected between the pre-fatigue crack region and growth zone. However, flat features were observed and the onset of larger faceted areas (prior to the post-test fracture zone) was used to define the beginning of the growth zone from testing.

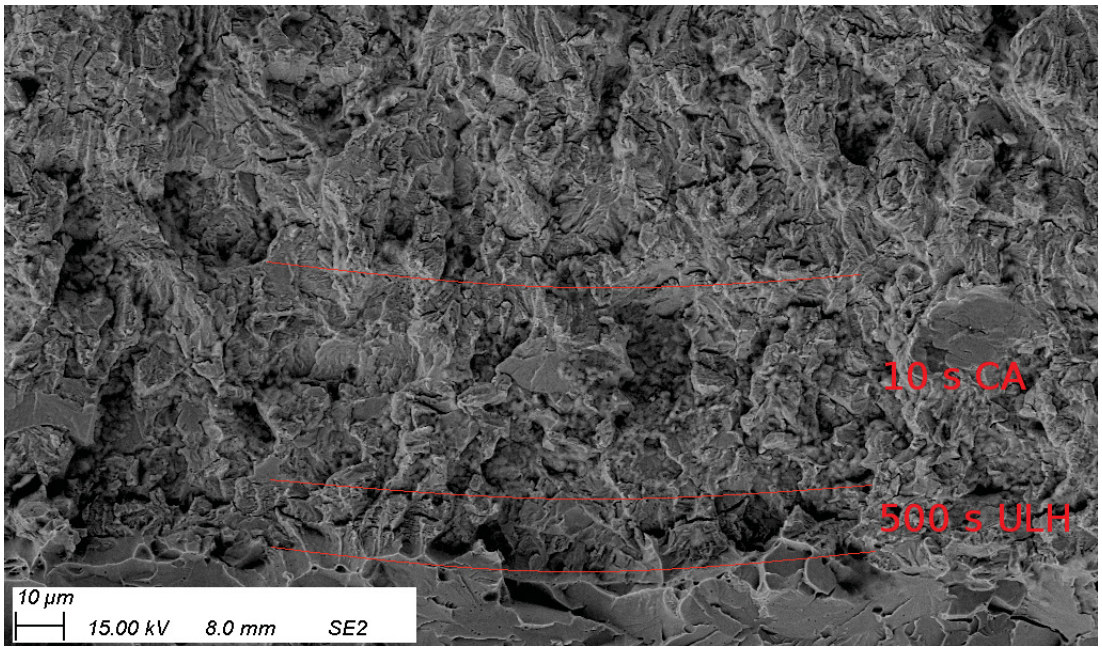

Figure 4.7: SEM-SE micrograph of "Hydrogen" crack growth band at the depth. Loading conditions are indicated on the image. Red lines indicate growth. Micrograph was taken after oxide removal.

4.2.3 Through-Thickness Crack Morphology

The SEM-BSE micrographs following various loading conditions are shown in Figures 4.8, 4.9, and 4.10. As seen in Figure 4.8, the "Hydrogen" and "Air" profiles show a sharp crack tip. However, the "Exposed" crack shows some crack wall dissolution during the hydrogen pre-charging period, indicating incomplete cathodic protection near the crack tip. However, subsequent growth during testing reveals a sharp crack tip.

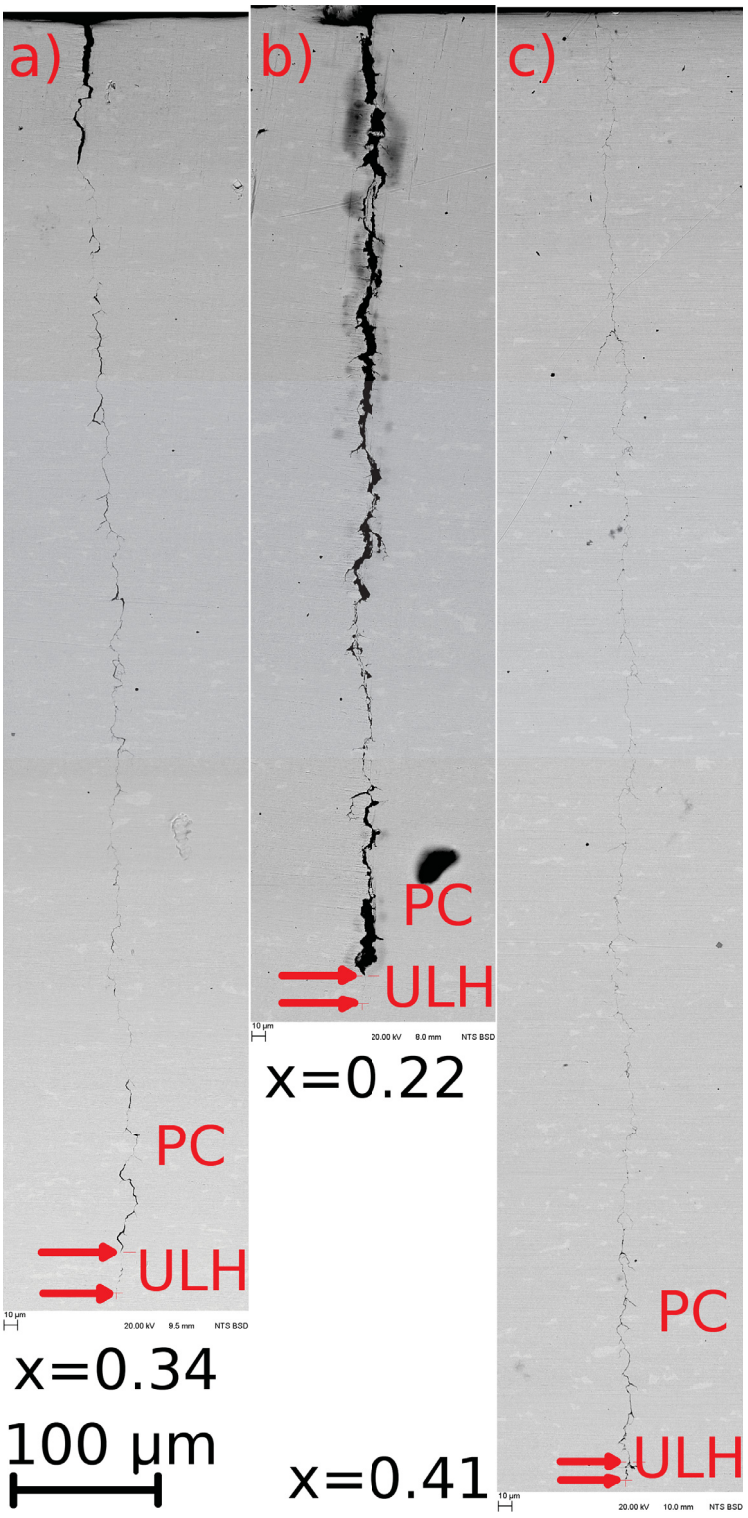

Figure 4.8: SEM-BSE micrographs of (a) "Hydrogen", (b) "Exposed", and (c) "Air" crack depth profiles. Red arrows indicate the crack tip corresponding to precracking (PC) and 10 s unloading, 500 s loading, and 1 hour hold (ULH). The approximate length fraction x is indicated beside the corresponding images. Images were taken with an acceleration voltage of 20 kV and working distances were between 8.5 mm and 10.0 mm.

Figure 4.9 shows some morphological differences in the crack profiles for "Exposed" cracks, indicating more observable dissolution near the crack tip with a faster unloading rate. One potential cause for the differences would be from mass transport due to advection of entrapped solution within the crack, and restoration of fresh fluid from the bulk solution.

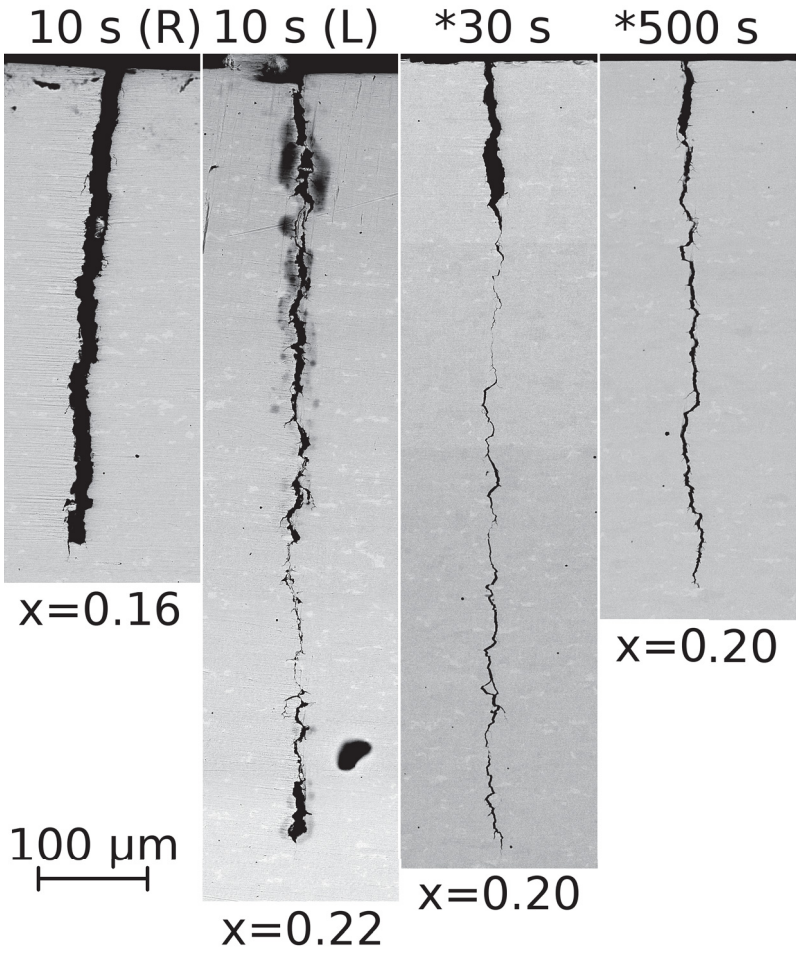

Figure 4.9: SEM-BSE micrographs of fully exposed crack depth profiles. The unloading times corresponding to underload and hold waveforms are shown and the approximate length fraction x is indicated beside the corresponding images. Images were taken with an acceleration voltage of 20 kV and working distances were between 7.5 mm and 10.5 mm. *Denotes prior constant amplitude loading.

Figure 4.10 shows a higher-magnification image of the depth profiles, following etching. All three crack environments displayed transgranular crack growth, consistent with near-neutral pH corrosion fatigue and inert fatigue in general. Crack tip bifurcation and some branching were observed during pre-fatigue crack growth.

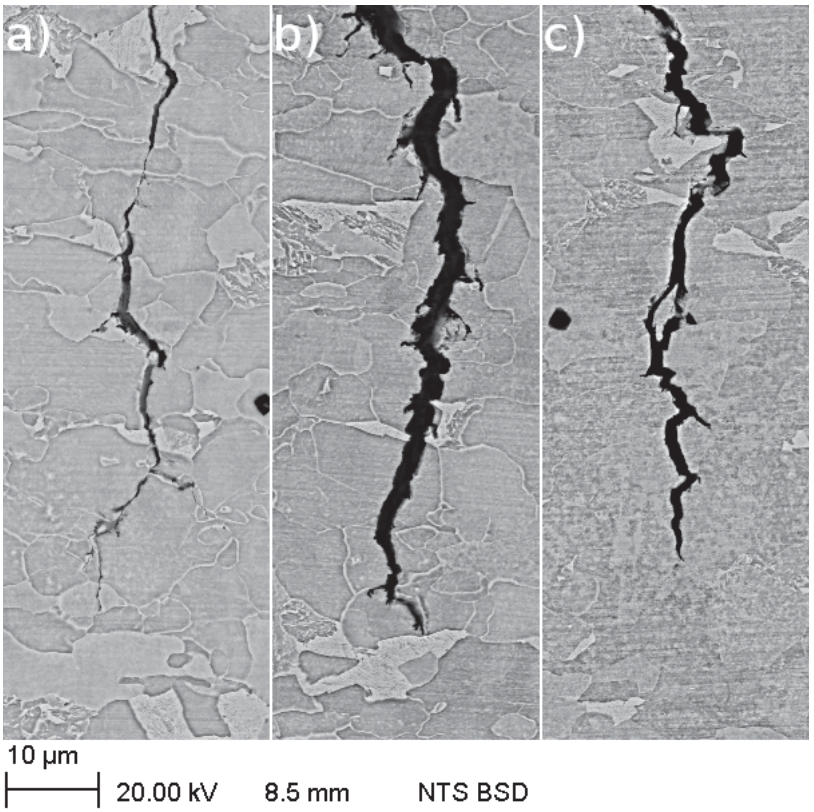

Figure 4.10: SEM-BSE micrographs of etched samples exposed to (a) "Air", (b) "Exposed", and (c) "Hydrogen" environments for 10 s unloading and 500 s constant amplitude loading and subsequent 500 s unloading, 500 s loading, and 1 hour hold. Images were taken with an acceleration voltage of 20 kV and working distances were between 8.0 mm and 8.5 mm.

4.2.4 Crack Morphology at the Surface

The surface profiles following etching are shown in Figure 4.11. As noted in Figure 4.11a, the "Air" crack follows a typical transgranular path. The "Exposed" crack (Figure 4.11b) shows some blunting at the crack tip, likely due to insufficient cathodic protection during hydrogen pre-charging. Finally, Figure 4.11c shows some discontinuous crack growth in the "Hydrogen" crack, where microcracks initiate beyond the crack tip but within the fracture process zone, and eventual growth connects the original crack with the new hydrogen cracks.

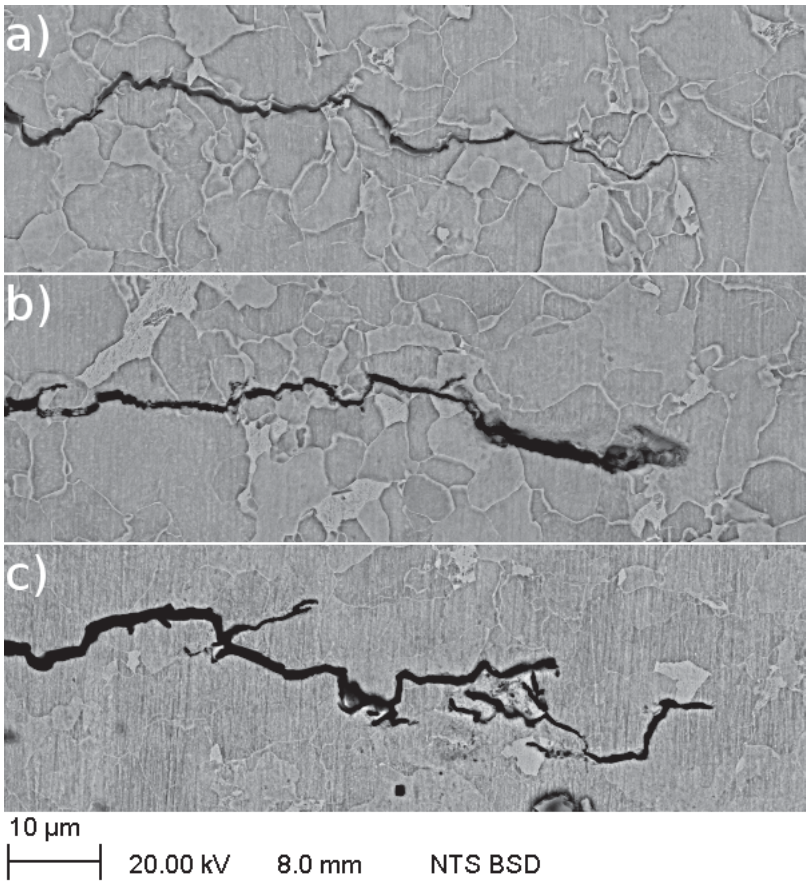

Figure 4.11: SEM-BSE micrographs of etched samples exposed to (a) "Air", (b) "Exposed", and (c) "Hydrogen" environments for 10 s unloading and 500 s constant amplitude loading and subsequent 500 s unloading, 500 s loading, and 1 hour hold. Images were taken with an acceleration voltage of 20 kV and working distances were between 8.0 mm and 8.5 mm.

4.2.5 Microscopic Features

Figure 4.12 shows typical fatigue striations observed for all three crack environments. These microscopic features confirm growth primarily through the cyclic nature of loading and not the monotonic hold.

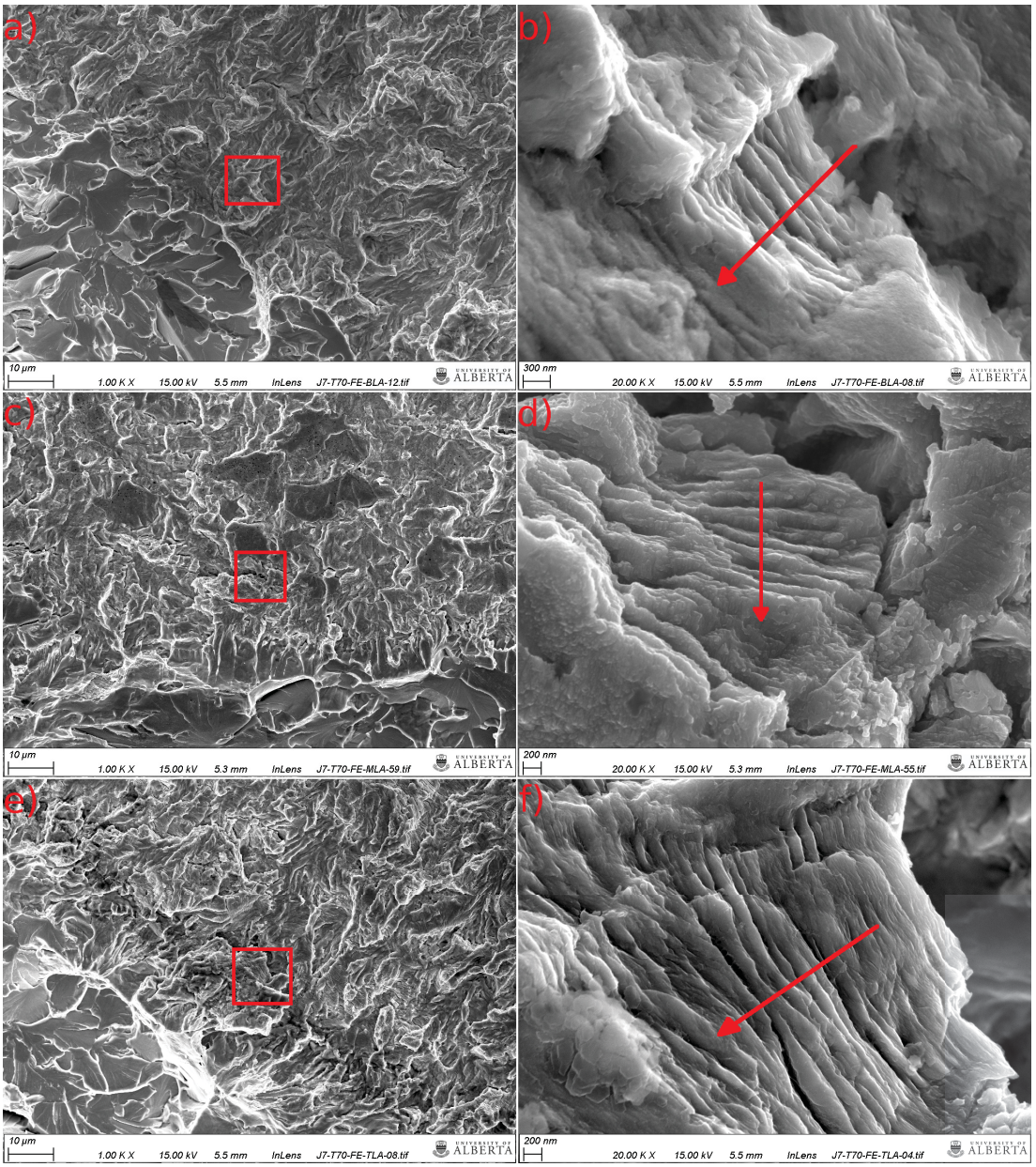

Figure 4.12: FESEM In-Lens micrographs of samples exposed to (a-b) "Air", (c-d) "Exposed", and (e-f) "Hydrogen" environments for 10 s unloading and 500 s constant amplitude loading and subsequent 500 s unloading, 500 s loading, and 1 hour hold. Images were taken with an acceleration voltage of 15 kV and working distances were between 5.3 mm and 5.5 mm. Red boxes in the left column denote the corresponding location for the higher magnification images in the right column. Arrows indicate the direction of crack propagation. Micrographs were taken after oxide removal.

4.2.6 Chemical Composition

Point analysis EDX results from the various deposits observed on the crack surfaces are summarized in Table 4.1. A few trends are readily observable from the data. The

darkest regions (Region 1), found near the top surface of the crack, typically have high amounts of Ca and O. Furthermore, lighter gray regions (Region 3) on the crack surface (typically just below the Ca- and O-rich regions at the top) show the presence of oxygen. Similarly, darker gray regions on the crack surface (Region 2 toward the crack wall) show higher amount of O, as well as trace amounts of Si.

Table 4.1: EDX results in wt.% for fully exposed cracks, with the balance being C and trace amounts of Si. Relevant loading conditions are shown below.

Region	Description	Loading Conditions	Fe	Mn	Ca	O
1	Darkest, Top Surface	10 s ULH	1.7	-	-	16.3
		10 s CA; 500 s ULH	9.4	-	65.3	17.6
		500 s CA; 30 s ULH	19.2	-	42.7	28.2
2	Darker, Crack Surface	10 s ULH	90.9	-	0.7	2.7
		10 s CA; 500 s ULH	73.5	-	19.0	-
		500 s CA; 30 s ULH	58.9	-	0.4	35.1
3	Lighter, Crack Surface	10 s ULH	73.8	-	0.9	17.1
		10 s CA; 500 s ULH	80.5	-	16.0	-
		500 s CA; 30 s ULH	87.9	-	-	7.1
4	Cleavage	10 s ULH	97.1	2.2	-	-
		10 s CA; 500 s ULH	94.7	-	-	-
		500 s CA; 30 s ULH	96.6	2.4	-	-

4.3 Discussion

The addition of a monotonic hold in near-neutral pH environments has been previously shown to retard crack growth in pipeline steels. However, the effect of a monotonic hold following asymmetrical triangular loading has not yet been studied in this environment. Specifically, the effect of changing unloading rates on crack growth rates is not known for this set of conditions. This section will explore the mechanisms relevant to crack growth in air, fully-exposed, and hydrogen-rich environments. Understanding of these mechanisms may improve operations relevant to the integrity management of pipelines.

4.3.1 Crack Arrest due to Static Hold

In this study, pipeline steel specimens were loaded in variable amplitude and constant amplitude loading waveforms to explore how changing the unloading rate may affect crack growth rates under different environments. Via SEM fractography, crack growth

rates were estimated and the morphology of the crack walls, crack tip at the surface, and the crack tip in the depth direction indicated different responses to unloading rates for the three environments. For similar loading waveforms, the partially-coated cracks showed the highest crack growth rates as a result of hydrogen-enhanced crack growth in the absence of anodic dissolution. Next, the cracks exposed to C2 solution showed greater crack growth relative to the fully-coated cracks, indicating that crack sharpening related to hydrogen ingress has a greater effect than blunting effects due to anodic dissolution. Previous studies by Egbewande et al. [43] and Been et al. [50] support the finding that dissolution rates in the near-neutral pH environment are less significant compared to crack growth rates driven by mechanical loading, especially during Stage II crack growth.

Crack arrest was observed at the crack surface in fully coated cracks and cracks fully exposed to the near-neutral pH environment loaded under the 500 s ULH waveform. For the fully coated cracks, the crack tip remained sharp, indicating that no significant blunting from room-temperature creep had occurred. Further, recall that the maximum initial stress intensity factor $K_{\max}$ at the surface is relatively low, at $11.9\,\mathrm{MPa\,m^{0.5}}$. The sharp crack tip and no observed crack growth suggest that the mechanical driving force at the surface is insufficient to allow for propagation of the crack. Additionally, recall that plane stress conditions at the surface would not allow for further increases in hydrostatic stress ahead of the crack tip due to a lack of crack tip constraint in the through-thickness direction. Crack tip blunting was observed in the SEM micrographs of the crack tip at the surface of the specimen. Since crack arrest was also observed in the fully-exposed crack but not the partially-coated crack, we can infer that the mechanical driving forces even with the presence of hydrogen is insufficient to overcome the threshold for crack propagation as well as crack blunting due to anodic dissolution [78, 115], room-temperature creep [149], and hydrogen-enhanced plasticity effects [52]. Plane stress conditions at the surface crack tip would result in lower stresses and limit the effect of hydrogen segregation to the FPZ. However, a greater availability of hydrogen at the bulk surface of the specimen is expected.

Conversely, the addition of a hold had relatively little effect for crack growth in the depth direction. Crack growth in the depth direction were all within one order of magnitude for cracks in each environment. The low amount of scatter (da/dN all within one order of magnitude) may be related to the higher constraint at the crack tip, resulting

in plane strain conditions. Although a higher stress would result, the minor effect of adding a hold indicates that the fracture process zone is likely already saturated with hydrogen. Thus, more time spent at high stress did not result in significantly greater crack growth rates. Increased amounts of hydrogen would be expected as a consequence of hydrogen pre-charging prior to mechanical loading, as well as the application of a cathodic potential.

Similar studies of pipeline steels subjected to variable amplitude loading in a near-neutral pH environment have been performed. The work from Yu et al. [150] showed that underload cycling with a monotonic hold caused a decrease in crack growth rates. It is important to note that the stress ratio used in the study by Yu et al. [150] was 0.5, while the current study used $R = 0.1$. The lower R in the present study is be expected to yield less-pronounced effects of crack blunting (and therefore retardation of crack growth) from the static hold due to more aggressive loading as a result of a higher stress range during the underloading events.

Another difference is that the work by Yu et al. [150] used a loading frequency of 1.04×10^{-3} Hz which is equivalent to approximately one underloading event every 16 hours (as opposed to 1 hour in this study). Per a separate study by Yu et al. [64], an increased holding time generally decreases crack growth rates due to more effects of crack tip blunting. However, an increased hydrogen concentration can be expected to compete with blunting due to anodic dissolution and room-temperature creep. From the work of Chen et al. [136] and also Oehlert and Atrens [73], room temperature creep causing blunting is possible as a result of releasing stored energy in dislocations, especially with the inclusion of the 1-hour monotonic hold. A hold period of 60 minutes was noted to create the maximum retardation effect [64] due to sufficient exhaustion of mobile dislocations while minimizing high levels of hydrogen segregation to the crack tip.

It is important to note that the studies by Yu et al. [64, 150] used compact tension specimens at open-circuit potential as opposed to semi-elliptical surface cracks with an applied cathodic potential that were used in the current study. The increased proximity of the crack tip to the sample surface from the semi-elliptical cracks as well as the application of cathodic potential would be expected to encourage hydrogen segregation to the crack tip and reduce retardation effects from the 60-minute static hold. The

changed crack geometry and electrochemical conditions would likely result in a different critical length of time to achieve the maximum retardation effect.

These data suggest that unloading rate and the addition of a monotonic hold may be less significant for crack growth in the depth direction at this stress intensity range. At the surface, however, a monotonic hold may cause sufficient crack blunting to arrest crack propagation. Higher unloading rates may be able to activate a dormant semi-elliptical crack at the surface as a result of increased hydrogen.

Subsequent sections will elaborate on the role of applied stress in relation to the threshold for crack growth, the role of hydrogen, and the role of plastic damage related to room-temperature creep on the crack growth behaviour in the three environments tested.

4.3.2 Mechanical Driving Forces and the Threshold for Cracking

Variable amplitude loading performed on fully coated crack specimens was used to simulate fatigue in an inert environment. Plastic damage as a result of dynamic loading counteracted by room-temperature creep processes [149] is expected to dominate crack growth behaviour. The addition of a monotonic hold did not show significant influence on crack growth behaviour for the fully coated cracks. Although no crack growth at the surface was observed under the 500 s ULH waveform for the fully coated cracks, some crack growth was observed in the depth direction.

The work by Kim et al. showed a fatigue threshold ΔK_{th} of $3.32\,\text{MPa}\,\text{m}^{0.5}$ for X65 CT specimens loaded at a frequency of 20 Hz and a load ratio of 0.1 [24]. Kim et al. showed that at a relatively load ratio of 0.1, crack closure was not significant [24]. The X65 steels tested in the current study also had a primarily polygonal ferrite microstructure with a grain size on the order of 10 microns, which was observed in the work by Kim et al. [24]. The minimum stress intensity at the depth and surface were $12.9\,\text{MPa}\,\text{m}^{0.5}$ and $6.7\,\text{MPa}\,\text{m}^{0.5}$, respectively, and these were both greater than the noted threshold of $3.32\,\text{MPa}\,\text{m}^{0.5}$ per the study by Kim et al. [24]. Therefore, we can expect all cracks to show some growth in both directions.

One possible explanation for crack arrest observed in the current study may be the difference in crack geometries and test specimens. The semi-elliptical cracks may have

a higher fatigue threshold, especially considering added residual stresses from specimen machining.

The work by Egbewande et al. [43] note a combined factor threshold of $4570(\mathrm{MPa\,m^{0.5}})^3$ $\mathrm{Hz}^{-0.1}$ at the sample surface and $2869(\mathrm{MPa\,m^{0.5}})^3$ $\mathrm{Hz}^{-0.1}$ in the depth direction, however it is important to note that the thresholds will likely change due to a difference in crack morphologies. Also note that the work by Chen and Sutherby set the threshold for the growth of a sharp crack at $8500(\mathrm{MPa\,m^{0.5}})^3$ $\mathrm{Hz}^{-0.1}$ [40]. Taking the combined factors in the depth and at the surface of the specimens (from Table 3.10), all cracks met the threshold in the depth per Egbewande et al. [43]. However, only the 500 s CA specimen had a combined factor greater than the threshold specified by Egbewande et al. [43]. It is interesting to note that crack arrest was observed at the surface for the fully exposed and the fully coated cracks subjected to the 500 s ULH loading; however, the partially coated crack still showed crack growth despite being below the threshold per Egbewande et al. [43]. The observed growth at the surface may suggest that the absence of anodic dissolution at the crack tip was enough to keep the crack sufficiently sharp in the fully-coated specimen. Further, hydrogen appeared to enhance crack growth in the partially-coated specimen.

The key difference between the work by Egbewande et al. and the current study is that the specimens in the work by Egbewande et al. kept an EDM slot, thus allowing for a wider crack mouth and therefore more fluid mixing from the bulk solution [43]. Further, a greater combined depth from the notch in addition to the crack tip would give rise to a greater stress intensity factor at the crack tip. The difference in crack width will therefore affect the thresholds for discontinuous and continuous crack growth.

Some trends are readily observable by looking at the crack growth data for the partially-coated cracks. As would be expected, a higher combined factor led to increased crack growth in the depth direction, due to an increase in the mechanical driving force. However, an increase in combined factor at the surface led to a supposed *decrease* in crack growth rates. This behaviour suggests that loading waveform shape and the presence of a monotonic hold may be more significant at the surface where hydrogen is expected to be more plentiful [39, 119]. Further discussion of the mechanism for hydrogen trapping and plastic damage are noted in the following section.

4.3.3 Plastic Damage and Room-Temperature Creep

Observed crack growth at the surface for the 10 s ULH, 10 s CA, and 500 s CA waveforms as opposed to the 500 s ULH waveform may be related to reduced screw dislocation mobility [68], allowing for more irreversible slip processes to occur. Sidey and Coffin [74] noted that waveform shape had some effect on crack growth rates in copper at elevated temperature in inert fatigue and these results suggest that waveform shape may affect crack growth rates in steel at room temperatures.

Comparing the two constant amplitude loading schemes, the waveform with rapid unloading displayed more crack growth per cycle at the surface despite having a lower mechanical driving force. Similarly, the ULH waveform with rapid unloading displays more crack growth. Based on these findings, sufficiently rapid unloading may be able to effectively lock atomic hydrogen within the fracture process zone near the surface of the specimen. Higher amounts of plastic damage and the absence of the monotonic hold in the constant amplitude loading waveforms can explain the absence of crack tip blunting related to room-temperature creep processes. However, the 10 s ULH waveform would be expected to also undergo RTC, but changes to the screw dislocation mechanics [68] and maybe formation of persistent slip bands [70] may be sufficient to overcome effects of RTC. Few differences were observed in the fractography micrographs between the various waveforms. From the micrographs of the crack tips at the surface, the crack tip remained sharp in the 500 s ULH waveform, so crack tip blunting from RTC may not be significant in this case.

Plastic damage as a result of decreased screw dislocation mobility may act as another means of increasing irreversible plastic damage that acts as a trapping site for hydrogen, effectively increasing crack growth rates. However, crack growth enhancement due to the presence of increased hydrogen concentration may be counteracted by increased plasticity effects in the presence of hydrogen as well as acting as a source for stored plastic energy driving room-temperature creep.

4.3.4 Crack Chemistry Considerations

Comparing the extremes of unloading rates (500 s vs 10 s), with and without a 1-hour monotonic hold (ULH vs CA waveforms), the fracture surface morphologies of the

fully exposed cracks suggest an effect from advection of the fluid. Taking the work by Turnbull and Ferriss [61], a significant potential drop across the crack depth would not be expected in the current study due to the relatively shallow crack depths (< 1 mm) used. However, mixing with the bulk solution would be more pronounced with higher unloading rates, in addition to the relatively high contributions of diffusion and ion migration to mass transport [107]. Evidence of some level of liquid entrapment between the crack walls is observed from Figure 4.4, where a gradient of corrosion byproduct can be seen, with higher concentrations nearer to the crack tip. This gradient is most likely due to the initial pre-charging time, where no dynamic loading was applied an corrosion build-up would occur toward the crack tip as a result of a slight potential drop within the crack. Subsequent dynamic loading during testing would then be affected due to the prior corrosion build-up.

Taking the EDX results, it is speculated that the darkest deposits in SEM-BSE images is a Ca-rich hydroxide or oxide and that iron carbonates are formed along the crack walls and especially near the crack front due to limited diffusion. Incomplete cathodic protection noted in the work by King et al. [44] can explain the dissolution of the crack walls during the hydrogen pre-charging period prior to loading, from the crack depth profile in Figure 4.9.

4.3.5 Sources of Error

Although some trends were observed, there are inherent variations during testing that will affect the results. Residual stress profiles from machining will vary (although milling was controlled as carefully as possible). Another source of variation would be the measurement error during microscopy. Replication damage could also have occurred during the replication process, as well as during SEM imaging from the electron beam. There may also be some variations in the tensile strength of the specimens, although these errors were mitigated by taking the samples from the same cut of pipe. Crack closure effects from the coatings are considered negligible in this study due to the narrow crack mouth opening as well as the relatively low crack depths. Further, there is also potential for measurement error, due to relatively low total crack growth both in the depth and at the surface.

Due to the small crack sizes and stress intensity factors being near threshold, there is a potential for a significant amount of the fracture process zone undergoing plastic deformation. Akid defines the transition between EPFM and LEFM to be approximately $a/r_p = 50$ [20], and current crack depths relative to the plastic zone size do not exceed this ratio. However, we can conclude that the cracks are nominally in LEFM from the thin-walled crack morphologies in the cross-section micrographs.

4.3.6 Future Work

Further testing for statistical validation is recommended to further explore this phenomenon. Further, testing on other grades of steel and various ranges of $K_{\max}$, ΔK, holding times, and waveform shapes are recommended to further demarcate potential changes in crack behaviour with the addition of a monotonic hold.

4.3.7 Impacts on Pipeline Integrity Management

With the above information, pipeline operators can optimize their hydrostatic test programs to minimize the amount of potential crack growth during operations and fitness-for-service testing. Following the work by Yu et al. [64], a static hold at maximum operating pressure can retard subsequent crack growth, especially following a significant

depressurization-repressurization event. The main addition from the current study is corroborating the findings from Yu et al. [64] with the surface crack geometries, expanding on the findings from Egbewande et al. [43], and differentiating the relative contributions from inert fatigue and hydrogen enhanced fatigue under cathodic protection.

4.4 Summary

The work in this chapter compared the crack growth behaviour of fully-coated, partially-coated, and fully-exposed semi-elliptical cracks immersed in a near-neutral pH environment with an applied cathodic potential. The effect of adding a one-hour monotonic hold was explored. The addition of a one-hour hold was shown to cause crack arrest at the surface of the cracks for fully-coated specimen due to room-temperature creep. Similarly, crack arrest was observed in the fully-exposed specimen likely due to a combination of room-temperature creep, anodic dissolution, and hydrogen-enhanced localized plasticity. Rapid unloading was found to enhance crack growth, suggesting that waveform shape can significantly affect crack growth behaviour during variable amplitude loading in corrosion fatigue due to enhanced hydrogen segregation. Further, enhanced crack growth from increased hydrogen concentrations at the crack tip due to crack morphology, reduced screw dislocation mobility, and applied cathodic potentials may be able to overcome retardation effects expected from an applied static hold.

Chapter 5

Effect of Unloading Rate

5.1 Overview

In this chapter, the effects of unloading rate on crack growth for a triangular loading waveform with intermittent monotonic holds will be studied. Crack growth rates as a function of the unloading rate, combined factor, fractography micrographs, energy-dispersive x-ray spectroscopy (EDX), and crack morphologies will be used to compare crack behaviour in a simulated inert environment (fully coated), near-neutral pH dilute bicarbonate solution (fully exposed), and a thinly coated specimen to simulate a hydrogen-rich environment with no anodic dissolution. Tabulated data corresponding to the graphs can be found in Appendix A and additional micrographs can be found in Appendix B.

5.2 Results

5.2.1 Crack Growth Rates vs Unloading Rate

The crack growth rate in the depth (da/dN) and at the surface (dc/dN) were plotted with respect to the unloading rates at their respective locations (dK/dt) in order to account for varying crack geometries, as seen in Figure 5.1.

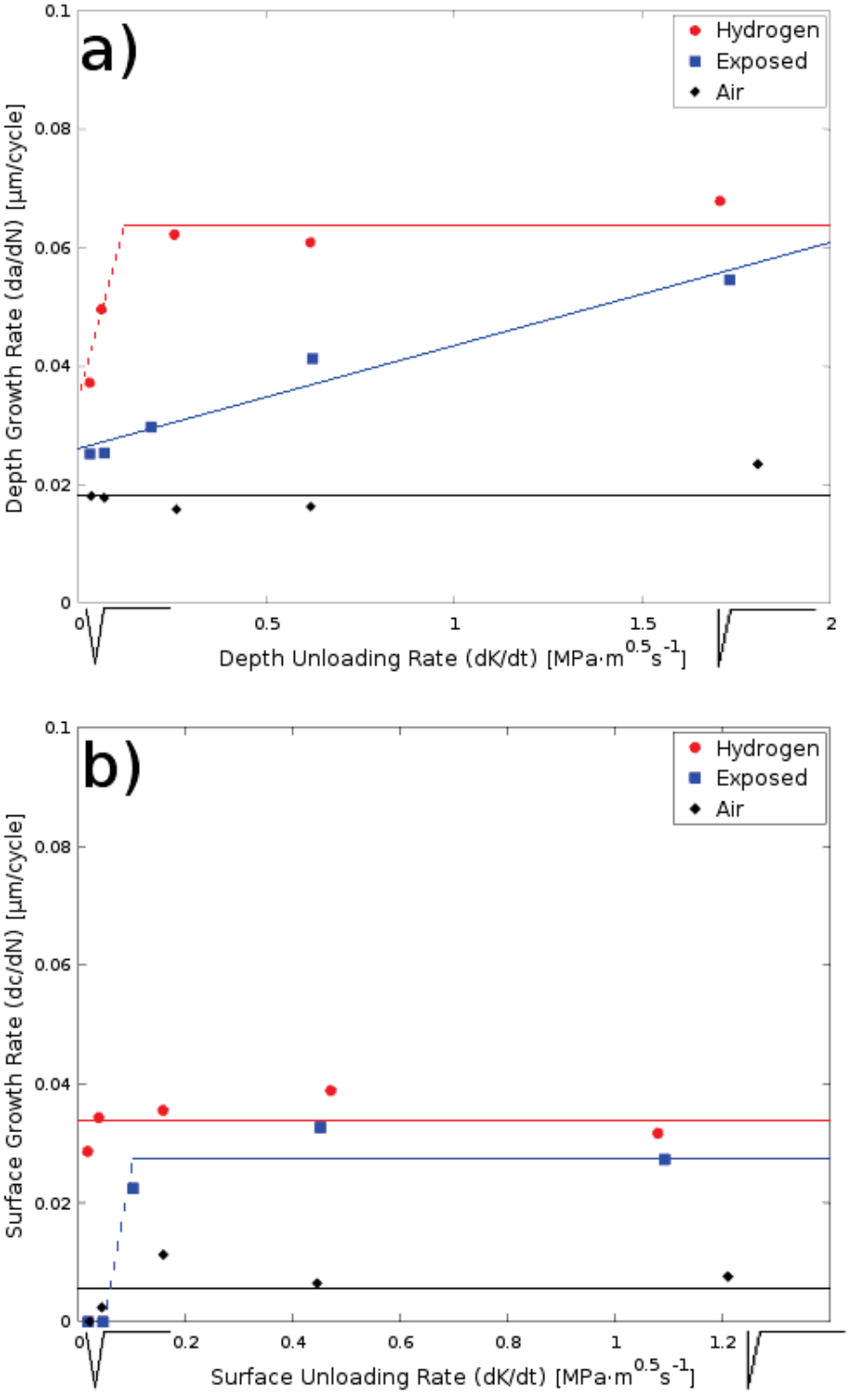

Figure 5.1: Growth per cycle as a function of unloading rate a) in the depth and b) at the surface.

Focusing on the depth growth rates, the "Air" cracks had a negligible dependence on unloading rate with an average growth rate of 0.018 ± 0.003 µm/cycle. However, the

"Exposed" cracks suggested a linear dependence of da/dN on dK/dt in the depth. Finally, the "Hydrogen" cracks appear to increase growth rates significantly until a dK/dt of approximately $0.25\,\mathrm{MPa\,m^{0.5}\,s^{-1}}$ to a mean value of 0.064 ± 0.004 µm/cycle. The error was determined by taking the standard deviation of the crack growth rates per cycle from each test.

From the surface growth rates, there appears to be minimal dependence on the unloading rate. However, it is important to note that there was no crack growth at the surface for the symmetrical underload and hold loading spectrum for the "Air" and "Exposed" cracks but crack growth was observed for the "Hydrogen" crack. Furthermore, increasing the unloading rate allowed for crack growth at the surface for both the "Air" and "Exposed" environments. The mean crack growth rates are summarized in Table 5.1.

Table 5.1: Average crack growth rates at the surface for the three simulated environments. *Taken only for unloading times less than 60 s.

Environment	**Depth**	**Surface**
Hydrogen	0.064 ± 0.004*	0.034 ± 0.004
Exposed	N/A	0.027 ± 0.005*
Air	0.018 ± 0.003	0.006 ± 0.004

Generally, the "Hydrogen" cracks had greater growth than the "Exposed" cracks, followed by the "Air" cracks. Furthermore, the growth per cycle in the depth was generally greater for all cracks when compared with growth at the surface. Figure 5.2 outlines the relationship between the aspect ratio of growth and the unloading rate.

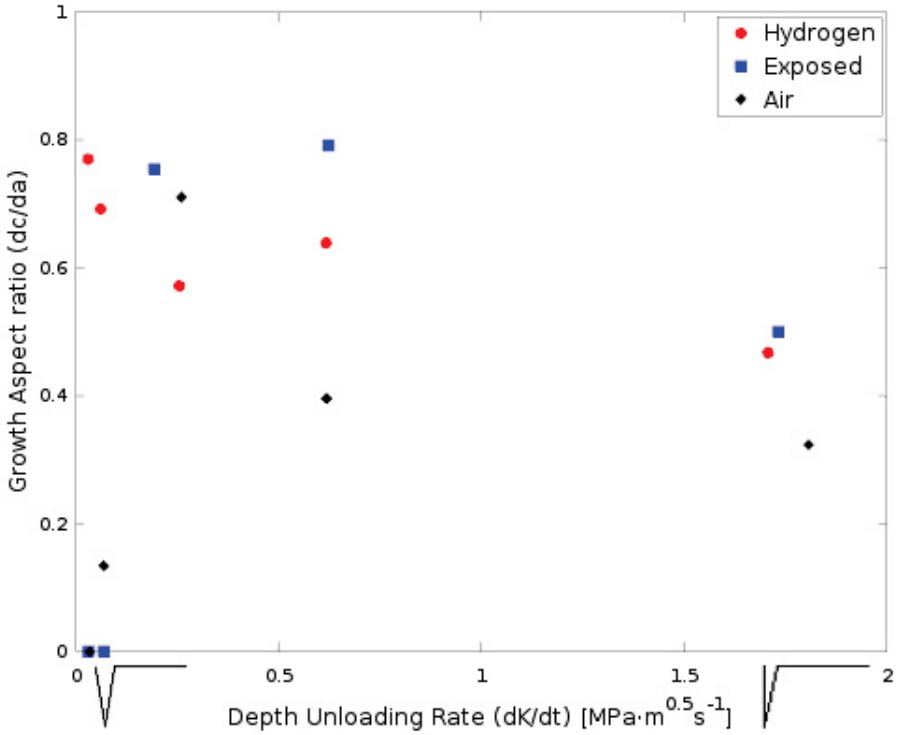

Figure 5.2: Aspect ratio of growth as a function of unloading rate at the depth.

An aspect ratio of growth $dc/da = 1$ would indicate equal crack growth at the surface and depth. Similarly, $dc/da > 1$ indicates more growth at the surface and $dc/da < 1$ would indicate more growth in the depth. From Figure 5.2, the "Air" cracks generally had more depth in the growth with a mean of 0.31 ± 0.27, with a significant standard deviation when compared with the mean value. However, both the "Exposed" and "Hydrogen" cracks displayed a decrease in growth aspect ratio as dK/dt increased, indicating more aggressive growth in the depth at higher unloading rates.

5.2.2 Crack Growth Rates vs Combined Factor

The crack growth rates in the surface and depth are plotted with respect to the combined factor for each of the three environments, shown in Figure 5.3. Note that the combined factors for all tests loaded to an underload and static hold were relatively similar in the air environment and thus the crack growth rates in the depth were also of similar value. However, more scatter was observed at the surface. In particular, the growth at the surface for the 60 s unloading time is much higher, especially comparing to the crack dormancy observed at 500 s unloading with a higher combined factor.

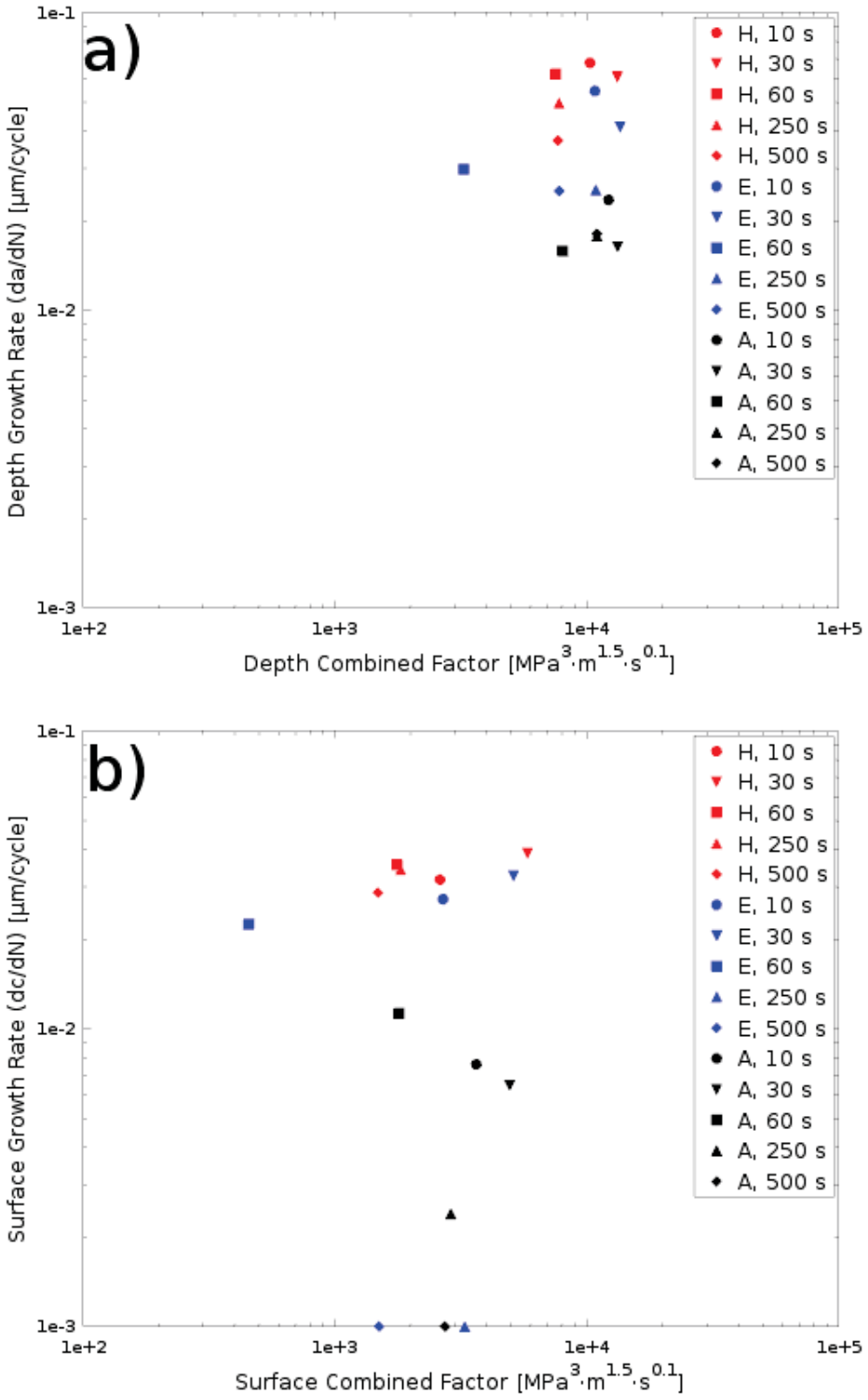

Figure 5.3: Growth per cycle as a function of combined factor a) in the depth and b) at the surface for the "Hydrogen", "Exposed", and "Air" environments. Note that all features plotted were tested with the ULH type waveform at various unloading times.

In the fully exposed cracks, we can see that although different samples may have similar combined factors, da/dN increases with decreasing unloading time. Furthermore, the

60 s unloading has comparable da/dN with the 500 s unloading despite having a lower combined factor. At the surface, samples with an unloading time of 60 s and less all displayed growth while samples with an unloading time of 250 s and 500 s displayed crack dormancy.

In the partially coated cracks, all cracks had comparable combined factors yet da/dN increased as unloading time decreased. It is interesting to note that the cracks with an unloading time of 60 s and less all had similar da/dN. Similarly, all cracks had similar dc/dN despite having a factor of 10 difference in combined factor. The general trend is that the "Hydrogen" environment has the greatest crack growth rates, followed by the "Exposed" environment and finally the "Air" environment.

5.2.3 Fractographic Images

Figures 5.4 and 5.10 show typical low magnification SEM-BSE micrographs of the fracture surfaces corresponding to the "Air" and "Hydrogen" environments. All images were shown for the fracture surface corresponding to the "Exposed" environments (Figures 5.5 to 5.9) due to significant variations between the various loading conditions. This section will outline the features observed in each environment.

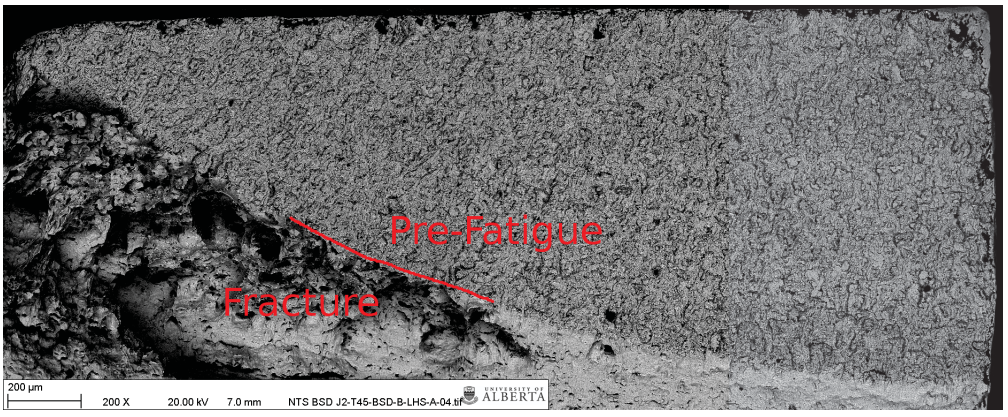

Figure 5.4: SEM-BSE micrograph of "Air" fracture surface loaded with 10 s unloading, 500 s ramp, and 1 h static hold.

From Figure 5.4, no significant changes were observed between the pre-fatigue crack growth region and the growth region from testing in the "Air" environment, as expected. However, the boundary between fatigue crack growth and post-test fracture is observable. In this case, some plastic deformation was observed near the depth due to the sample geometry prior to post-test fracture.

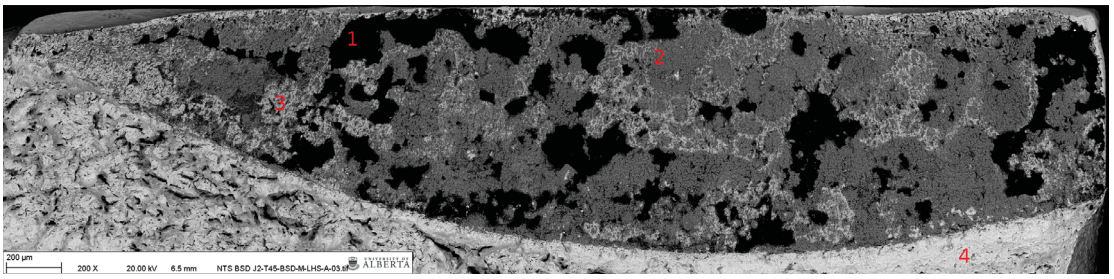

Figure 5.5: SEM-BSE micrograph of "Exposed" fracture surface loaded with 10 s unloading, 500 s ramp, and 1 h static hold.

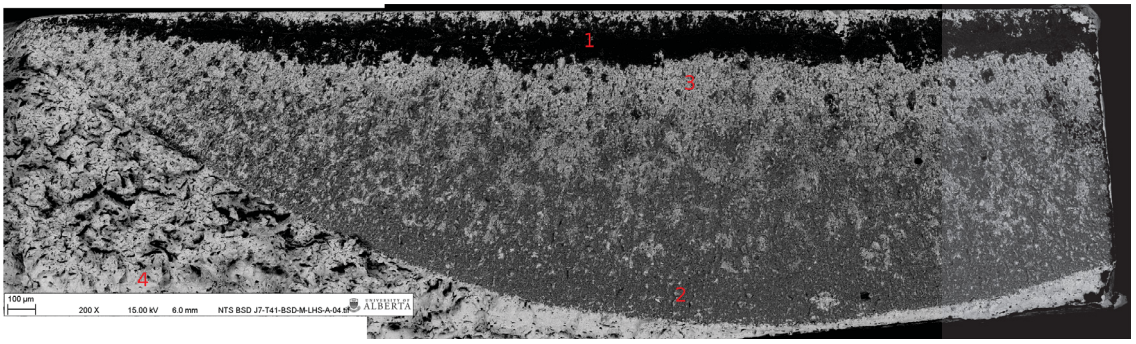

Figure 5.6: SEM-BSE micrograph of "Exposed" fracture surface loaded with 500 s constant amplitude loading; subsequent testing with 30 s unloading, 500 s ramp, and 1 h static hold was performed.

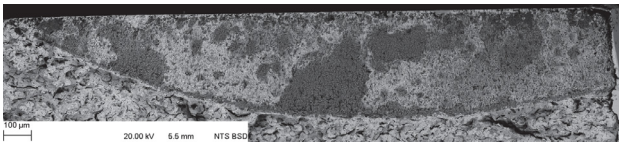

Figure 5.7: SEM-BSE micrograph of "Exposed" fracture surface loaded with 60 s unloading, 500 s ramp, and 1 h static hold.

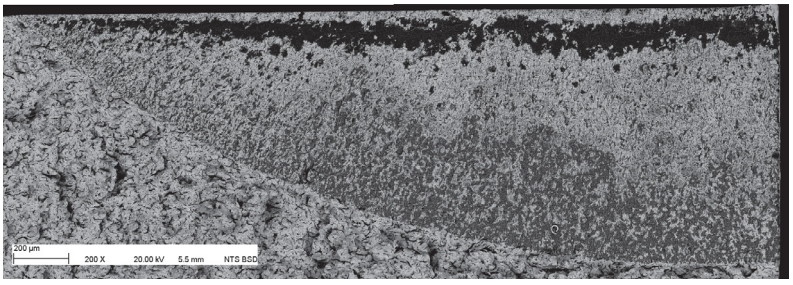

Figure 5.8: SEM-BSE micrograph of "Exposed" fracture surface loaded with 250 s unloading, 500 s ramp, and 1 h static hold.

For the fully exposed cracks shown in Figures 5.5 to 5.9, the boundary between the pre-fatigue crack growth and growth due to testing is easily observed at this magnification. Furthermore, the boundary between the growth region from testing and post-test fracture is also observable. Features of the fracture surfaces from the fully exposed cracks

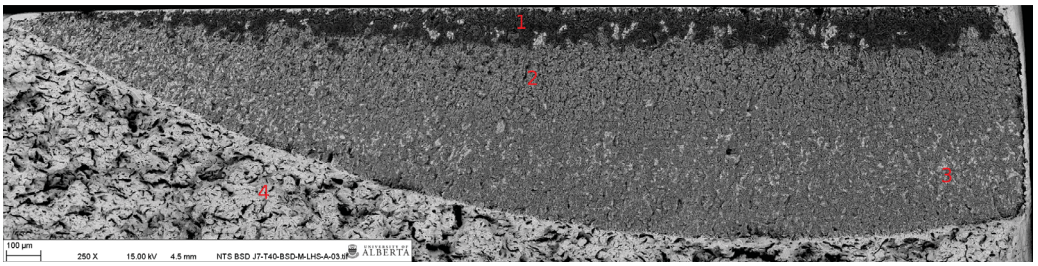

Figure 5.9: SEM-BSE micrograph of "Exposed" fracture surface loaded with 10 s unloading and 500 s constant amplitude loading; subsequent testing with 500 s unloading, 500 s ramp, and 1 h static hold was performed.

are summarized in Table 5.2.

Table 5.2: Observations of low magnification SEM-BSE micrographs of fully exposed crack surfaces. *Tested after prior constant amplitude loading and a second round of hydrogen-precharging.

Figure	Unloading Time	Observations
1	10 s	Darker corrosion product distributed throughout depth of crack. Regions of lighter corrosion product.
2	30 s*	Darker corrosion product only near the top of the crack. Lighter corrosion product mostly in the depth with a lighter gradient upward.
3	60 s	Lighter corrosion product distributed throughout depth. Much smaller in dimensions than other cracks.
4	250 s	Darker corrosion product only near the top. Lighter corrosion product visible nearer to the crack wall.
5	500 s*	Darker corrosion product only near the top. Lighter corrosion product covering rest of fracture surface.

For the partially coated cracks (example shown in Figure 5.10), a distinct growth band was observed due to a significant change in surface topography between the pre-fatigue crack growth region, testing region, and post-test fracture.

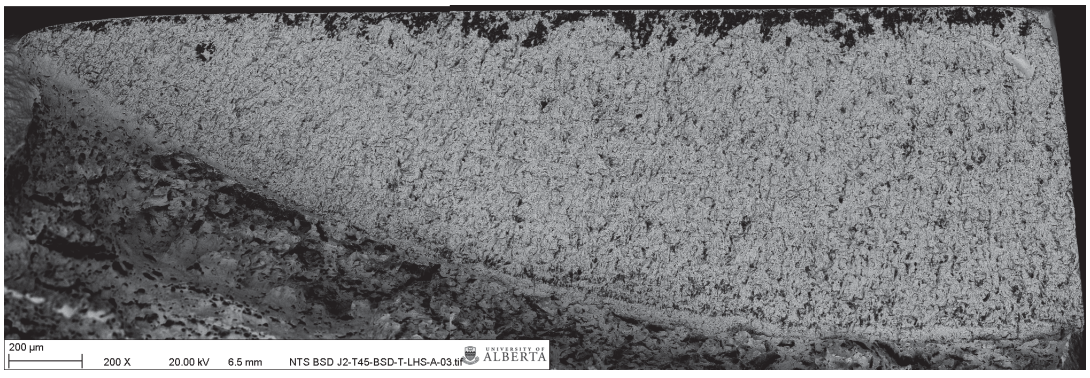

Figure 5.10: SEM-BSE micrograph of "Hydrogen" fracture surface loaded with 10 s unloading, 500 s ramp, and 1 h static hold.

Figures 5.11 to 5.13 show typical medium magnification SEM-SE micrographs of the fracture surfaces corresponding to the "Air", "Exposed", and "Hydrogen" environments. The remainder of the fracture surface micrographs are shown in Appendix B. This section will outline the various microscopic features used as criteria to determine where the growth zones end and begin.

Because the pre-fatigue crack growth was performed in air, growth in the "Air" environment is expected to have similar features, as seen in Figure 5.11. Significant changes in the surface topography or sudden changes in the step patterns of growth were used as a reference to separate pre-fatigue crack growth and crack growth from testing in the simulated "Air" environment.

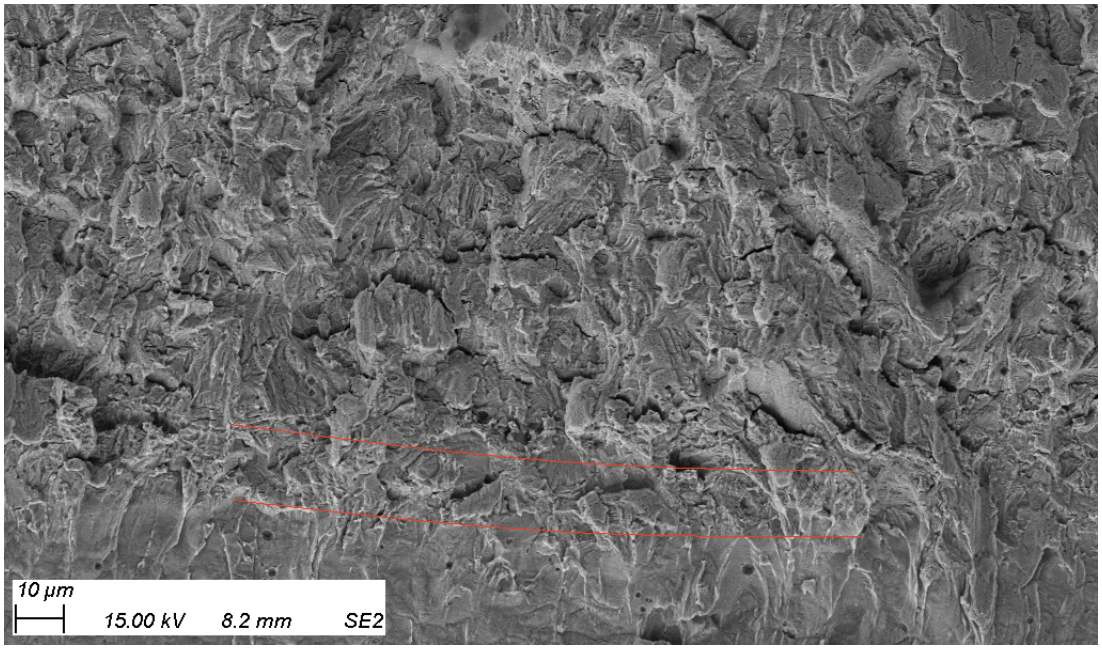

Figure 5.11: SEM-SE micrograph of "Air" crack growth band at the depth loaded with 10 s unloading, 500 s ramp, and 1 h static hold. Red lines indicate growth. Micrograph was taken after oxide removal.

After the minimum 12 day hydrogen pre-charging and at least 21 days of loading in the underload and hold spectra, corrosion product was observed in all "Exposed" cracks, as shown in Figure 5.12. Thus, the boundary between the pre-fatigue crack growth region and growth region from testing was relatively clear. Little corrosion product was observed in the growth region due to the relatively short period of exposure.

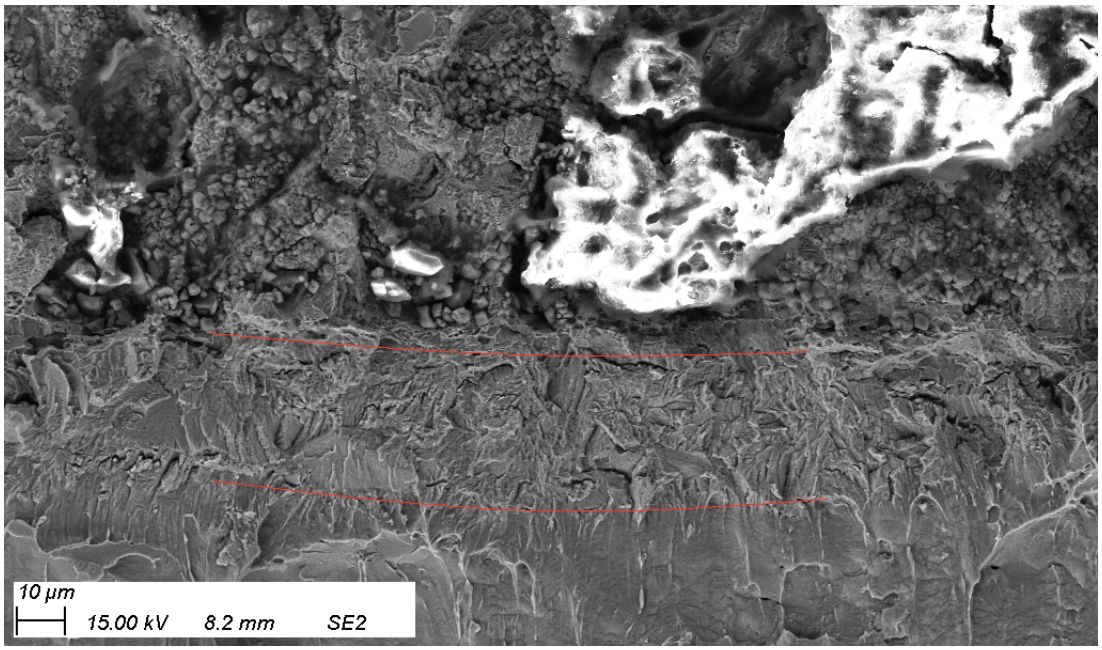

Figure 5.12: SEM-SE micrograph of "Exposed" crack growth band at the depth loaded with 10 s unloading, 500 s ramp, and 1 h static hold. Red lines indicate growth. Micrograph was taken after oxide removal.

Because the "Hydrogen" cracks (example shown in Figure 5.13) were isolated from direct exposure from C2 solution, little phase contrast was detected between the pre-fatigue crack region and growth zone. However, flat features were observed and the onset of larger faceted areas (prior to the post-test fracture zone) was used to define the beginning of the growth zone from testing.

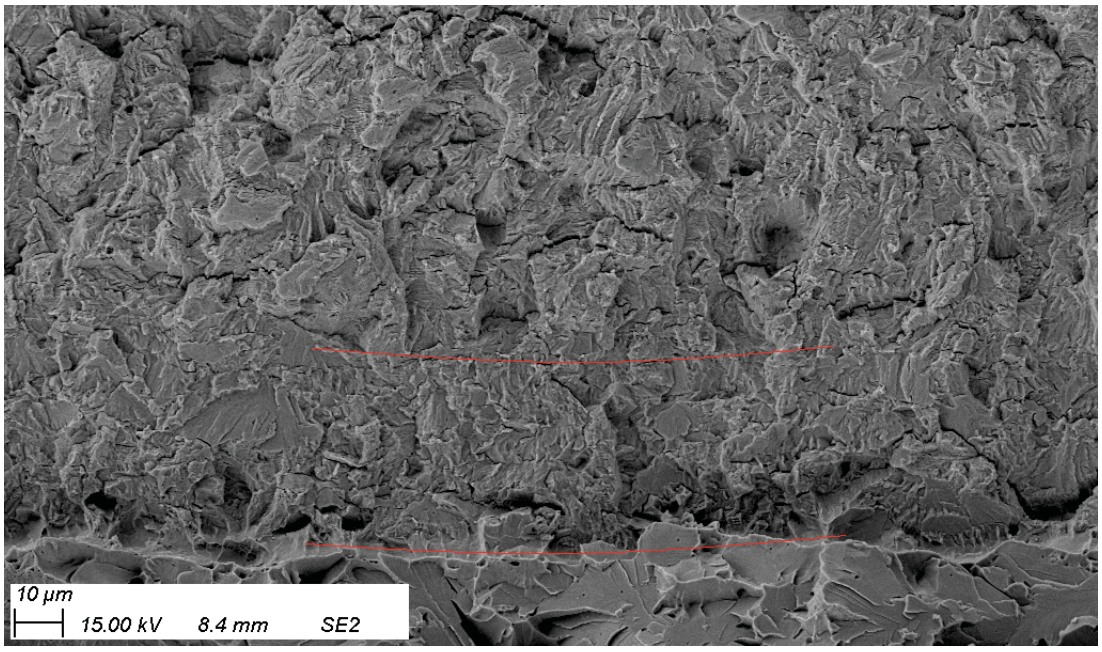

Figure 5.13: SEM-SE micrograph of "Hydrogen" crack growth band at the depth loaded with 10 s unloading, 500 s ramp, and 1 h static hold. Red lines indicate growth. Micrograph was taken after oxide removal.

5.2.4 Through-Thickness Crack Morphology

Figure 5.14 shows the depth profiles for all of the cracks, categorized by unloading rate and simulated environment. Generally, the crack tips in the depth remained sharp for all tests and environments. Figure 5.15 shows the depth profiles for the fully exposed cracks. Some crack widening was observed in the fully exposed environment, and significant widening was observed for the 10 s unloading time. Areas that have undergone pre-charging show a wider region for the fully exposed cracks, and growth regions were much thinner. Some crack tip branching and bifurcation was seen for all cracks.

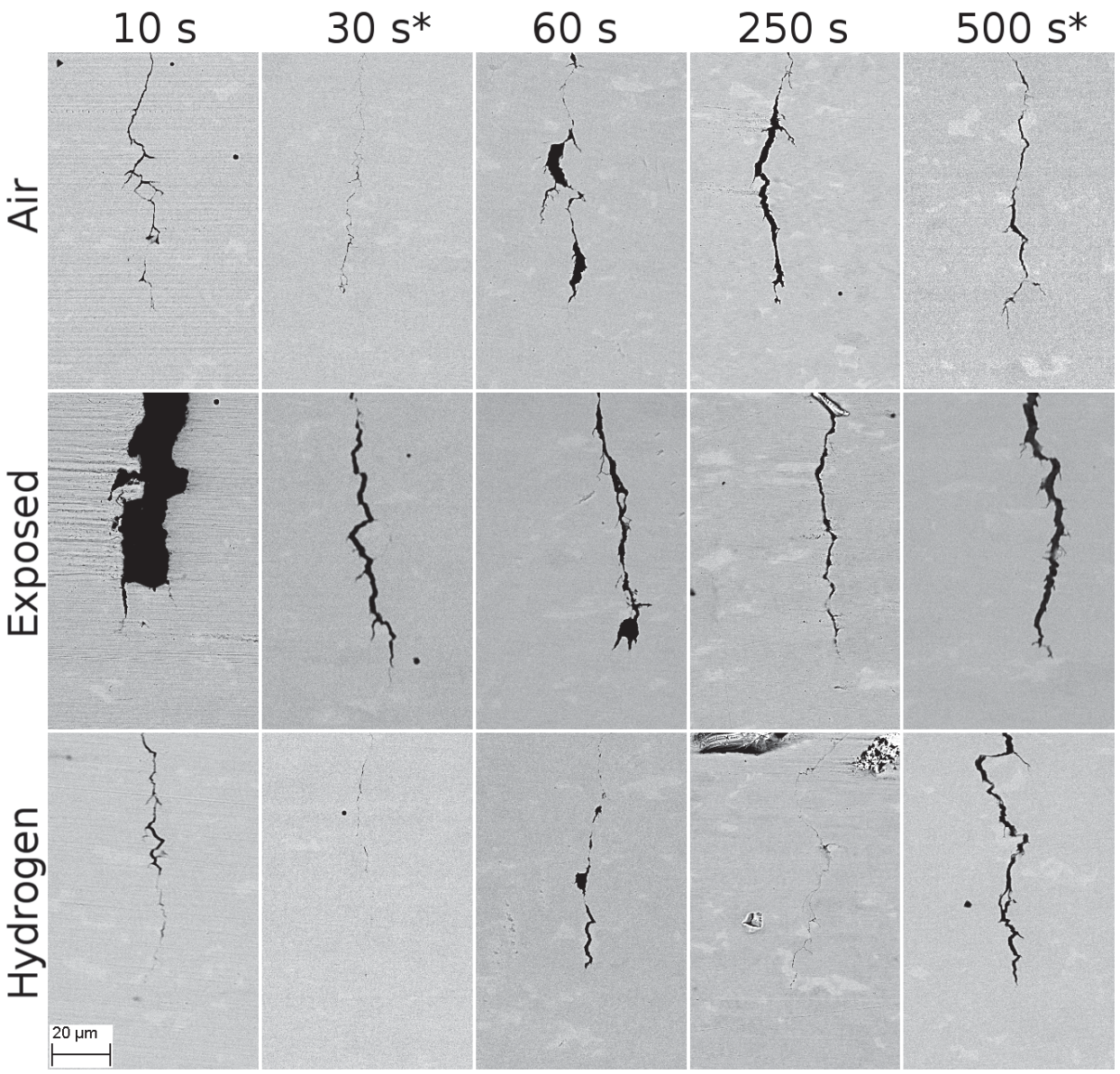

Figure 5.14: SEM-BSE micrographs of depth profiles, categorized by unloading times and simulated environment. The working distances ranged from 7.0 to 11.5 mm. The accelerating voltage used was 20 kV. Note that these depth profiles were not taken at the midpoint of the crack. *Previously loaded with a constant amplitude waveform.

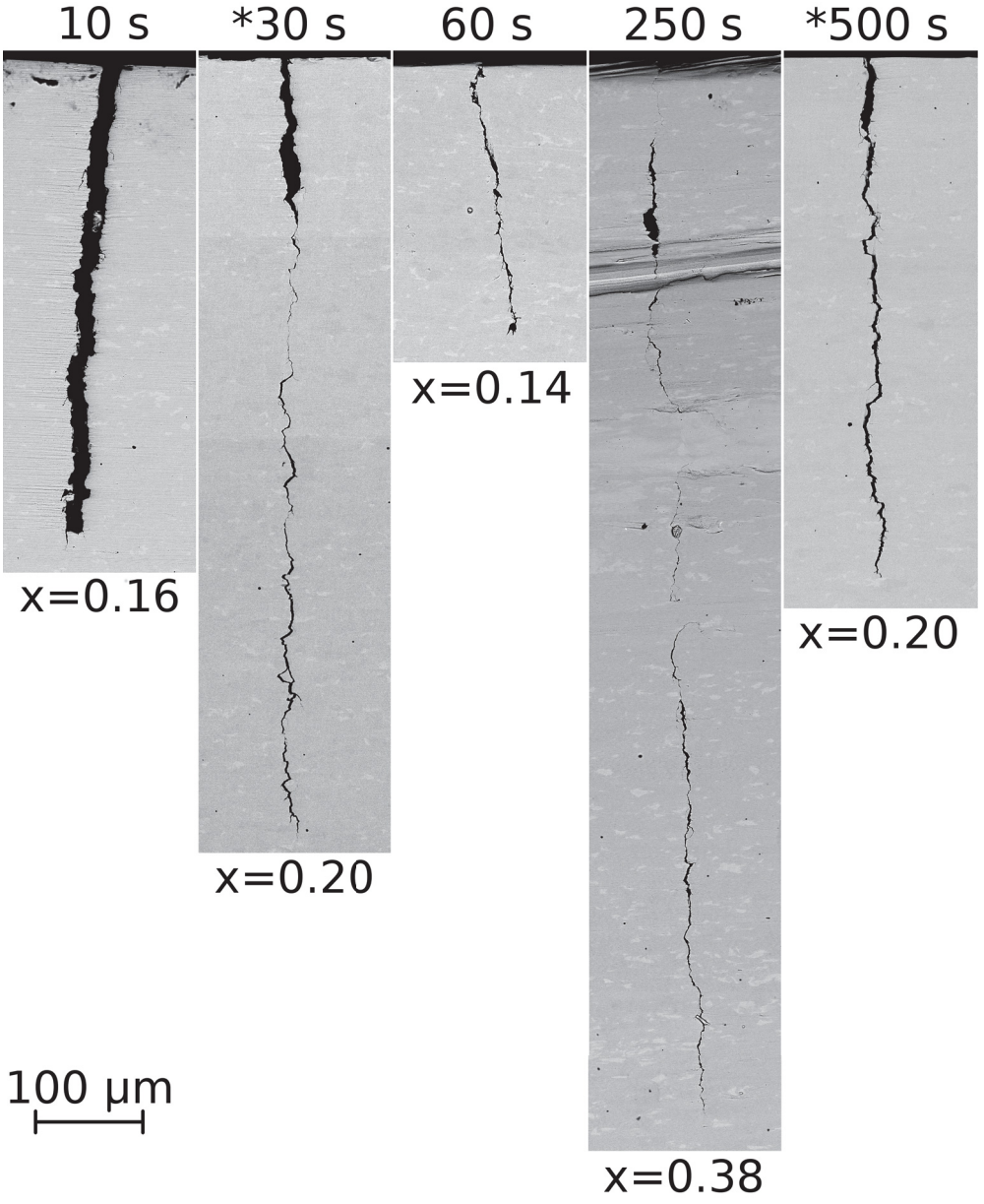

Figure 5.15: SEM-BSE micrographs of fully exposed crack depth profiles. The unloading times corresponding to underload and hold waveforms are shown and the approximate length fraction x is indicated beside the corresponding images. Images were taken with an acceleration voltage of 20 kV and working distances were between 7.5 mm and 10.5 mm. *Denotes prior constant amplitude loading.

5.2.5 Crack Morphology at the Surface

Figure 5.16 shows the surface profiles for all of the cracks, categorized by unloading rate and simulated environment. Generally, the crack tips at the surface remained sharp for all tests and environments. Some crack widening was observed in the fully exposed

environment, and significant widening was observed for the 10 s unloading time. Areas that have undergone pre-charging show a wider region for the fully exposed cracks, and growth regions were much thinner.

Furthermore, the crack tip for the fully exposed crack subjected to 500 s unloading times displayed blunting. Although the crack tips for the "Air" crack with an unloading time of 500 s and the "Exposed" crack with an unloading time of 250 s remained sharp, no significant crack growth was observed at the surface.

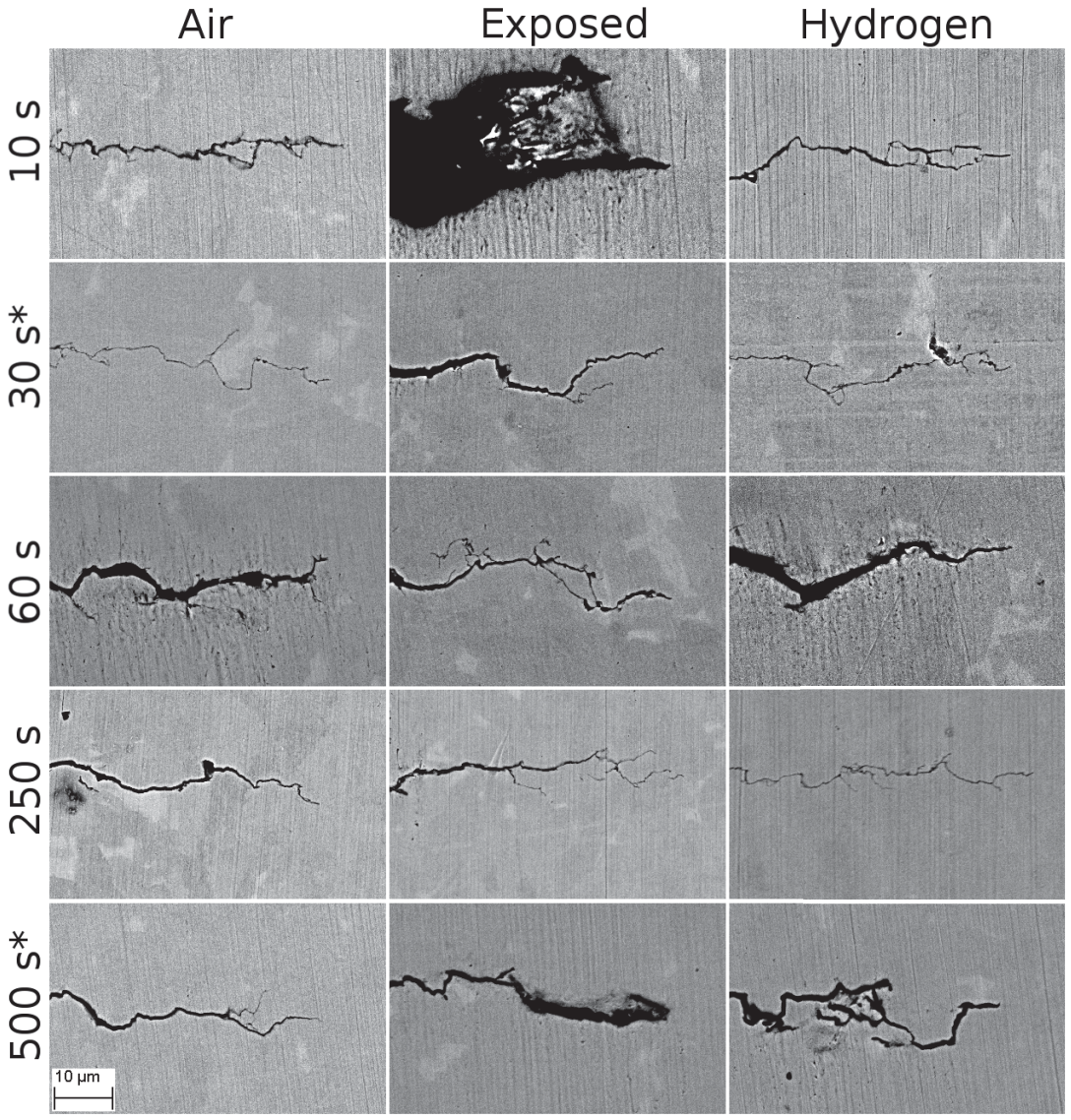

Figure 5.16: SEM-BSE micrographs of surface profiles, categorized by unloading times and simulated environment. The working distances ranged from 7.0 to 12.0 mm. The accelerating voltage used was 20 kV. *Previously loaded with a constant amplitude waveform.

5.2.6 Microscopic Features

Direct observation of striation widths were statistically insignificant due to variations in viewing angles. Furthermore, due to the relatively low stress intensity at the crack tip, several loading cycles were expected to generate a single striation, adding more variation in da/dN correlations. Note the relative "waviness" in the striations, indicating the presence of multiple active slip systems. The activation of multiple slip systems may be signs of sufficient levels of hydrogen within the fracture process zone to aid in dislocation slip of secondary slip systems. Typical images of striations found in each environment are shown in Figure 5.17.

Protrusions and cavities were only observed in the "Exposed" and "Hydrogen" cracks. Typical images are shown in Figure 5.18 Microvoids were also observed near protrusions and cavities within the fracture process zone, some distance ahead of the crack wall. Some charging was observed in the SEM fractographs, indicating non-conductive scale formation as seen in Figure 5.19. Formation of these carbonates and hydroxides may be related to the relatively short diffusion distance and advection effects as a consequence of the relatively shallow cracks (less than 1 mm). Furthermore, non-metallic inclusions were also observed from the FESEM micrographs, as seen in Figure 5.20.

5.2.7 Chemical Composition

Table 5.3 shows the semi-quantitative EDX results for the various regions, with the balance composed of C and trace amounts of Si. The dark film near the surface of the samples showed high amounts of carbon, calcium, and oxygen (other than iron). This may be related to a formation of carbonate. The darker regions toward the crack depth also showed the presence of carbon, calcium, and oxygen. This region may be related to the formation of a carbonate mixed with oxides. Finally, lighter regions on the crack walls showed mostly oxygen.

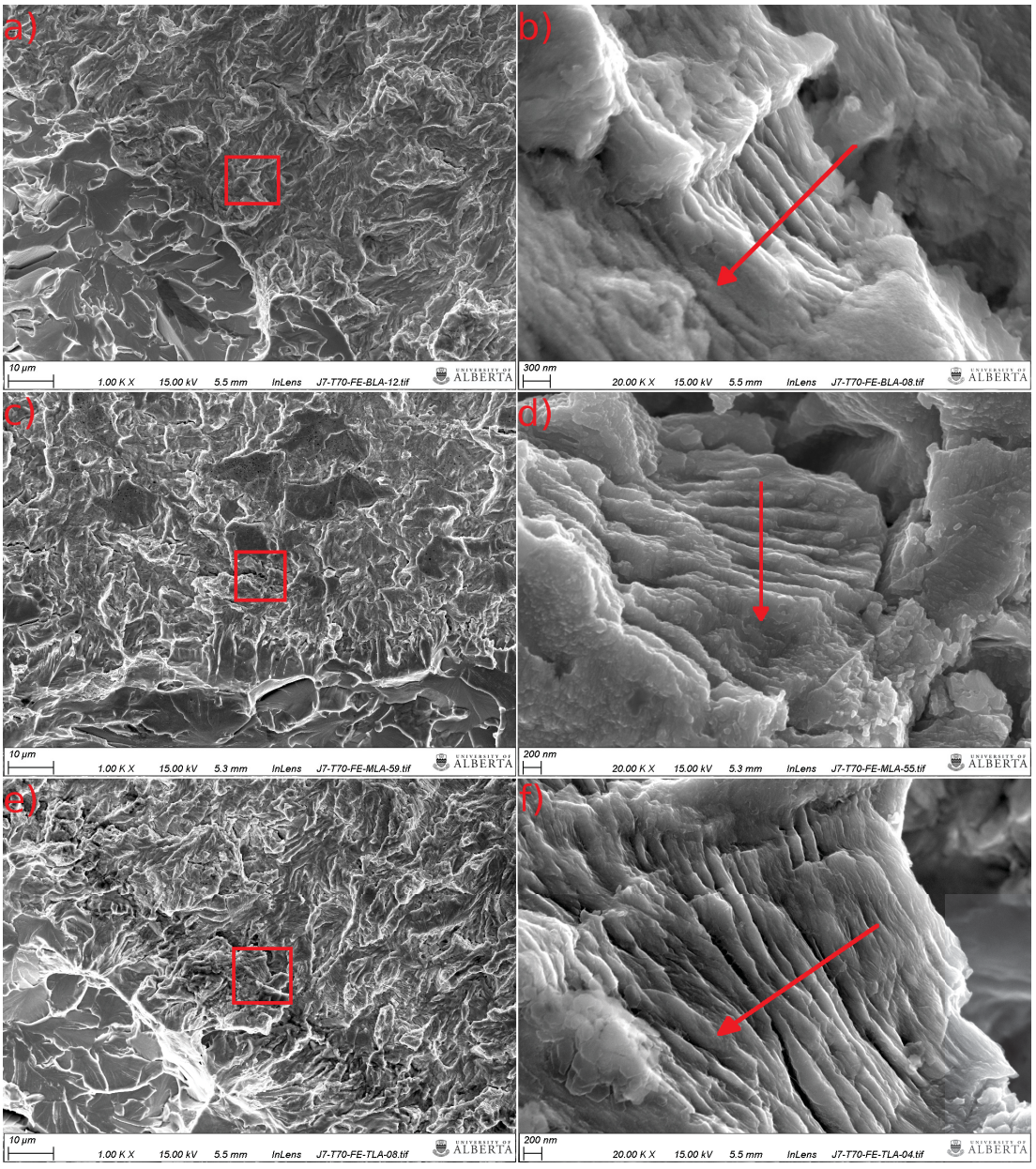

Figure 5.17: FESEM SE micrographs using the in-lens detector of typical striations from samples exposed to (a-b) "Air", (c-d) "Exposed", and (e-f) "Hydrogen" environments for 10 s unloading and 500 s constant amplitude loading and subsequent 500 s unloading, 500 s loading, and 1 hour hold. Images were taken with an acceleration voltage of 15 kV and working distances were between 5.3 mm and 5.5 mm. Red boxes in the left column denote the corresponding location for the higher magnification images in the right column. Arrows indicate the direction of crack propagation. Micrographs were taken after oxide removal.

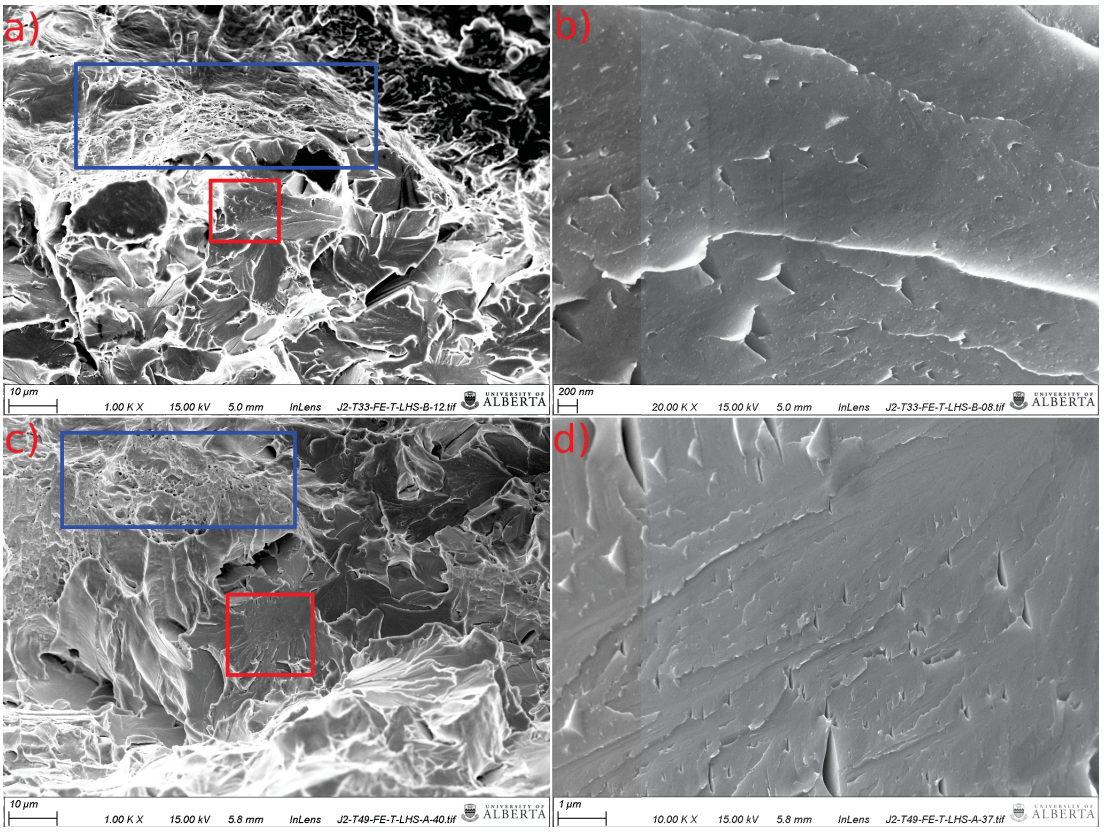

Figure 5.18: FESEM SE micrographs using the in-lens detector of protrusions and cavities found on samples exposed to (a-b) "Exposed", and (c-d) "Hydrogen" environments for 10 s unloading, 500 s loading, and 1 hour hold. Images were taken with an acceleration voltage of 15 kV and working distances were between 5.0 mm and 5.8 mm. Red boxes in the left column denote the corresponding location for the higher magnification images in the right column. Blue boxes indicate regions of clustered microvoids. A series of protrusions are shown in (b) while cavities are shown in (d).

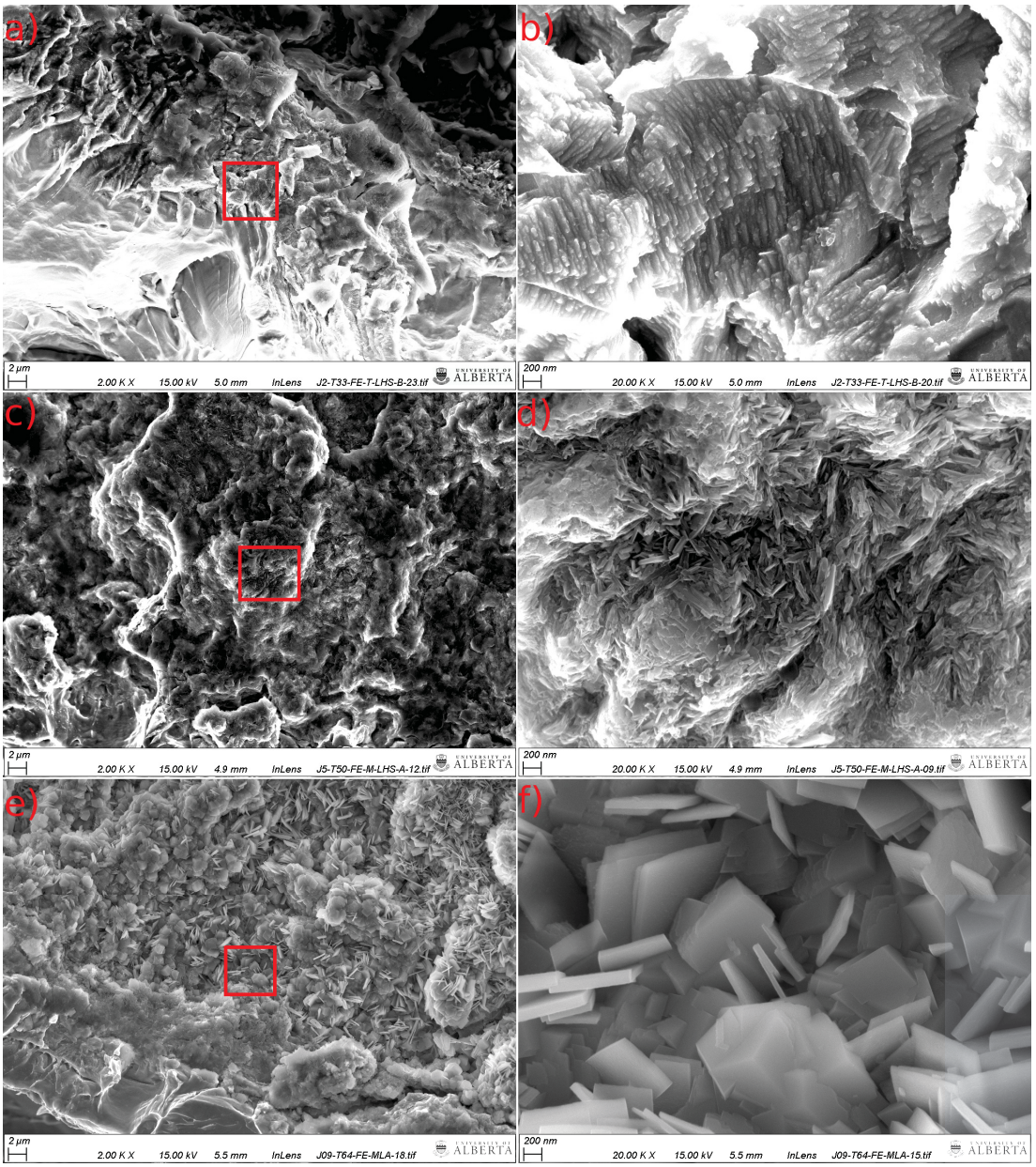

Figure 5.19: FESEM SE micrographs using the in-lens detector of various precipitates found on fully exposed cracks loaded with (a-b) 10 s unloading, 500 s loading, and 1 hour hold; (c-d) 10 s unloading with 500 s constant amplitude loading, with subsequent 500 s unloading, 500 s loading, and 1 hour static hold; and (e-f) 30 s unloading, 500 s loading, and 1 hour hold. Images were taken with an acceleration voltage of 15 kV and working distances were between 4.9 mm and 5.5 mm. Red boxes in the left column denote the corresponding location for the higher magnification images in the right column.

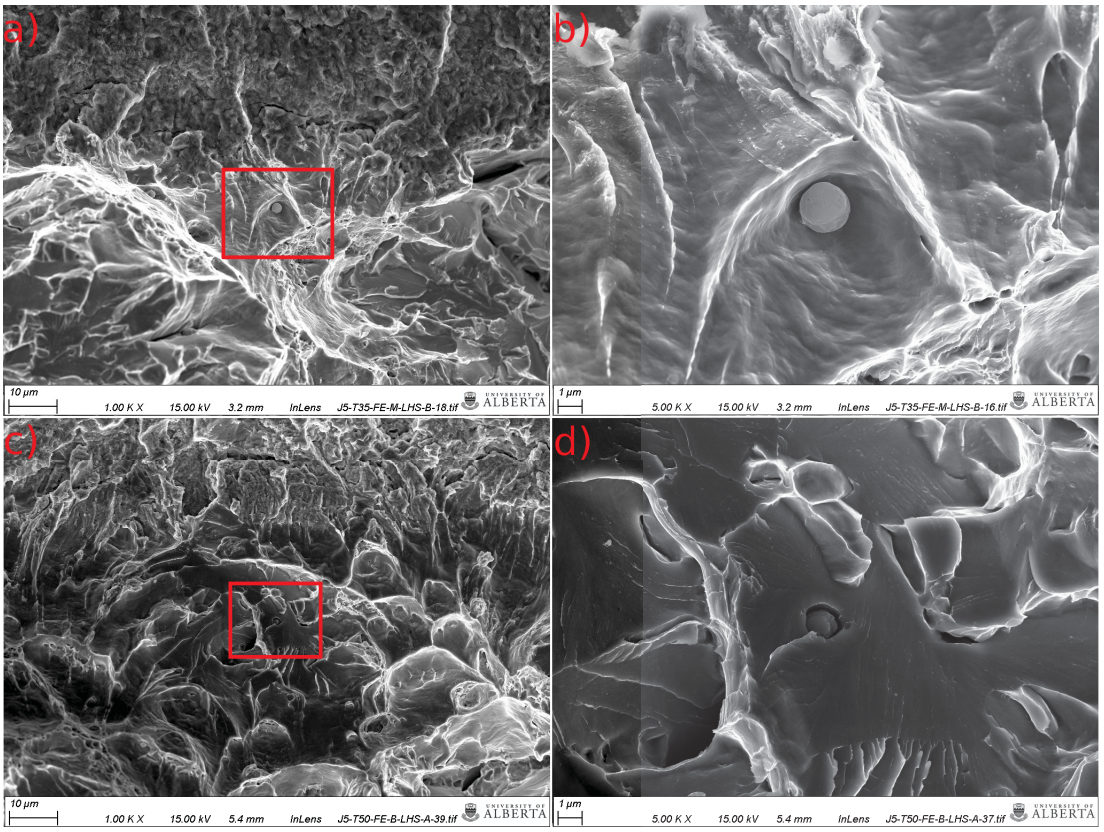

Figure 5.20: FESEM SE micrographs using the in-lens detector of inclusions from (a-b) "Air" and (c-d) "Exposed" cracks loaded with 10 s unloading with 500 s constant amplitude loading, with subsequent 500 s unloading, 500 s loading, and 1 hour static hold. Images were taken with an acceleration voltage of 15 kV and working distances were between 3.2 mm and 5.4 mm. Red boxes in the left column denote the corresponding location for the higher magnification images in the right column.

Table 5.3: EDX results in wt.% for fully exposed cracks. Balance of composition is C. Relevant loading conditions are shown below.

Feature / Location	Loading Conditions	Fe	Mn	Ca	O
Darkest, Top Surface	10 s ULH	1.7	-	-	16.3
	500 s CA; 30 s ULH	19.2	-	42.7	28.2
	250 s ULH	0.6	-	28.5	54.2
	10 s CA; 500 s ULH	9.4	-	65.3	17.6
Darker, Crack Surface	10 s ULH	90.9	-	0.7	2.7
	500 s CA; 30 s ULH	58.9	-	0.4	35.1
	60 s ULH	69.3	1.7	0.6	23.9
	250 s ULH	86.1	-	-	11.5
	10 s CA; 500 s ULH	73.5	-	19.0	-
Lighter, Crack Surface	10 s ULH	73.8	-	0.9	17.1
	500 s CA; 30 s ULH	87.9	-	-	7.1
	60 s ULH	92.8	-	-	5.0
	250 s ULH	79.4	1.8	-	13.8
	10 s CA; 500 s ULH	80.5	-	16.0	-
Cleavage	10 s ULH	97.1	2.2	-	-
	500 s CA; 30 s ULH	96.6	2.4	-	-
	60 s ULH	96.8	2.4	-	-
	250 s ULH	96.4	-	-	-
	10 s CA; 500 s ULH	94.7	-	-	-

5.2.8 Summary of Results

Table 5.4 summarizes the key results that have been shown thus far. The next section will explain the results shown here and will link trends to literature. Generally, the "Hydrogen" environments showed the greatest crack growth rates, followed by the "Exposed" and "Air" environments.

Table 5.4: Key observations from the various analyses performed.

Analysis	**Key Observations**
Unloading Rate	More of an effect in the depth, negligible effects at the surface and for "Air" cracks. Depth CGR increases linearly for "Exposed" cracks. Rapid depth CGR increase for "Hydrogen" cracks with $dK/dt > 0.25$. Consequently, crack growth is favored in the depth over the surface for "Exposed" and "Hydrogen" cracks at greater unloading rates.
Combined Factor	Greater crack growth rates are observed in the depth for "Exposed" cracks with comparable combined factors. Higher unloading rates can overcome crack dormancy for cracks with comparable combined factors.
Fractography	Two types of corrosion products were observed for "Exposed" cracks, one closer to the surface and one closer to the depth. The distribution of corrosion product appeared to change with unloading times. "Hydrogen" cracks showed larger faceted surfaces.
Depth Profiles	All crack tips remained sharp. Some widening during precharging in the "Exposed" cracks.
Surface Profiles	Most crack tips remained sharp. No growth observed for some cracks with slower unloading rates. Some widening during precharging in the "Exposed" cracks.
Striations	Wavy slip observed, indicating the activation of multiple slip systems. May be related to presence of hydrogen aiding dislocation slip.
EDX	Indications of formation of carbonates and potentially hydroxides and oxides were observed in the "Exposed" cracks. Carbonates appeared to form towards the crack tips, while hydroxides/oxides appeared to form along the crack walls nearer to the bulk surface.

5.3 Discussion

The addition of a monotonic hold in near-neutral pH environments has been previously shown to retard crack growth in pipeline steels. However, the effect of a monotonic hold following asymmetrical triangular loading has not yet been studied in this environment.

Specifically, the effect of changing unloading rates on crack growth rates are not known for this set of conditions. This section will explore the mechanisms relevant to crack growth in air, fully-exposed, and hydrogen-rich environments. Understanding of these mechanisms may improve operations relevant to the integrity management of pipelines.

5.3.1 Effect of Unloading Rate

In this study, pipeline steel specimens were loaded in variable amplitude and constant amplitude loading waveforms to explore how changing the unloading rate may affect crack growth rates under different environments. Via SEM fractography, crack growth rates were estimated and the morphology of the crack walls, crack tip at the surface, and the crack tip in the depth direction indicated different responses to unloading rates for the three environments. For similar loading waveforms, the partially-coated cracks showed the highest crack growth rates as a result of hydrogen-enhanced crack growth in the absence of anodic dissolution. Next, the cracks exposed to C2 solution showed greater crack growth relative to the fully-coated cracks, indicating that crack sharpening related to hydrogen ingress has a greater effect than blunting effects due to anodic dissolution. Crack growth rates appeared to have some dependence on unloading rate, especially in the depth direction, for fully exposed and partially coated cracks, suggesting that the accumulation of hydrogen in the fracture process zone influences crack growth behaviour. Previous studies by Sidey and Coffin [74] and Barsom [75] suggest that slow-loading and fast-unloading in an inert environment act to enhance crack growth rates when compared with symmetrical loading rates. Since diffusible atomic hydrogen can act to enhance crack growth in NNpHCF [9, 39], we propose that the synergy of screw dislocation mobility coupled with hydrogen enhanced plasticity is the main mechanism for increased crack growth with higher unloading rates.

The enhancement on crack growth rates due to the presence of hydrogen is observed both at the surface and in the depth of the semi-elliptical cracks studied. From Figure 5.1, a clear trend relating da/dN to dK/dt is observed for cracks fully exposed to C2 solution and partially coated cracks. Furthermore, fully exposed cracks have lower crack growth rates than the partially coated cracks which suggests retardation of crack growth due to anodic dissolution. Egbewande et al. [43] and Been et al. [50] note that dissolution rates in the near-neutral pH environment are less significant compared to crack growth rates

driven by mechanical loading, especially during Stage II crack growth. Additionally, King et al. note that dissolution rates are typically lower in dilute near-neutral pH solutions when compared with higher pH solutions [44], but some anodic dissolution is still possible even when a slightly cathodic potential is applied.

From Figure 5.1, there appears to be a transition at unloading times of approximately 60 s for partially coated samples where the crack growth reaches a maximum for this range of $K_{\max}$ in NNpHCF. In the study by Yu et al. [67], NNpHCF crack growth rates increased as loading frequency decreased for variable amplitude spectra (minor cycles with periodic underloading) down to 1×10^{-3} Hz, where crack growth remained constant for frequencies below the critical value. The change in frequency dependence found by Yu et al. [67] was attributed to the fracture process zone becoming saturated by hydrogen. Coincidentally, the critical frequency at room temperature where screw dislocation mobility becomes significantly less than the mobility of edge dislocations is approximately 1×10^{-3} Hz, as noted by Mughrabi et al. [68]. Based on the step change in crack growth rates in the partially coated cracks of the current study as unloading rate is increased, this information suggests that the locking of screw dislocations contributes to hydrogen segregation. For the fully exposed cracks, it appears that the hydrogen enhancement is insufficient to completely overcome crack tip blunting from anodic dissolution since no step change was observed.

From Xing et al. [122], the accumulation rate of hydrogen into the fracture process zone during loading is much larger than the diffusion rate of hydrogen out of the FPZ. Thus, this difference can effectively be enhanced by restricting the mobility of screw dislocations at sufficiently high unloading rates as noted by Magnin et al. [30]. The consequence of the "slow" loading and rapid unloading would be an even greater accumulation of hydrogen ahead of the crack tip, thus enhancing crack growth in the depth. Similar to the work by Xing et al. [122], it is possible to expand on the work by Song and Curtin [121] and predict the amount of hydrogen accumulated near the crack tip. Song and Curtin related the number of hydrogen atoms per unit thickness in relation to original hydrogen concentration, hydrogen diffusivity, and the temporal changes of stress intensity factor as noted in the below equation:

$$\frac{N_H}{L_z} = \beta\left(\frac{1}{2}, \frac{9}{10}\right)\frac{2c_o}{{a_o}^3}\left[\frac{5(1+\nu)D\Omega\dot{K}_I t^2}{12\sqrt{2\pi}k_B T}\right]^{4/5} \tag{5.1}$$

where $\beta(1/2, 9/10)$ is the beta function, c_o is the original hydrogen/iron concentration, a_o is the lattice parameter, ν is the Poisson ratio, D is the hydrogen diffusivity, Ω is the molar volume of hydrogen, $\dot{K_I}$ is the rate change of stress intensity factor with respect to time, t is the time for loading or unloading, k_B is Boltzmann's constant, and T is temperature [121]. We can assume c_o as 2 appm [122], a_o as 2.856×10^{-10} m [151], ν as 0.3, D_H as $1.7 \times 10^{-9}\,\mathrm{m^2\,s^{-1}}$ [152], Ω as $1.99e-30$ [122], and T as 300 K. Assuming L_z as 24 angstroms [121], we can determine the number of hydrogen atoms that accumulate within this distance ahead of the crack tip as $\dot{K_I}$ and t change for various unloading times. Note that the beta function, also called the Euler integral of the first kind, is represented by:

$$\beta(x, y) = \int_0^1 t^{x-1}(1-t)^{y-1}dt \tag{5.2}$$

See Figure 5.21 for the results of this study, assuming a thickness region of 24 angstroms and a length directly along the crack growth direction of 1 micron. Please note that the fully coated cracks, representing crack growth under inert fatigue, was also included in the plot. An approximate baseline da/dN under inert fatigue was determined to be 0.02 and 0.01 microns per cycle in the depth and at the surface, respectively, for this dataset. Recall from Chapter 4 that in the fully exposed environment, a quasi-equilibrium of various crack-tip sharpening processes (hydrogen-assisted corrosion fatigue) and crack-tip blunting processes (room-temperature creep, anodic dissolution, HELP/AIDE) will manifest in an average da/dN. Also recall that due to partial coating, the "Hydrogen" cracks will have the same set of sharpening and blunting processes with the exception of anodic dissolution. Consequently, we can clearly see a net increase in da/dN with the exposure to C2 solution of the fully exposed cracks, and a further increase in the partially coated cracks. As a result of the quasi-equilibrium established, the critical amount of hydrogen required for significant gains in crack growth rates will depend on the kinetics of the various environmental conditions at play.

At the surface, there is generally less hydrogen segregation to the crack tip as a result of plane stress conditions. Consequently, crack growth rate da/dN is far less sensitive to hydrogen accumulation ahead of the crack tip. The lesser dependence of crack growth at the surface on the unloading rate is also likely related to a higher availability of hydrogen,

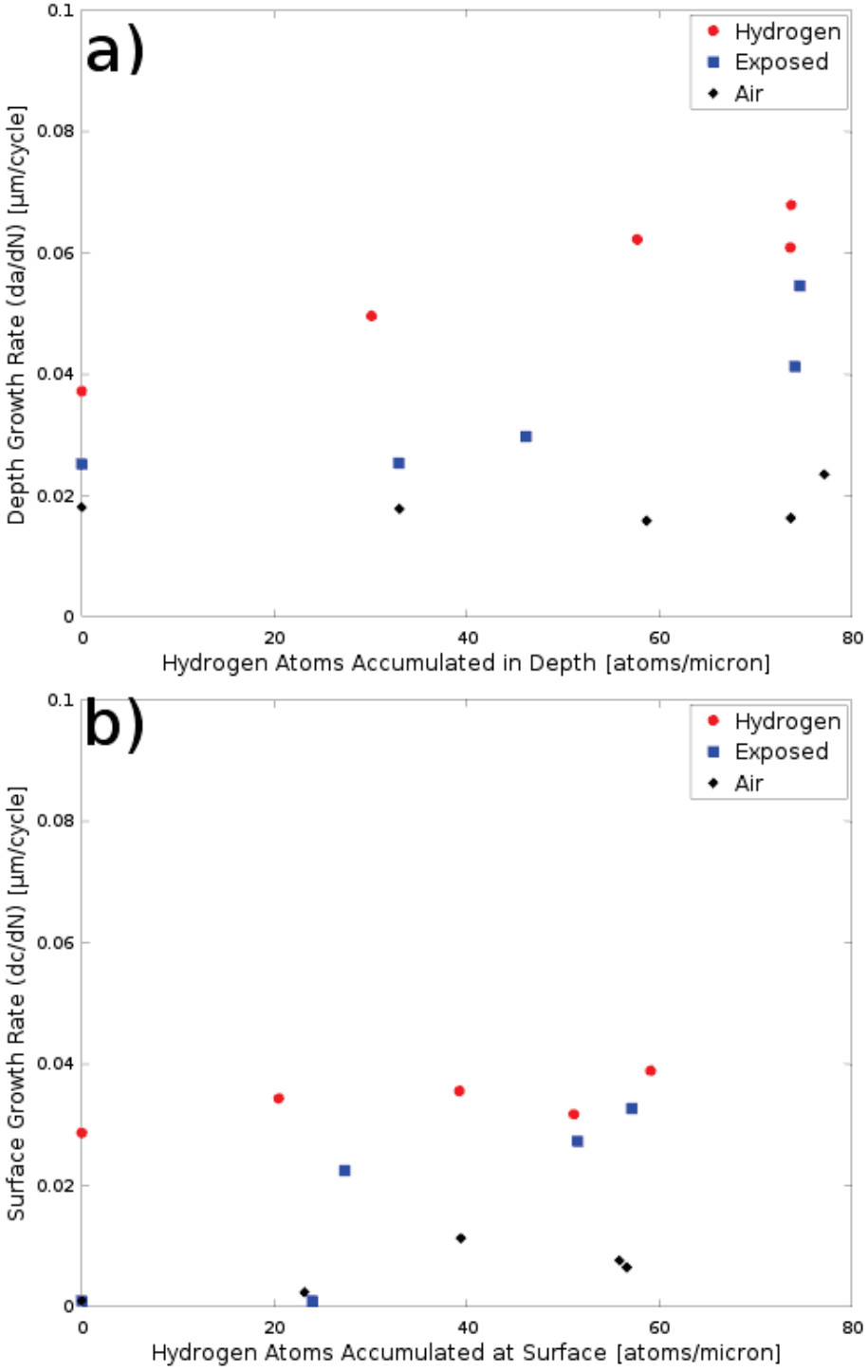

Figure 5.21: Number of hydrogen atoms accumulated within 1 micron of the crack tip a) in the depth direction and b) at the surface.

since hydrogen is generated at the surface of the specimen as a result of dissolution. Further, the presence of a cathodic potential would enhance hydrogen uptake. With the greater amount of hydrogen, the FPZ is likely saturated and effects from unloading rate are relatively less significant. Additionally, it the fully exposed crack undergoes

sufficient crack tip blunting from anodic dissolution, HELP, and RTC to cause the crack to enter a state of dormancy. However, the critical amount of hydrogen within 1 micron of the crack tip is approximately 25 H atoms for a 24 angstrom thickness to overcome these blunting effects. In terms of unloading rate, this is achieved at 60 s unloading time for 500 s loading time followed by a 1-hour monotonic hold. At this concentration, there is enough hydrogen to sufficiently weaken the metal bonds and allow for crack propagation.

In the depth direction, there is a much stronger dependence of da/dN vs H concentration as a result of greater H segregation under plane strain conditions and crack tip stress triaxiality. There is also a seemingly linear dependence of da/dN vs H concentration for the partially coated cracks, but significant rises in da/dN with H concentration for fully exposed cracks are observed at approximately 70 H atoms within 1 micron of the crack tip for a 24 angstrom thickness. It is important to note that the 10 s ULH waveform predicted less hydrogen accumulated within 1 micron of the crack tip than the 30 s ULH waveform. This is likely as a result of the different crack geometries, where the 30 s ULH waveform had a higher initial $K_{\max}$ than the 10 s ULH waveform both in the depth and at the surface of the crack.

Please note that these calculations assume that under symmetrical loading conditions, the number of mobile hydrogen atoms diffusing into the FPZ would equal the number diffusing out. As explored by Xing et al. [122], the number of hydrogen atoms diffusing outwards during unloading is significantly less than the amount diffusing in during loading. Here, we also assume that contributions from hydrogen transported with dislocations are accounted for with an effective diffusivity greater than would typically be predicted by bulk lattice diffusion [152]. There is also the added effect that slip during loading can generally considered as irreversible but relaxation during unloading would have a primarily elastic component. Also recall that at sufficiently high strain rates, the transport of H via dislocations becomes a non-equilibrium process and dislocations will carry less hydrogen [138].

In summary, crack growth rate in the depth direction generally increases due to reduced screw dislocation mobility and less time available for hydrogen to diffuse out of the fracture process zone as the unloading rate is increased. The higher crack growth rates are primarily related to enhanced hydrogen segregation ahead of the crack tip. This

enhancement effect was not observed in the fully coated cracks due to an absence of hydrogen. Similarly, there was little dependence of the crack growth rates at the surface on the unloading rate due to lower amounts of crack tip constraint and therefore less hydrogen segregation towards the crack tip.

5.3.2 Mechanical Driving Forces

All cracks had comparable combined factors (especially in the depth), yet da/dN increased as unloading time decreased. At the surface, some crack growth was observed with a 60 s unloading time despite a lower combined factor and crack arrest being observed for both 250 s and 500 s unloading times. These results suggest that unloading rate may be a significant factor in addition to the already-established combined factor model as summarized by Chen [9]. Results outlined from the previous section are compared with the works by Chen and Sutherby [40], Yu et al. [64], and Engel [144] in Figure 5.22.

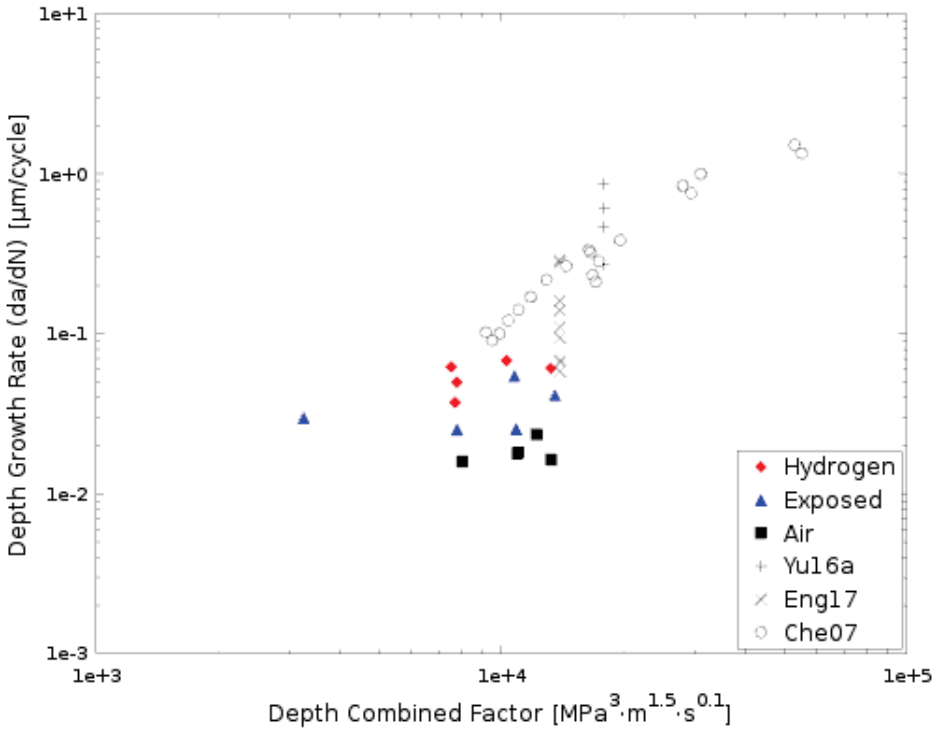

Figure 5.22: Growth per cycle as a function of combined factor in the depth direction for the "Hydrogen", "Exposed", and "Air" environments. Note that all features plotted from the current study were tested with the ULH type waveform at various unloading times. Data from the works by Yu et al. (Yu16a) [64], Engel (Eng17) [144], and Chen and Sutherby (Che07) [40] are included here.

The crack growth rates from the current study appear to be within range, albeit lower than the aforementioned references. Although higher H concentrations would be expected as a result of applied cathodic potentials, the lower mechanical forces represented by the combined factor led to lower crack growth rates. Deviations from the combined factor model, initially proposed by Chen et al. [40], can be due to differences in crack morphology since the original model used standard fracture mechanics CT specimens instead of the surface semi-elliptical cracks used in this study. Further, the initial model was developed for a $K_{\max}$ of 35 to 55 MPa m$^{0.5}$ and ΔK of 10 to 28 MPa m$^{0.5}$; the current study tested $K_{\max}$ between 7 and 21 MPa m$^{0.5}$ as well as ΔK between 6 and 19 MPa m$^{0.5}$. Similarly, the work by Yu et al. [64] used CT specimens and greater stress intensities. One additional cause for discrepancy is that the work by Chen and Sutherby [40] used constant amplitude triangular waveform loading, whereas the data from the current study was based on block loading of an underload waveform with a 1-hour monotonic hold. Although similar crack growth rates were achieved as in the work by Engel [144], note that those results are from underloading and minor cycling as well as underload and static hold waveforms but at the open circuit potential. Further, the environmental conditions were different in the work by Engel [144] due to the simulation of a disbonded coating, compared with the current study which would more represent a crack exposed to bulk solution.

As discussed by Martinez-Paneda et al. [58], SGP may be significant in contributing to a higher amount of hydrogen being trapped within the FPZ as a result of higher stresses and strains generated in the 1-2 microns ahead of the crack tip, as well as the generation of geometrically necessary dislocations that can act as a reservoir for atomic hydrogen. SGP theory per Martinez-Paneda et al. [58] support our assumption that the majority of hydrogen is trapped within 1 micron ahead of the crack tip, as previously noted by Toribio [141]. However, please note that our calculations in the previous section on unloading rate use a rudimentary Irwin approximation for the plastic zone and do not account for added gradients related to SGP.

Note that the threshold for crack growth should be different at the surface of the crack (length direction) as opposed to growth in the depth direction. It is expected that a higher amount of crack tip constraint in the depth direction will occur, thus allowing for more triaxial stresses to build up and therefore promoting hydrogen segregation to the crack tip under plane strain conditions. Further, it is important to consider the differing

hydrogen concentrations with respect to depth, since a higher initial depth effectively raises the distance from the source of hydrogen (H uptake at the bulk surface as a result of enhancement from cathodic potentials).

Not every loading event will cause crack propagation. Assuming that the average striation width is on the order of 0.1 microns, we can clearly see from the da/dN that the overall crack growth rate is approximately 5-10 times less than the striation width. Several cycles are likely required to generate enough irreversible dislocation slip corresponding to the formation of a single striation, as corroborated by the review by Davidson and Lankford [27]. This phenomenon is likely due to the low ΔK experienced at the crack surface and in the depth direction, related to a Stage I to Stage II transition where $\log(da/dN)$ may not be fully linear with respect to $\log(\Delta K)$.

Crack growth rates for partially-coated specimens is within one order of magnitude of that in fully coated specimens, and greater differences may be observed at higher stress intensity ranges [116, 126]. The work by Cotterill and King [126] did not show significant hydrogen contribution to crack growth at stress intensity ranges less than $20\,\mathrm{MPa\,m^{0.5}}$. Additionally, the brittle striation spacing was 3.5 ± 1 micron due to the higher stress intensity range of $35\,\mathrm{MPa\,m^{0.5}}$ [126]. The high-magnification fractographs in the current study only showed ductile striations and this is one reason for a relatively smaller striation width (on the order of 0.1 microns). At higher stress intensity ranges (e.g. $35\,\mathrm{MPa\,m^{0.5}}$ as in the work by Cotterill and King [126], larger striation widths and a greater number of quasicleavage facets would be expected in observations due to higher hydrogen activity.

In summary, the crack growth rates in the current study may deviate from the crack growth rates as predicted by the combined factor model from Chen et al. [40]. Some reasons for this discrepancy include the use of surface cracks in the current study as opposed to CT specimens that the model was based on, added crack tip constraint from strain gradient plasticity that may not be fully accounted for in the combined factor model, and low stress intensities that are closer to near-threshold growth in the current study as opposed to Stage II crack growth in the model.

5.3.3 Hydrogen Diffusion Pathways

From the above, it was proposed that hydrogen plays a key role in crack growth behaviour when the unloading rate is changed. Understanding the diffusion pathway that H will take towards the fracture process zone helps to explain the influence of hydrogen on crack growth.

Hydrogen will be generated at the bulk surface as a result of corrosion, and atomic hydrogen will uptake into the steel. H can then diffuse via grain boundaries, "bulk" diffusion through normal interstitial lattice sites (NILS), and via dislocation transport which is aided by cyclic slip [138, 140]. H segregates toward the fracture process zone since a chemical potential gradient is established as a result of the expanded lattice [122]. Various traps due to inclusions (such as TiC and MnS), grain boundaries, persistent slip bands, immobile dislocations, and dislocation subcells will cause an effective increase in solubility and decrease in diffusivity.

Per Gangloff's definition [52], the system studied here is likely a combination of both IHAC and HEAC, with a greater contribution from IHAC. H would be primarily introduced from the external bulk surface away from the crack tip, due to the enhanced uptake of H as a result of cathodic current flowing through the steel [39, 119]. The greater contribution from IHAC is further corroborated by the work by Turnbull [61], who notes that crack tip charging is typically more significant only at potentials more negative than -1000 mV(SCE). Further, recall that a higher concentration of H dissolved in the lattice will decrease the threshold stress intensity and increase the subcritical crack growth rates for IHAC [52, 129–133]. Considering the potential rate-limiting steps as per Nanninga and White [116], the current work most likely shows the effects of the rate of creation of a new crack surface as well as the rate of diffusion of H to the fracture process zone. The rate of hydrogen dissociation and adsorption is likely insignificant under the conditions studied due to the relatively long hydrogen pre-charging times where a significant portion of the specimen have hydrogen traps already saturated.

5.3.4 Plastic Damage and Room-Temperature Creep

Recall from the study by Yu et al. [64] that the average crack growth rates are reached once a state of quasi-equilibrium is established between various time-dependent processes. As the crack propagates, mobile dislocations are exhausted and crack blunting due to room-temperature creep occurs. Precyclic loading will change the residual stress profiles, as discussed by Chen et al. [111]. Conversely, the overall crack size will increase and therefore stresses ahead of the crack tip also increase. Consequently, increased hydrogen segregation to the crack tip occurs which acts to propagate and sharpen the crack. With the shallow initial crack depths in this study (generally less than 1 mm), the change in residual stress will also affect the thermodynamics of hydrogen segregation towards the crack tip. Comparing the crack tips in this study with other works [10, 48, 145], there is evidence suggesting that crack bifurcation and discontinuous crack is at play. The 1-hour hold provides additional time for diffusible hydrogen to segregate to the crack tip as a result of a chemical potential gradient.

5.3.5 Crack Chemistry Considerations

As seen from the micrographs of the fractured specimens that were fully exposed to the C2 solution, more rapid fluid flow out of the crack has resulted in a more distributed corrosion product. Generally however, a lighter corrosion product is observed to build toward the bottom of the crack and a darker corrosion product is formed near the surface of the crack. Recall from the work by Turnbull [107] that the effect from advection is actually less significant for shorter cracks since there would be more mixing with the bulk solution. Prior studies by Zhang et al. [41] and Chen and Sutherby [40] suggest higher dissolution rates at the surface. Restricted mass transport can be expected within the relatively low crack mouth opening displacement, especially at the lower stress intensity factors experienced as a result of the surface crack geometries.

Turnbull [61] has noted a considerable effect of an increased ΔK with a constant stress ratio R, leading to a higher $K_{\max}$ and a consequently larger crack mouth opening displacement and volume-to-area ratio within the crack. The significance of the volume-to-area ratio is that the concentration of hydrogen ions available within the crack is directly affected, thus changing pH [61]. A decreased $K_{\max}$ will correspond to a lower

pH; conversely, an increased $K_{\max}$ will correspond to a higher pH. With this in mind, the current study uses a relatively low $K_{\max}$ compared with other tests that use compact tension specimens with a larger initial crack size and therefore higher $K_{\max}$. Therefore, significant deviation from the model predicted by Chen et al. [40] is expected.

Furthermore, the differing geometries of surface cracks with standard fracture mechanics compact tension specimens is yet another cause for deviation between the current dataset and the combined factor model by Chen et al. [40]. Increased mixing with the bulk solution would be expected in compact tension specimens as opposed to the relatively constrained geometry of surface cracks. As discussed by Turnbull [143], the through-thickness crack nature of most fracture mechanics specimens generates an artefact of testing, since mass is not truly conserved when fluid is allowed to flow in the through-thickness direction. Turnbull also notes that the formation of precipitates will restrict crack flow and mass transport within the crack [143].

In addition to differences caused by crack geometries, it is also important to consider the effect of applied cathodic potential, as used in this study. As noted by Chen et al. [89], more negative applied potentials can generally be cause for an increase in pH. However, constant supply of CO_2 in the simulated deaerated environment will maintain levels of carbonic acid and the subsequent dissociation of carbonic acid into hydrogen carbonate and carbonate ions will allow for maintenance of near-neutral pH [89].

As observed from the fractographs and supplementary EDX analysis, formation of iron carbonates and hydroxides resulted. King et al. [44] noted that localized corrosion was still possible and this phenomenon was confirmed via some corrosion of the crack walls as well as minor pitting observed at the steel surface. However, the formation of iron carbonate and hydroxide films are expected to inhibit cathodic currents and reduce the surface area of steel available for anodic reaction, thereby providing another mechanism to maintain pH near 7 [44, 89].

Furthermore, reduced corrosion rates as a result of both cathodic protection and film formation will decrease the overall amount of hydrogen generated within the crack, as well as the diffusion rate of hydrogen from the crack walls to the crack tip and FPZ. However, since localized dissolution is still possible at the bulk steel surface, generation of atomic hydrogen is still expected to occur at the surface and gradually diffuse in the depth direction. Ultimately, hydrogen segregation will occur at the crack tip and FPZ,

thus still allowing for hydrogen-enhanced crack growth. Localized corrosion is expected due to the presence of sulfate, chloride, and nitrate ions as discussed by Patel [93] and Beavers and Harle [91].

With regards to crack chemistry, the increased constraint of a surface crack will have different diffusion pathways for hydrogen to enter the fracture process zone. The combination of increased constraint and the application of cathodic potentials will allow the formation of oxides and carbonates in this environment which will restrict the cathodic current and mass transport within the crack.

5.3.6 Sources of Error

Although some trends were observed, there are inherent variations during testing that will affect the results. Residual stress profiles from machining will vary (although milling was controlled as carefully as possible). Further, another key source of variation would be the measurement error during microscopy. Replication damage could also have occurred during the replication process, as well as during SEM imaging from the electron beam. There may also be some variations in the tensile strength of the specimens, although these errors were mitigated by taking the samples from the same cut of pipe. Crack closure effects from the coatings are considered negligible in this study due to the narrow crack mouth opening as well as the relatively low crack depths. Further, there is also potential for measurement error, due to relatively low total crack growth both in the depth and at the surface.

The calculations in Figure 5.21 that predict the amount of hydrogen accumulated ahead of the crack tip assumes that the diffusivity of H accounts for diffusion assisted by hydrogen locked in dislocation cores, as well as diffusion along grain boundaries, in addition to bulk diffusion. More detailed modeling would be required to validate this phenomenon of hydrogen accumulation, but the current study shows a comparison to depict the relative effects of loading-unloading asymmetry. The work by Dadfarnia et al. [138] note that the amount of H transported via dislocations become especially important when NILS diffusivity is less significant and if there is a substantial amount of hydrogen trapping sites.

Due to specimen geometries, the current study more closely simulates circumferential instead of axial crack orientations. Although NNpHCF typically produces axial cracks, the crack growth behaviour in the depth should be similar. However, crack growth at the surface may not be representative of axial cracks due to crack growth being perpendicular to the rolling direction of the pipe since more microstructural barriers to crack growth would be present.

Due to the small crack sizes and stress intensity factors being near threshold, there is a potential for a significant amount of the fracture process zone being undergoing plastic deformation. Akid defines the transition between EPFM and LEFM to be approximately $a/r_p = 50$ [20], and current crack depths relative to the plastic zone size do not exceed this ratio. However, we can conclude that the cracks are nominally in LEFM from the thin-walled crack morphologies in the cross-section micrographs.

5.3.7 Future Work

Additional testing for statistical validation is recommended to further explore this phenomenon. Further, testing on other grades of steel and various ranges of $K_{\max}$, ΔK, holding times, and waveform shapes are recommended to further demarcate potential changes in crack behaviour with the addition of a monotonic hold. Further refinement of modelling, as well as a fully-coupled model for stress, strain, dislocation motion, and hydrogen diffusion under varying stresses, cathodic potentials, and hydrogen concentrations.

5.3.8 Impacts on Pipeline Integrity Management

Considering the above, pipeline operators can optimize their operations to minimize rapid depressurization events (especially so for liquids transmission, due to the nominal incompressibility of liquids) in order to extend the lifetime of their assets. Since strict control of pressurization and de-pressurization rates are not always possible or practical, the consideration of pressure change rates over time could be used as an added criterion when evaluating the remaining corrosion fatigue life of an asset. The pressure rate effects would be expected to be more pronounced under near-neutral pH conditions promoting hydrogen-enhanced fatigue.

5.4 Summary

The work in this chapter compared the crack growth behaviour of fully-coated, partially-coated, and fully-exposed semi-elliptical cracks immersed in a near-neutral pH environment with an applied cathodic potential. The effect of reducing the unloading time was studied. Reduced unloading times allowed for increased segregation of hydrogen to the crack tip as a result of restricted screw dislocation motion and elastic lattice response. Greater hydrogen effects were observed in the depth compared with the surface of the cracks due to differences in hydrogen concentrations and crack tip stresses. Consequently, greater crack growth rates were observed with lesser unloading times and increased segregation of hydrogen to the crack tip for the fully exposed and partially coated cracks. Fully coated cracks showed a negligible dependence on unloading rate. Sufficiently high unloading rates may allow for cracks to enter an active growth state.

Chapter 6

Conclusions and Future Work

6.1 Conclusions

This thesis has studied the crack growth behaviour of fully-coated, partially-coated, and fully-exposed semi-elliptical cracks immersed in a near-neutral pH environment with an applied cathodic potential.

The effect of adding a one-hour monotonic hold was explored. The addition of a one-hour hold was shown to cause crack arrest at the surface of the cracks for fully-coated specimen due to room-temperature creep. Similarly, crack arrest was observed in the fully-exposed specimen likely due to a combination of room-temperature creep, anodic dissolution, and hydrogen-enhanced localized plasticity. Further, enhanced crack growth from increased hydrogen concentrations at the crack tip due to crack morphology and applied cathodic potentials may be enough to overcome retardation effects expected from an applied static hold.

Rapid unloading was found to enhance crack growth, suggesting that waveform shape can significantly affect crack growth behaviour during variable amplitude loading in corrosion fatigue due to enhanced hydrogen segregation. The effect of reducing the unloading time was studied. Reduced unloading times allowed for increased segregation of hydrogen to the crack tip as a result of changed screw dislocation motion and elastic lattice response. Greater hydrogen effects were observed in the depth compared with the surface of the cracks due to differences in hydrogen concentrations and crack tip stresses. Consequently, greater crack growth rates were observed with lesser unloading times and

increased segregation of hydrogen to the crack tip for the fully exposed and partially coated cracks. Fully coated cracks showed a negligible dependence on unloading rate. Sufficiently high unloading rates may allow for cracks to enter an active growth state.

6.2 Implications on Pipeline Integrity Management

With the above information, pipeline operators can optimize their hydrostatic test programs to minimize the amount of potential crack growth during operations and fitness-for-service testing. Following the work by Yu et al. [64], a static hold at maximum operating pressure can retard subsequent crack growth in the length direction, especially following a significant depressurization-repressurization event. However, cracks may still grow in the depth direction. One key finding from the current study is differentiating the relative contributions from inert fatigue and hydrogen enhanced fatigue under cathodic protection.

Considering the unloading rates, pipeline operators can optimize their operations to minimize rapid depressurization events (especially so for liquids transmission, due to the nominal incompressibility of liquids) to extend the lifetime of their assets. Since strict control of pressurization and de-pressurization rates are not always possible or practical, the consideration of pressure change rates over time could be used as an added criterion when evaluating the remaining corrosion fatigue life of an asset. The pressure rate effects would be expected to be more pronounced under near-neutral pH conditions promoting hydrogen-enhanced fatigue.

6.3 Future Work

As seen from the current study, near neutral pH corrosion fatigue is an incredibly complex and complicated phenomenon. Many subsequent studies can be performed in order to better understand the effects of strain rate and hydrogen on crack growth rate. Similar studies with added specimen counts can also be performed for added statistical validation.

Material considerations including the effects from interaction with mill scale, changed microstructure in the heat-affected-zone near longitudinal seam welds, and crack growth behaviour in various material grades in NNpHCF conditions can be explored.

Environmental considerations including the presence of organics in solution and the effect on hydrogen permeation in the steel, as well as varying concentrations of sulfides that may increase the subsurface hydrogen concentration may also be explored. Better understanding of the effects of cracks shifting between active and dormant states under varying CO_2 concentrations can also be studied.

Other mechanical considerations include studying the effects of NNpHCF behaviour under constant displacement conditions and mixed-mode loading can be explored. Different crack geometries and specimens may allow for better simulation of field conditions. Further, the interaction of multiple cracks (coplanar or otherwise) can also be studied and modeled.

Furthermore, new characterization techniques can be developed or used to study NNpHCF cracking, including ultrasonic methods, eddy current, and acoustic emissions. Higher-resolution testing such as atomic force microscopy can also be used to image and study striation growth.

Many opportunities for modeling are also present, including the potential to couple fluid flow with hydrogen diffusion and crack propagation. Furthermore, additional molecular dynamics modeling can be performed to study the behaviour of dislocation subcells present within the fracture process zone.

References

[1] "Pipelines across canada." `http://www.nrcan.gc.ca/energy/infrastructure/18856`, accessed 2019-01-24.

[2] J. J. HARWOOD, "The influence of stress on corrosion (part 1 of two parts)," *CORROSION*, vol. 6, no. 8, pp. 249–259, 1950.

[3] J. J. HARWOOD, "The influence of stress on corrosion (part ii of two parts)," *Corrosion*, vol. 6, no. 9, pp. 290–307, 1950.

[4] J. A. Beavers, "2013 frank newman speller award lecture: Integrity management of natural gas and petroleum pipelines subject to stress corrosion cracking," *CORROSION*, vol. 70, no. 1, pp. 3–18, 2014.

[5] B. Delanty and J. O'Beirne, "Major field study compares pipeline SCC [stress corrosion cracking] with coatings," *Oil and Gas Journal*, vol. 90, no. 24, pp. 39 – 44, 1992.

[6] J. A. Beavers and B. A. Harle, "Mechanisms of high-ph and near-neutral-ph scc of underground pipelines," in *International Pipeline Conference*, vol. 1, pp. 555–564, New York: ASME, 1996.

[7] B. T. Lu, F. Song, M. Gao, and M. Elboujdaini, "Crack growth model for pipelines exposed to concentrated carbonate–bicarbonate solution with high pH," *Corrosion Science*, vol. 52, pp. 4064 – 4072, 2010.

[8] B. T. Lu, F. Song, M. Gao, and M. Elboujdaini, "Crack growth prediction for underground high pressure gas lines exposed to concentrated carbonate–bicarbonate solution with high pH," *Engineering Fracture Mechanics*, vol. 78, pp. 1452 – 1465, 2011.

[9] W. Chen, "An overview of near-neutral ph stress corrosion cracking in pipelines and mitigation strategies for its initiation and growth," *CORROSION*, vol. 72, no. 7, pp. 962–977, 2016.

[10] R. N. Parkins, W. K. J. Blanchard, and B. S. Delanty, "Transgranular stress corrosion cracking of high-pressure pipelines in contact with solutions of near neutral pH," *Corrosion*, vol. 50, pp. 394 – 408, 1994.

[11] R. N. Parkins and J. A. Beavers, "Some effects of strain rate on the transgranular stress corrosion cracking of ferritic steels in dilute near-neutral-ph solutions," *CORROSION*, vol. 59, no. 3, pp. 258–273, 2003.

[12] A. D. Batte, R. R. Fessler, J. E. Marr, and S. C. Rapp, "A new joint-industry project addressing the integrity management of scc in gas transmission pipelines.," *Journal of Pipeline Engineering*, vol. 11, no. 2, pp. 93 – 116, 2012.

[13] A. D. Batte, R. R. Fessler, J. E. Marr, and S. C. Rapp, "Managing the threat of scc in gas transmission pipelines," in *2012 9th International Pipeline Conference*, pp. 379–388, American Society of Mechanical Engineers, 2012.

[14] J. Zhao, K. Chevil, M. Yu, J. Been, S. Keane, G. V. Boven, R. Kania, and W. Chen, "Statistical analysis on underload-type pipeline spectra," *Journal of Pipeline Systems Engineering and Practice*, vol. 7, no. 4, Issue: object: doi:10.1061/ps.2016.7.issue-4, revision: rev:1479533476797-40289:doi:10.1061/ps.2016.7.issue-4, .

[15] M. Yu, W. Chen, R. Kania, G. V. Boven, and J. Been, "Crack propagation of pipeline steel exposed to a near-neutral ph environment under variable pressure fluctuations," *International Journal of Fatigue*, vol. 82, Part 3, pp. 658 – 666, 2016.

[16] J. Zhao, W. Chen, S. Keane, J. Been, and G. Van Boven, "Development and validation of load-interaction based models for crack growth prediction," in *2014 10th International Pipeline Conference*, pp. V002T06A077–V002T06A077, American Society of Mechanical Engineers, 2014.

[17] D. L. McDowell, "Basic issues in the mechanics of high cycle metal fatigue," *International Journal of Fracture*, vol. 80, no. 2, p. 103, 2004.

[18] D. Davidson, K. Chan, R. McClung, and S. Hudak, "4.05 - small fatigue cracks," in *Comprehensive Structural Integrity* (I. Milne, R. O. Ritchie, and B. Karihaloo, eds.), pp. 129 – 164, Oxford: Pergamon, 2003.

[19] M. Smith, *Fitness for Service, API 579-1/ASME FFS-1.* American Petroleum Institute, edition ed., 2016.

[20] R. Akid, "2.12 - corrosion fatigue*," in *Shreir's Corrosion* (B. Cottis, M. Graham, R. Lindsay, S. Lyon, T. Richardson, D. Scantlebury, and H. Stott, eds.), pp. 928 – 953, Oxford: Elsevier, 2010.

[21] K. J. Miller, "Materials science perspective of metal fatigue resistance," *Materials Science and Technology*, vol. 9, no. 6, pp. 453–462, 1993.

[22] D. Taylor and J. F. Knott, "Fatigue crack propagation behaviour of short cracks; the effect of microstructure," *Fatigue and Fracture of Engineering Materials and Structures*, vol. 4, no. 2, pp. 147–155, 1981.

[23] B. Tomkins, "Fatigue crack propagation–an analysis," *Philosophical Magazine*, vol. 18, no. 155, pp. 1041–1066, 1968.

[24] Y.-P. Kim, C.-M. Kim, W.-S. Kim, K.-S. Song, and K.-S. Shin, "Near-threshold fatigue crack growth behavior and crack closure of natural gas pipeline steels," *Procedia Engineering*, vol. 10, pp. 813–820, 2011.

[25] P. C. Paris and F. Erdogan, "A critical analysis of crack propagation laws," ASME, 1963.

[26] S. Tiku, A. Dinovitzer, V. Semiga, M. Piazza, and T. Jones, "Improvement of pipeline fatigue life estimation," in *2016 11th International Pipeline Conference*, pp. V001T03A026–V001T03A026, American Society of Mechanical Engineers, 2016.

[27] D. L. Davidson and J. Lankford, "Fatigue crack-growth in metals and alloys: Mechanisms and micromechanics," *International Materials Reviews*, vol. 37, no. 2, pp. 45 – 76, 1992.

[28] N. Grinberg, "Stage ii fatigue crack growth," *International Journal of Fatigue*, vol. 6, no. 4, pp. 229 – 242, 1984.

[29] H. Mughrabi, "Microstructural fatigue mechanisms: Cyclic slip irreversibility, crack initiation, non-linear elastic damage analysis," *International Journal of Fatigue*, vol. 57, pp. 2 – 8, 2013.

[30] T. Magnin and J. Driver, "The influence of strain rate on the low cycle fatigue properties of single crystals and polycrystals of two ferritic alloys," *Materials Science and Engineering*, vol. 39, no. 2, pp. 175 – 185, 1979.

[31] T. Magnin, A. Fourdeux, and J. Driver, "Fatigue-induced shear bands in ferritic single crystals," *Acta Metallurgica*, vol. 30, no. 1, pp. 273 – 278, 1982.

[32] T. Magnin, L. Coudreuse, and A. Fourdeux, "Consequences of slip-twinning interactions on the monotonic and cyclic deformation of b.c.c. stainless steels," *Materials Science and Engineering*, vol. 63, no. 1, pp. L5 – L8, 1984.

[33] U. F. Kocks, "A statistical theory of flow stress and work-hardening," *The Philosophical Magazine: A Journal of Theoretical Experimental and Applied Physics*, vol. 13, no. 123, pp. 541–566, 1966.

[34] B. N. Leis, R. Rungta, M. E. Mayfield, and J. A. Beavers, "Corrosion-fatigue crack initiation in an iron-caustic system," in *Corrosion Fatigue: Mechanics, Metallurgy, Electrochemistry, and Engineering (ASTM STP 801)*, pp. 197–228, ASTM International, 1983.

[35] R. Akid, "The influence of environment upon the accumulation of damage under corrosion fatigue conditions," *Fatigue & Fracture of Engineering Materials & Structures*, vol. 19, no. 2-3, pp. 277–285, 1996.

[36] W. Bouaeshi, S. Ironside, and R. Eadie, "Research and cracking implications from an assessment of two variants of near-neutral pH crack colonies in liquid pipelines," *Corrosion*, vol. 63, no. 7, pp. 648 – 660, 2007.

[37] A. Boukerrou and R. Cottis, "Crack initiation in the corrosion fatigue of structural steels in salt solutions," *Corrosion Science*, vol. 35, no. 1, pp. 577 – 585, 1993. Advances in Corrosion and Protection.

[38] K. J. Miller and R. Akid, "The application of microstructural fracture mechanics to various metal surface states," *Proceedings of the Royal Society of London A:*

Mathematical, Physical and Engineering Sciences, vol. 452, no. 1949, pp. 1411–1432, 1996.

[39] W. Chen, R. Kania, R. Worthingham, and G. V. Boven, "Transgranular crack growth in the pipeline steels exposed to near-neutral pH soil aqueous solutions: The role of hydrogen," *Acta Materialia*, vol. 57, pp. 6200 – 6214, 2009.

[40] W. Chen and R. L. Sutherby, "Crack growth behavior of pipeline steel in near-neutral pH soil environments," *Metallurgical and Materials Transactions A*, vol. 38A, no. 6, pp. 1260 – 1268, 2007.

[41] J. Zhao, W. Chen, M. Yu, K. Chevil, R. Eadie, G. Van Boven, R. Kania, J. Been, and S. Keane, "Crack growth modeling and life prediction of pipeline steels exposed to near-neutral ph environments: Dissolution crack growth and occurrence of crack dormancy in stage i," *Metallurgical and Materials Transactions A*, vol. 48, no. 4, pp. 1629–1640, 2017.

[42] K. Sadananda, A. Vasudevan, and R. Holtz, "Extension of the unified approach to fatigue crack growth to environmental interactions," *International Journal of Fatigue*, vol. 23, pp. 277 – 286, 2001.

[43] A. Egbewande, W. Chen, R. Eadie, R. Kania, G. Van Boven, R. Worthingham, and J. Been, "Transgranular crack growth in the pipeline steels exposed to near-neutral pH soil aqueous solutions: Discontinuous crack growth mechanism," *Corrosion Science*, vol. 83, pp. 343 – 354, 2014.

[44] F. King, T. R. Jack, W. Chen, M. J. Wilmott, R. R. Fessler, K. Krist, *et al.*, "Mechanistic studies of initiation and early stage crack growth for near-neutral pH SCC on pipelines," in *CORROSION 2000*, NACE International, 2000.

[45] W. Chen and R. Sutherby, "Environmental effect of crack growth rate of pipeline steel in near-neutral pH soil environments," in *2004 International Pipeline Conference*, pp. 123–132, American Society of Mechanical Engineers, 2004.

[46] B. Gu, W. Z. Yu, J. L. Luo, and X. Mao, "Transgranular stress corrosion cracking of X-80 and X-52 pipeline steels in dilute aqueous solution with near-neutral pH," *Corrosion*, vol. 55, no. 3, pp. 312 – 318, 1999.

[47] W. Chen, F. King, and E. Vokes, "Characteristics of near-neutral-pH stress corrosion cracks in an X-65 pipeline," *Corrosion*, vol. 58, no. 3, pp. 267 – 275, 2002.

[48] J. A. Beavers, C. E. Jaske, and R. R. Fessler, "Effect of pressure fluctuations on the propagation and dormancy of near neutral ph stress corrosion cracks in underground petroleum pipelines," in *Proceedings of 15th EPRG-PRCI Joint Technical Meeting on Pipeline Research, Orlando, USA*, 2005.

[49] J. Burns, R. Bush, J. Ai, J. Jones, Y. Lee, and R. Gangloff, "Effect of water vapor pressure on fatigue crack growth in al–zn–cu–mg over wide-range stress intensity factor loading," *Engineering Fracture Mechanics*, vol. 137, no. Supplement C, pp. 34 – 55, 2015. Corrosion Fatigue.

[50] J. Been, R. Eadie, and R. Sutherby, "Prediction of environmentally assisted cracking on gas and liquid pipelines.," in *6TH ASME International Pipeline Conference [IPC 2006] (Calgary, Alberta, 9/25-29/2006) Proceedings*, no. IPC2006-10345, pp. 517 – 531, 2006.

[51] J. Newman and I. Raju, "Stress-intensity factor equations for cracks in three-dimensional finite bodies," in *Fracture Mechanics: Fourteenth Symposium—Volume I: Theory and Analysis*, ASTM International, 1983.

[52] R. Gangloff, "6.02 - hydrogen-assisted cracking," in *Comprehensive Structural Integrity* (I. Milne, R. O. Ritchie, and B. Karihaloo, eds.), pp. 31 – 101, Oxford: Pergamon, 2003.

[53] N. A. Fleck, "Fatigue crack growth due to periodic underloads and overloads," *Acta Metallurgica*, vol. 33, pp. 1339 – 1354, 1985.

[54] J. Rice and G. Rosengren, "Plane strain deformation near a crack tip in a power-law hardening material," *Journal of the Mechanics and Physics of Solids*, vol. 16, no. 1, pp. 1 – 12, 1968.

[55] J. R. Rice, "A path independent integral and the approximate analysis of strain concentration by notches and cracks," *Journal of applied mechanics*, vol. 35, no. 2, pp. 379–386, 1968.

[56] N. Fleck and J. Hutchinson, "A reformulation of strain gradient plasticity," *Journal of the Mechanics and Physics of Solids*, vol. 49, no. 10, pp. 2245 – 2271, 2001.

[57] J. W. Hutchinson, "Plasticity at the micron scale," *International Journal of Solids and Structures*, vol. 37, no. 1, pp. 225 – 238, 2000.

[58] E. Martínez-Pañeda, C. F. Niordson, and R. P. Gangloff, "Strain gradient plasticity-based modeling of hydrogen environment assisted cracking," *Acta Materialia*, vol. 117, pp. 321 – 332, 2016.

[59] Y. Wei and J. W. Hutchinson, "Steady-state crack growth and work of fracture for solids characterized by strain gradient plasticity," *Journal of the Mechanics and Physics of Solids*, vol. 45, no. 8, pp. 1253 – 1273, 1997.

[60] E. Martínez-Pañeda and C. Betegón, "Modeling damage and fracture within strain-gradient plasticity," *International Journal of Solids and Structures*, vol. 59, pp. 208 – 215, 2015.

[61] A. Turnbull and D. Ferriss, "Mathematical modelling of the electrochemistry in corrosion fatigue cracks in structural steel cathodically protected in sea water," *Corrosion Science*, vol. 26, no. 8, pp. 601 – 628, 1986.

[62] Y. Kondo, "4.10 - fatigue under variable amplitude loading," in *Comprehensive Structural Integrity* (I. Milne, R. O. Ritchie, and B. Karihaloo, eds.), pp. 253 – 279, Oxford: Pergamon, 2003.

[63] Y.-H. Zhang and S. Maddox, "Investigation of fatigue damage to welded joints under variable amplitude loading spectra," *International Journal of Fatigue*, vol. 31, no. 1, pp. 138 – 152, 2009. Fatigue assessment of welded connections.

[64] M. Yu, W. Chen, K. Chevil, G. Van Boven, and J. Been, "Retarding crack growth by static pressure hold for pipeline steel exposed to a near-neutral pH environment," in *2016 11th International Pipeline Conference*, pp. V001T03A091–V001T03A091, American Society of Mechanical Engineers, 2016.

[65] T. M. Ahmed, S. B. Lambert, R. Sutherby, and A. Plumtree, "Cyclic crack growth rates of X-60 pipeline steel in a neutral dilute solution," *Corrosion*, vol. 53, no. 7, pp. 581 – 590, 1997.

[66] M. Yu, W. Chen, R. Kania, G. Van Boven, and J. Been, "Depressurization-induced crack growth enhancement for pipeline steels exposed to near-neutral

pH environments," in *10th ASME International Pipeline Conference Proceedings*, no. IPC2014-33282, 2014.

[67] M. Yu, X. Xing, H. Zhang, J. Zhao, R. Eadie, W. Chen, J. Been, G. Van Boven, and R. Kania, "Corrosion fatigue crack growth behavior of pipeline steel under underload-type variable amplitude loading schemes," *Acta Materialia*, vol. 96, pp. 159 – 169, 2015.

[68] H. Mughrabi, K. Herz, and X. Stark, "The effect of strain-rate on the cyclic deformation properties of α-iron single crystals," *Acta Metallurgica*, vol. 24, no. 7, pp. 659–668, 1976.

[69] H. Solomon and G. McMahon, "Solute effects in micro and macroyielding of iron at low temperatures," *Acta Metallurgica*, vol. 19, no. 4, pp. 291 – 302, 1971.

[70] T. Magnin and L. Coudreuse, "The effects of strain rate on the corrosion fatigue behaviour of b.c.c. fe-26cr-1mo stainless steels," *Materials Science and Engineering*, vol. 72, no. 2, pp. 125 – 134, 1985.

[71] J. W. Christian, "Letter to the editor: The stress dependence of dislocation velocity, and its relation to the strain rate sensitivity," *Acta Metallurgica*, vol. 12, pp. 99 – 102, 1964.

[72] S.-H. Wang and W. Chen, "Room temperature creep deformation and its effect on yielding behaviour of a line pipe steel with discontinuous yielding," *Materials Science and Engineering A*, vol. 301, pp. 147 – 153, 2001.

[73] A. Oehlert and A. Atrens, "Room temperature creep of high strength steels," *Acta Metallurgica et Materialia*, vol. 42, no. 5, pp. 1493 – 1508, 1994.

[74] D. Sidey and L. Coffin, "Low-cycle fatigue damage mechanisms at high temperature," in *Fatigue mechanisms*, ASTM International, 1979.

[75] J. Barsom, "Corrosion-fatigue crack propagation below kiscc," *Engineering Fracture Mechanics*, vol. 3, no. 1, pp. 15 – 25, 1971.

[76] D. E. Gücer and M. Çapa, "Frequency effects in low-cycle fatigue," *Metallurgical Transactions*, vol. 1, pp. 3075–3081, Nov 1970.

[77] L. Freund, J. Hutchinson, and P. Lam, "Analysis of high-strain-rate elastic-plastic crack growth," *Engineering Fracture Mechanics*, vol. 23, no. 1, pp. 119 – 129, 1986.

[78] A. Turnbull, "6.04 - environment-assisted fatigue in liquid environments," in *Comprehensive Structural Integrity* (I. Milne, R. O. Ritchie, and B. Karihaloo, eds.), pp. 163 – 210, Oxford: Pergamon, 2003.

[79] J. C. Amazigo and J. W. Hutchinson, "Crack-tip fields in steady crack-growth with linear strain-hardening," *Journal of the Mechanics and Physics of Solids*, vol. 25, no. 2, pp. 81–97, 1977.

[80] M. Hussain, S. Pu, and J. Underwood, "Strain energy release rate for a crack under combined mode i and mode ii," in *Fracture analysis: Proceedings of the 1973 national symposium on fracture mechanics, part II*, ASTM International, 1974.

[81] M. Hall, "An alternative to the shoji crack tip strain rate equation," *Corrosion Science*, vol. 50, no. 10, pp. 2902 – 2905, 2008.

[82] Q. Peng, J. Kwon, and T. Shoji, "Development of a fundamental crack tip strain rate equation and its application to quantitative prediction of stress corrosion cracking of stainless steels in high temperature oxygenated water," *Journal of Nuclear Materials*, vol. 324, no. 1, pp. 52 – 61, 2004.

[83] B. Lu, "Further study on crack growth model of buried pipelines exposed to concentrated carbonate–bicarbonate solution," *Engineering Fracture Mechanics*, vol. 131, pp. 296 – 314, 2014.

[84] L. M. Young, P. L. Andresen, T. M. Angeliu, *et al.*, "Crack tip strain rate: estimates based on continuum theory and experimental measurement," in *CORROSION 2001*, NACE International, 2001.

[85] B. Moran and C. Shih, "Crack tip and associated domain integrals from momentum and energy balance," *Engineering Fracture Mechanics*, vol. 27, no. 6, pp. 615 – 642, 1987.

[86] M. Gupta, R. Alderliesten, and R. Benedictus, "A review of t-stress and its effects in fracture mechanics," *Engineering Fracture Mechanics*, vol. 134, pp. 218 – 241, 2015.

[87] N. O'Dowd and C. Shih, "Family of crack-tip fields characterized by a triaxiality parameter—i. structure of fields," *Journal of the Mechanics and Physics of Solids*, vol. 39, no. 8, pp. 989 – 1015, 1991.

[88] R. N. Parkins, "A review of stress corrosion cracking of high pressure gas pipelines," *Corrosion 2000*, no. 00363, pp. 1 – 23, 2000.

[89] X. Chen, C. Du, X. Li, and Y. Huang, "Effects of cathodic potential on the local electrochemical environment under a disbonded coating," *Journal of Applied Electrochemistry*, vol. 39, no. 5, pp. 697 – 704, 2009.

[90] W. Chen, S.-H. Wang, F. King, T. R. Jack, and M. J. Wilmott, "Hydrogen permeation behavior of X-70 pipeline steel in a near-neutral pH soil environment," in *2000 3rd International Pipeline Conference*, pp. V002T06A038–V002T06A038, American Society of Mechanical Engineers, 2000.

[91] J. A. Beavers and B. A. Harle, "Mechanisms of high-pH and near-neutral-pH SCC [stress corrosion cracking] of underground pipelines," *Journal of Offshore Mechanics and Arctic Engineering*, vol. 123, no. 3, pp. 147 – 151, 2001.

[92] A. Eslami, R. Kania, B. Worthingham, G. V. Boven, R. Eadie, and W. Chen, "Effect of CO_2 and R-ratio on near-neutral pH stress corrosion cracking initiation under a disbonded coating of pipeline steel," *Corrosion Science*, vol. 53, pp. 2318 – 2327, 2011.

[93] C. Patel, "The influence of sulphate, chloride and nitrate anions on the cyclic strain-enhanced dissolution behaviour of mild steel," *Corrosion Science*, vol. 21, no. 2, pp. 145 – 158, 1981.

[94] A. Turnbull and D. Ferriss, "Mathematical modelling of the electrochemistry in corrosion fatigue cracks in steel corroding in marine environments," *Corrosion Science*, vol. 27, no. 12, pp. 1323 – 1350, 1987.

[95] G. V. Boven, W. Chen, and R. Rogge, "The role of residual stress in neutral pH stress corrosion cracking of pipeline steels. Part I: Pitting and cracking occurrence.," *Acta Materialia*, vol. 55, pp. 29 – 42, 2007.

[96] W. Chen, G. Van Boven, and R. Rogge, "The role of residual stress in neutral pH stress corrosion cracking of pipeline steels – Part II: Crack dormancy," *Acta Materialia*, vol. 55, pp. 43 – 53, 2007.

[97] G. Wranglen, "Pitting and sulphide inclusions in steel," *Corrosion Science*, vol. 14, no. 5, pp. 331–349, 1974.

[98] M. Elboujdaini and R. W. Revie, "Metallurgical factors in stress corrosion cracking (SCC) and hydrogen-induced cracking (HIC)," *Journal of Solid State Electrochemistry*, vol. 13, no. 7, p. 1091, 2009.

[99] R. Sutherby and W. Chen, "Deflected stress corrosion cracks in the pipeline steel," in *2004 International Pipeline Conference*, pp. 113–121, American Society of Mechanical Engineers, 2004.

[100] M. P. Brongers, J. A. Beavers, C. E. Jaske, and B. S. Delanty, "Influence of line-pipe steel metallurgy on ductile tearing of stress-corrosion cracks during simulated hydrostatic testing," in *2000 3rd International Pipeline Conference*, pp. V002T06A009–V002T06A009, American Society of Mechanical Engineers, 2000.

[101] M. Javidi and S. B. Horeh, "Investigating the mechanism of stress corrosion cracking in near-neutral and high ph environments for {API} 5l {X52} steel," *Corrosion Science*, vol. 80, pp. 213 – 220, 2014.

[102] G. Liang, X. Peng, E. S. Juan, and Y. F. Cheng, "Strain aging of x100 steel in service and the enhanced susceptibility of pipelines to stress corrosion cracking.," *JOURNAL OF MATERIALS ENGINEERING AND PERFORMANCE*, vol. 22, no. 12, pp. 3778 – 3782, 2013.

[103] H. K. D. H. Bhadeshia, "Prevention of hydrogen embrittlement in steels," *ISIJ international*, vol. 56, no. 1, pp. 24–36, 2016.

[104] A. Torres-Islas, J. Gonzalez-Rodriguez, J. Uruchurtu, and S. Serna, "Stress corrosion cracking study of microalloyed pipeline steels in dilute $NaHCO_3$ solutions," *Corrosion Science*, vol. 50, pp. 2831 – 2839, 2008.

[105] R. Ritchie and S. Suresh, "Some considerations on fatigue crack closure at near-threshold stress intensities due to fracture surface morphology," *Metallurgical and Materials Transactions A*, vol. 13, no. 5, pp. 937–940, 1982.

[106] J. A. Beavers, J. T. Johnson, and R. L. Sutherby, "Materials factors influencing the initiation of near-neutral ph scc on underground pipelines," in *2000 3rd International Pipeline Conference*, pp. V002T06A041–V002T06A041, American Society of Mechanical Engineers, 2000.

[107] A. Turnbull, "The environmentally small/short crack growth effect: current understanding," *Corrosion Reviews*, vol. 30, no. 1-2, pp. 1–17, 2012.

[108] R. Eadie, L. W. Hunt, R. Sutherby, G. Roy, G. Shen, J. Luo, W. Chen, T. C. Hamré, F. King, and T. Jack, "Long seam welds in gas and liquids pipelines and near-neutral pH stress corrosion cracking and corrosion fatigue," in *4th ASME International Pipeline Conference [IPC] (Calgary, Alberta, 9/29/2002-10/3/2002) Proceedings*, no. IPC2002-27118, 2002.

[109] P. L. Andresen and M. M. Morra, "Effect of rising and falling k profiles on scc growth rates in high-temperature water," *Journal of pressure vessel technology*, vol. 129, no. 3, pp. 488–506, 2007.

[110] G. Van Boven, R. Rogge, and W. Chen, "Residual stress and stress corrosion cracking of high pressure hydrocarbon transmission pipelines," in *2006 International Pipeline Conference*, pp. 725–742, American Society of Mechanical Engineers, 2006.

[111] W. Chen, S. H. Wang, R. Chu, F. King, T. R. Jack, and R. R. Fessler, "Effect of precyclic loading on stress-corrosion-cracking initiation in an X-65 pipeline steel exposed to near-neutral pH soil environment," *Metallurgical and Materials Transactions A*, vol. 34A, no. 11, pp. 2601 – 2608, 2003.

[112] D. He, W. Chen, J. Luo, F. King, T. Jack, and K. Krist, "Effect of surface scratch roughness and orientation on the development of scc of line pipe steel in near neutral ph environment," in *2000 3rd International Pipeline Conference*, pp. V002T06A043–V002T06A043, American Society of Mechanical Engineers, 2000.

[113] D. Najjar, T. Magnin, and T. Warner, "Influence of critical surface defects and localized competition between anodic dissolution and hydrogen effects during stress corrosion cracking of a 7050 aluminium alloy," *Materials Science and Engineering: A*, vol. 238, no. 2, pp. 293 – 302, 1997.

[114] D. A. Jones, "A unified mechanism of stress corrosion and corrosion fatigue cracking," *Metallurgical Transactions A*, vol. 16, pp. 1133–1141, Jun 1985.

[115] T. Magnin, R. Chieragatti, and R. Oltra, "Mechanism of brittle fracture in a ductile 316 alloy during stress corrosion," *Acta Metallurgica et Materialia*, vol. 38, no. 7, pp. 1313 – 1319, 1990.

[116] N. Nanninga, A. Slifka, Y. Levy, and C. White, "A review of fatigue crack growth for pipeline steels exposed to hydrogen," *Journal of research of the National Institute of Standards and Technology*, vol. 115, no. 6, p. 437, 2010.

[117] A. Krom, R. Koers, and A. Bakker, "Hydrogen transport near a blunting crack tip," *Journal of the Mechanics and Physics of Solids*, vol. 47, no. 4, pp. 971 – 992, 1999.

[118] A. Díaz, J. Alegre, and I. Cuesta, "A review on diffusion modelling in hydrogen related failures of metals," *Engineering Failure Analysis*, vol. 66, pp. 577 – 595, 2016.

[119] W. Chen, R. Kania, B. Worthingham, and S. Kariyawasam, "Role of hydrogen in crack growth in pipeline steels exposed to near neutral ph soil environments," in *ICF12, Ottawa 2009*, 2013.

[120] P. Sofronis and R. M. McMeeking, "Numerical analysis of hydrogen transport near a blunting crack tip," *Journal of the Mechanics and Physics of Solids*, vol. 37, pp. 317 – 350, 1989.

[121] J. Song and W. Curtin, "Atomic mechanism and prediction of hydrogen embrittlement in iron," *Nature materials*, vol. 12, no. 2, p. 145, 2013.

[122] X. Xing, M. Yu, O. Tehinse, W. Chen, and H. Zhang, "The effects of pressure fluctuations on hydrogen embrittlement in pipeline steels," in *2016 11th International Pipeline Conference*, p. V001T03A025, American Society of Mechanical Engineers, 2016.

[123] X. Xing, W. Chen, and H. Zhang, "Atomistic study of hydrogen embrittlement during cyclic loading: Quantitative model of hydrogen accumulation effects," *International Journal of Hydrogen Energy*, vol. 42, no. 7, pp. 4571 – 4578, 2017.

[124] X. Xing, M. Yu, W. Chen, and H. Zhang, "Atomistic simulation of hydrogen-assisted ductile-to-brittle transition in α-iron," *Computational Materials Science*, vol. 127, pp. 211 – 221, 2017.

[125] G. Pressouyre, "A classification of hydrogen traps in steel," *Metallurgical Transactions A*, vol. 10, no. 10, pp. 1571–1573, 1979.

[126] P. Cotterill and J. King, "Hydrogen embrittlement contributions to fatigue crack growth in a structural steel," *International Journal of Fatigue*, vol. 13, no. 6, pp. 447 – 452, 1991.

[127] G. Pressouyre, "Hydrogen traps, repellers, and obstacles in steel; consequences on hydrogen diffusion, solubility, and embrittlement," *Metallurgical transactions A*, vol. 14, no. 10, pp. 2189–2193, 1983.

[128] J. P. Hirth, "Effects of hydrogen on the properties of iron and steel," *Metallurgical Transactions A*, vol. 11, no. 6, pp. 861–890, 1980.

[129] D. Dautovich and S. Floreen, "The stress intensities for slow crack growth in steels containing hydrogen," *Metallurgical transactions*, vol. 4, no. 11, pp. 2627–2630, 1973.

[130] W. Gerberich, X. Chen, M. Kaczorowski, *et al.*, "Crack growth from internal hydrogen—temperature and microstructural effects in 4340 steel," *Metallurgical Transactions A*, vol. 19, no. 5, pp. 1319–1334, 1988.

[131] Y. Yamaguchi, H. Nonaka, and K. Yamakawa, "Effect of hydrogen content on threshold stress intensity factor in carbon steel in hydrogen-assisted cracking environments," *Corrosion*, vol. 53, no. 2, pp. 147–155, 1997.

[132] R. L. Thomas, J. R. Scully, and R. P. Gangloff, "Internal hydrogen embrittlement of ultrahigh-strength aermet 100 steel," *Metallurgical and Materials Transactions A*, vol. 34, no. 2, pp. 327–344, 2003.

[133] R. L. Thomas, D. Li, R. P. Gangloff, and J. R. Scully, "Trap-governed hydrogen diffusivity and uptake capacity in ultrahigh-strength aermet 100 steel," *Metallurgical and Materials Transactions A*, vol. 33, no. 7, pp. 1991–2004, 2002.

[134] Z. Y. Liu, C. F. Dong, X. G. Li, Q. Zhi, and Y. F. Cheng, "Stress corrosion cracking of 2205 duplex stainless steel in H_2S–CO_2 environment," *Journal of Materials Science*, vol. 44, no. 16, pp. 4228 – 4234, 2009.

[135] M. Stevens and I. Bernstein, "The role of aging reactions in the hydrogen embrittlement susceptibility of an hsla steel," *Metallurgical Transactions A*, vol. 16, no. 10, pp. 1879–1886, 1985.

[136] W. Chen and S.-h. Wang, "Room temperature creep behaviour of pipeline steels and its influence on stress corrosion cracking," in *2002 4th International Pipeline Conference*, pp. 1895–1902, American Society of Mechanical Engineers, 2002.

[137] S. del Busto, C. Betegón, and E. Martínez-Pañeda, "A cohesive zone framework for environmentally assisted fatigue," *Engineering Fracture Mechanics*, vol. 185, pp. 210 – 226, 2017. XVIII International Colloquium Mechanical Fatigue of Metals.

[138] M. Dadfarnia, M. L. Martin, A. Nagao, P. Sofronis, and I. M. Robertson, "Modeling hydrogen transport by dislocations," *Journal of the Mechanics and Physics of Solids*, vol. 78, pp. 511 – 525, 2015.

[139] L. Jemblie, V. Olden, and O. Akselsen, "A coupled diffusion and cohesive zone modelling approach for numerically assessing hydrogen embrittlement of steel structures," *International Journal of Hydrogen Energy*, vol. 42, no. 16, pp. 11980 – 11995, 2017.

[140] A. Turnbull, "Perspectives on hydrogen uptake, diffusion and trapping," *International Journal of Hydrogen Energy*, vol. 40, no. 47, pp. 16961 – 16970, 2015. Special issue on 1st International Conference on Hydrogen Storage, Embrittlement and Applications (Hy-SEA 2014), 26-30 October 2014, Rio de Janeiro, Brazil.

[141] J. Toribio, "The role of crack tip strain rate in hydrogen assisted cracking," *Corrosion Science*, vol. 39, no. 9, pp. 1687 – 1697, 1997.

[142] G. R. Engelhardt and D. D. Macdonald, "Modelling the crack propagation rate for corrosion fatigue at high frequency of applied stress," *Corrosion Science*, vol. 52, no. 4, pp. 1115 – 1122, 2010.

[143] A. Turnbull, "Modeling of the chemistry and electrochemistry in cracks—a review," *CORROSION*, vol. 57, no. 2, pp. 175–189, 2001.

[144] D. W. Engel, "Investigation of surface crack growth behaviour under variable pressure fluctuations in near-neutral pH environments."

[145] A. Egbewande, W. Chen, R. Eadie, R. Kania, G. V. Boven, R. Worthingham, and J. Been, "Surface crack growth behavior of pipeline steel under disbonded coating at free corrosion potential in near-neutral pH soil environments," *Metallurgical and Materials Transactions A*, vol. 45A, no. 11, pp. 4946 – 4959, 2014.

[146] C. S. Association, *Oil and gas pipeline systems*. CSA, 7th edition ed., 2015.

[147] A. International, *Standard Practice for Preparing, Cleaning, and Evaluating Corrosion Test Specimens*. ASTM International, 2003.

[148] J. Schindelin, I. Arganda-Carreras, E. Frise, V. Kaynig, M. Longair, T. Pietzsch, S. Preibisch, C. Rueden, S. Saalfeld, B. Schmid, *et al.*, "Fiji: an open-source platform for biological-image analysis," *Nature methods*, vol. 9, no. 7, pp. 676–682, 2012.

[149] S.-H. Wang, Z. Yonggang, and C. Weixing, "Room temperature creep and strain-rate-dependent stress-strain behavior of pipeline steels," *Journal of Materials Science*, vol. 36, no. 8, pp. 1931 – 1938, 2001.

[150] M. Yu, W. Chen, R. Kania, G. Van Boven, and J. Been, "Underload-induced crack growth behaviour of minor cycles of pipeline steel in near-neutral pH environment," *Fatigue and Fracture of Engineering Materials and Structures*, vol. 38, no. 6, pp. 681 – 692, 2015.

[151] W. P. Davey, "Precision measurements of the lattice constants of twelve common metals," *Physical Review*, vol. 25, no. 6, p. 753, 1925.

[152] W. Chen, H. Zhu, and S. H. Wang, "Low temperature creep behaviour of pipeline steels," *Canadian Metallurgical Quarterly*, vol. 48, no. 3, pp. 271 – 283, 2009.

Appendix A

Supporting Data

A.1 Test pH

Table A.1: pH measurements for bulk solution and anode chambers. Results were unavailable for pH measurements following the 10 +CA waveform.

Waveform	Bulk	Anode
10 s ULH	6.29	6.09
30 s ULH	6.42	6.37
60 s ULH	6.26	6.25
250 s ULH	6.11	6.10
500 s ULH	6.47	6.37
10 s +CA	–	–
500 s CA	6.24	6.20
Average	6.30 ± 0.13	6.23 ± 0.12

A.2 Final Dimensions

Table A.2: Final dimensions [µm].

	Final Depth (a)			**Final Length ($2c$)**		
Waveform	**Hydrogen**	**Exposed**	**Air**	**Hydrogen**	**Exposed**	**Air**
10 s ULH	905	917	1013	5325	5502	5515
30 s ULH	1218	1164	1133	5126	5435	5364
60 s ULH	734	387	727	4505	3360	4756
250 s ULH	720	929	897	4501	4994	5297
500 s ULH	670	670	871	4800	4817	5334
10 s +CA	660	660	862	4777	4817	5334
500 s CA	1194	1149	1127	5092	5407	5358

A.3 Plastic Zone Size

Table A.3: Plastic zone sizes based on initial dimensions [µm].

	Depth			**Surface**		
Waveform	**Hydrogen**	**Exposed**	**Air**	**Hydrogen**	**Exposed**	**Air**
10 s ULH	95	98	107	38	39	48
30 s ULH	112	114	112	65	59	58
60 s ULH	77	44	80	29	12	29
250 s ULH	77	96	97	29	43	40
500 s ULH	75	75	95	25	25	38
10 s +CA	71	72	93	22	23	36
500 s CA	104	111	111	52	56	56

A.4 Initial Dimensions relative to Plastic Zone Size

Table A.4: Initial dimensions normalized against respective plastic zone sizes.

	Initial Depth			Initial Length		
Waveform	**Hydrogen**	**Exposed**	**Air**	**Hydrogen**	**Exposed**	**Air**
10 s ULH	9.1	9.0	9.4	55.6	55.9	51.7
30 s ULH	10.6	10.1	10.0	45.5	47.5	47.8
60 s ULH	9.1	8.5	9.0	58.3	76.2	59.4
250 s ULH	9.1	9.6	9.2	58.3	52.1	54.9
500 s ULH	8.8	8.8	9.1	63.9	63.9	56.3
10 s +CA	8.7	8.6	9.0	66.3	66.6	57.2
500 s CA	10.0	9.9	10.0	48.8	48.5	48.3

A.5 Measured Growth

Table A.5: Measured growth at the surface and in the depth [µm].

	Depth Growth (Δa)			Surface Growth ($\Delta(2c)$)		
Waveform	**Hydrogen**	**Exposed**	**Air**	**Hydrogen**	**Exposed**	**Air**
10 s ULH	40	32	14	37	32	9
30 s ULH	27	18	7	34	29	6
60 s ULH	36	17	9	41	26	13
250 s ULH	20	10	7	28	0	2
500 s ULH	15	10	7	23	0	0
10 s +CA	44	41	22	101	47	18
500 s CA	154	47	22	29	29	10

A.6 Crack Growth Rates

Table A.6: Growth per block at the surface and in the depth [µm/cycle]. Note that growth at the surface is per side, not the total length.

	Depth CGR (da/dN)			**Surface CGR (dc/dN)**		
Waveform	**Hydrogen**	**Exposed**	**Air**	**Hydrogen**	**Exposed**	**Air**
10 s ULH	0.068	0.055	0.024	0.032	0.027	0.008
30 s ULH	0.061	0.041	0.016	0.039	0.033	0.006
60 s ULH	0.062	0.030	0.016	0.036	0.022	0.011
250 s ULH	0.050	0.025	0.018	0.034	0	0.002
500 s ULH	0.037	0.025	0.018	0.029	0	0
10 s +CA	0.039	0.036	0.020	0.044	0.021	0.008
500 s CA	0.136	0.041	0.019	0.013	0.013	0.004

A.7 Growth Aspect Ratio

Table A.7: Growth aspect ratio $\Delta c/\Delta a$.

Waveform	**Hydrogen**	**Exposed**	**Air**
10 s ULH	0.5	0.5	0.3
30 s ULH	0.6	0.8	0.4
60 s ULH	0.6	0.8	0.7
250 s ULH	0.7	0	0.1
500 s ULH	0.8	0	0
10 s +CA	1.2	0.6	0.4
500 s CA	0.1	0.3	0.2

A.8 Unloading Rate

Table A.8: Unloading rate in the depth and at the surface [$\mathrm{MPa\,m^{0.5}\,s^{-1}}$].

	$dK/dt_{\mathbf{depth}}$			$dK/dt_{\mathbf{surf}}$		
Waveform	**Hydrogen**	**Exposed**	**Air**	**Hydrogen**	**Exposed**	**Air**
10 s ULH	1.71	1.73	1.81	1.08	1.09	1.21
30 s ULH	0.62	0.62	0.62	0.47	0.45	0.44
60 s ULH	0.26	0.19	0.26	0.16	0.10	0.16
250 s ULH	0.06	0.07	0.07	0.04	0.05	0.04
500 s ULH	0.03	0.03	0.03	0.02	0.02	0.02
10 s +CA	1.47	1.48	1.69	0.83	0.83	1.05
500 s CA	0.04	0.04	0.04	0.03	0.03	0.03

Appendix B

Supplementary Crack Images

B.1 Fractography – Full Crack

B.1.1 Sample J2 – 10 s ULH

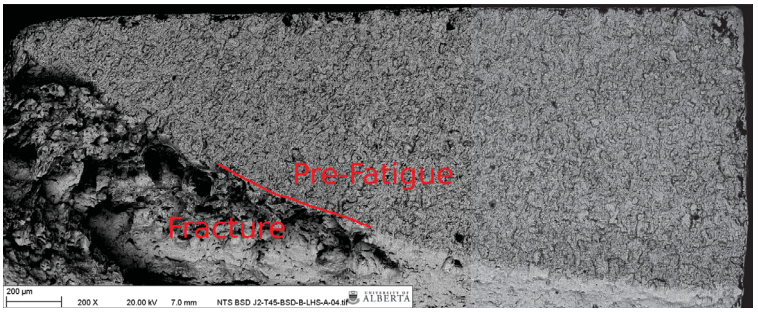

Figure B.1: SEM-BSD micrograph of "Air" fracture surface loaded with 10 s unloading, 500 s ramp, and 1 h static hold.

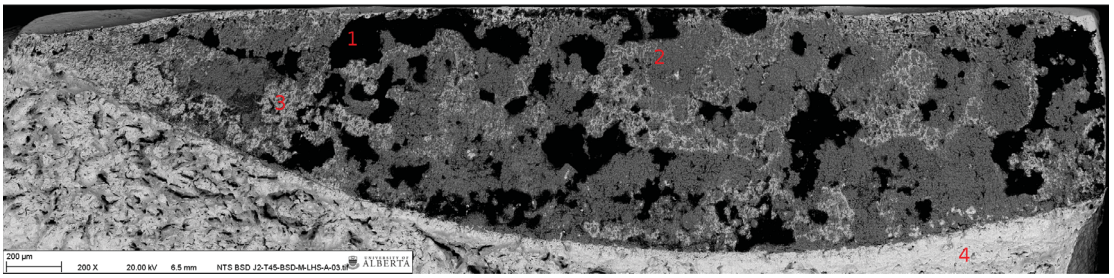

Figure B.2: SEM-BSD micrograph of "Exposed" fracture surface loaded with 10 s unloading, 500 s ramp, and 1 h static hold.

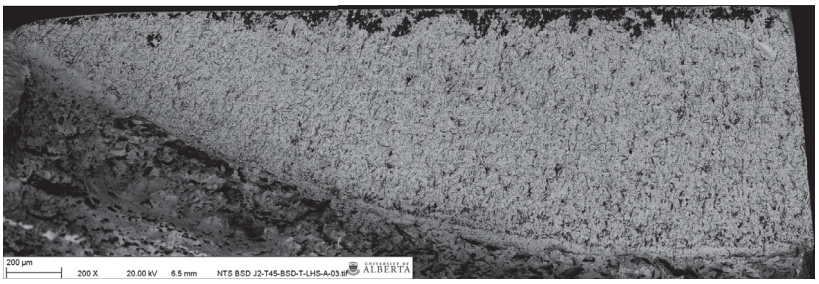

Figure B.3: SEM-BSD micrograph of "Hydrogen" fracture surface loaded with 10 s unloading, 500 s ramp, and 1 h static hold.

B.1.2 Sample J5 – 10 s CA; 500 s ULH

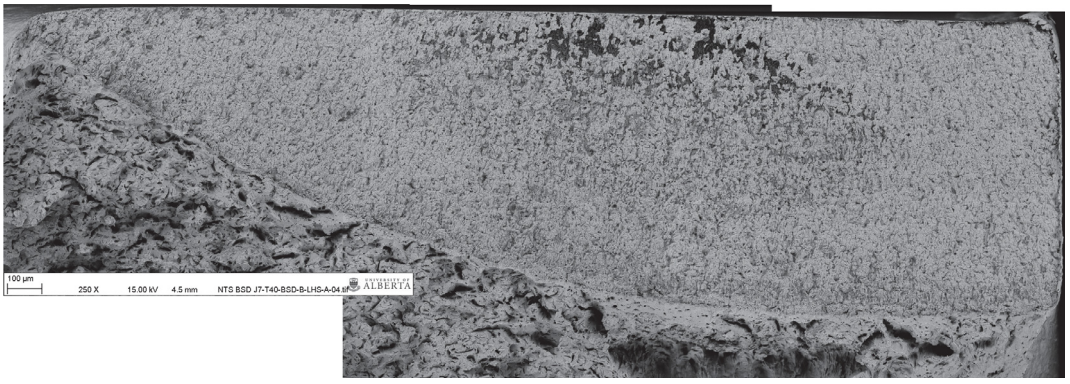

Figure B.4: SEM-BSD micrograph of "Air" fracture surface loaded with 10 s unloading and 500 s constant amplitude loading; subsequent testing with 500 s unloading, 500 s ramp, and 1 h static hold was performed.

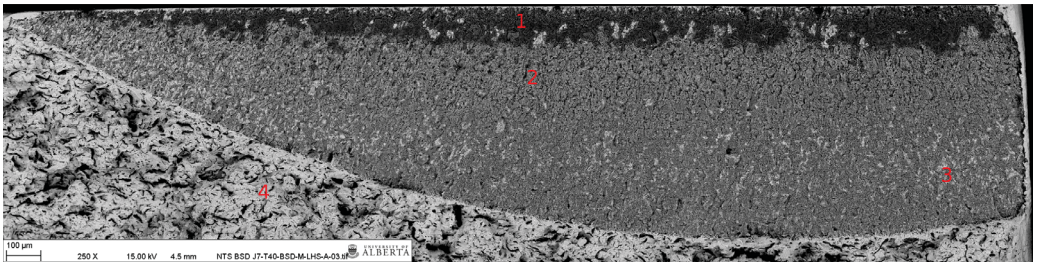

Figure B.5: SEM-BSD micrograph of "Exposed" fracture surface loaded with 10 s unloading and 500 s constant amplitude loading; subsequent testing with 500 s unloading, 500 s ramp, and 1 h static hold was performed.

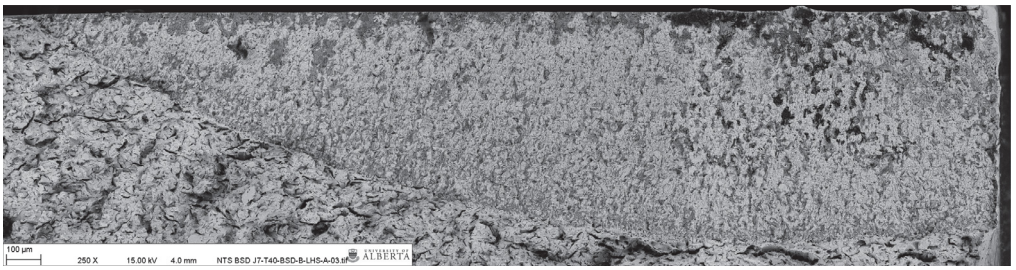

Figure B.6: SEM-BSD micrograph of "Hydrogen" fracture surface loaded with 10 s unloading and 500 s constant amplitude loading; subsequent testing with 500 s unloading, 500 s ramp, and 1 h static hold was performed.

B.1.3 Sample J7 – 500 s CA; 30 s ULH

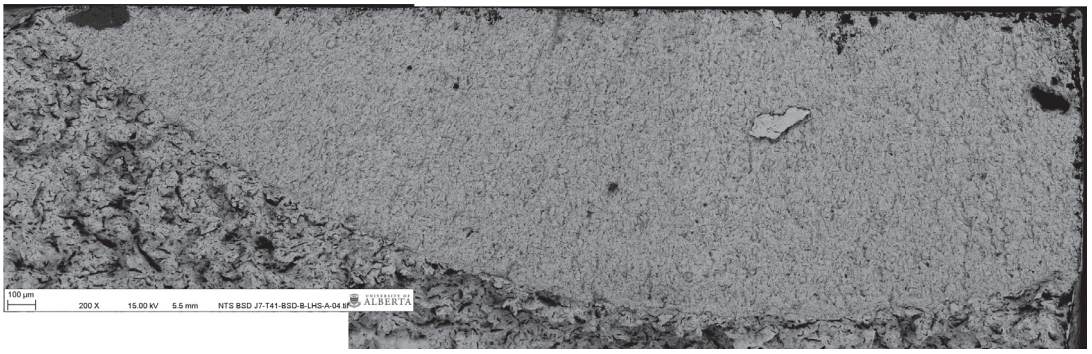

Figure B.7: SEM-BSD micrograph of "Air" fracture surface loaded with 500 s constant amplitude loading; subsequent testing with 30 s unloading, 500 s ramp, and 1 h static hold was performed.

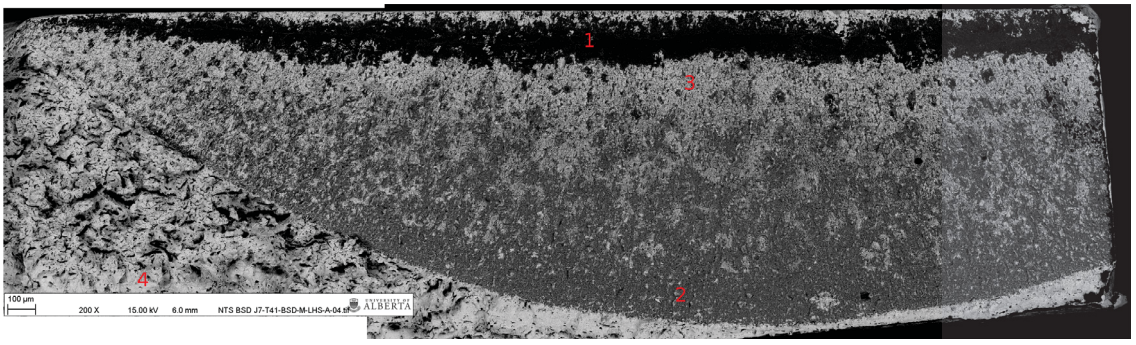

Figure B.8: SEM-BSD micrograph of "Exposed" fracture surface loaded with 500 s constant amplitude loading; subsequent testing with 30 s unloading, 500 s ramp, and 1 h static hold was performed.

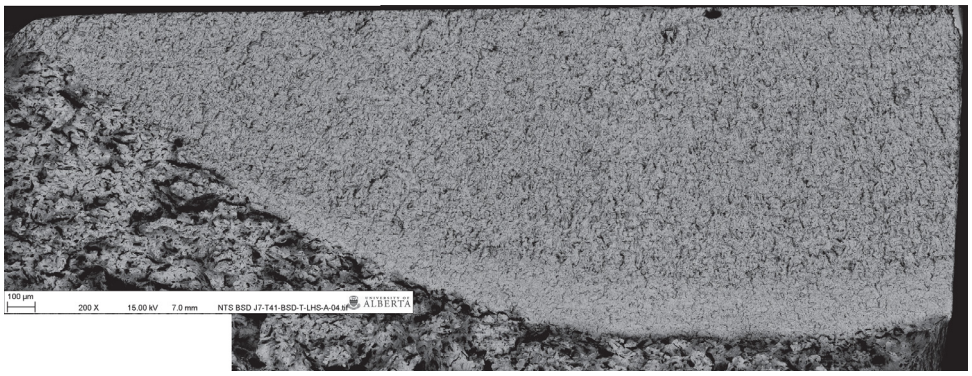

Figure B.9: SEM-BSD micrograph of "Hydrogen" fracture surface loaded with 500 s constant amplitude loading; subsequent testing with 30 s unloading, 500 s ramp, and 1 h static hold was performed.

B.1.4 Sample J9 – 60 s ULH

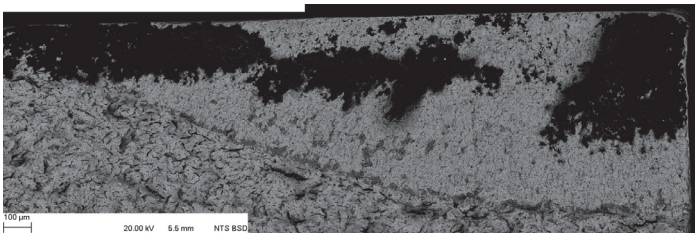

Figure B.10: SEM-BSD micrograph of "Air" fracture surface loaded with 60 s unloading, 500 s ramp, and 1 h static hold.

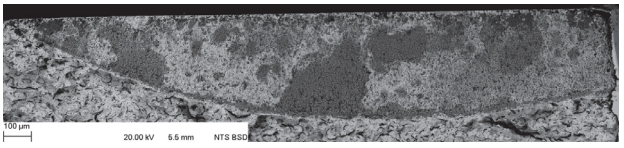

Figure B.11: SEM-BSD micrograph of "Exposed" fracture surface loaded with 60 s unloading, 500 s ramp, and 1 h static hold.

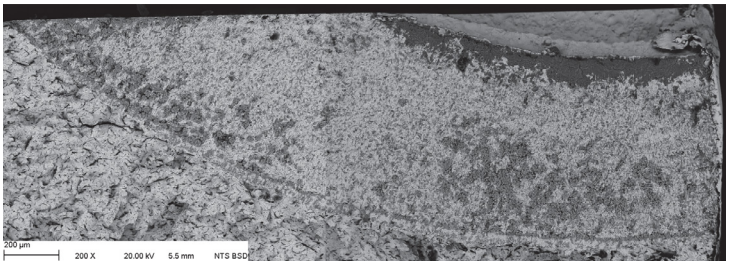

Figure B.12: SEM-BSD micrograph of "Hydrogen" fracture surface loaded with 60 s unloading, 500 s ramp, and 1 h static hold.

B.1.5 Sample J11 – 250 s ULH

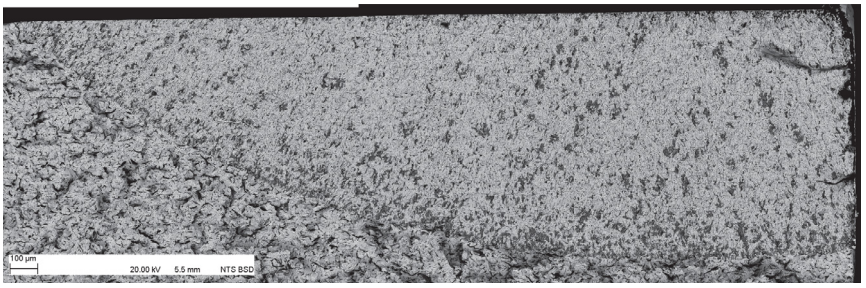

Figure B.13: SEM-BSD micrograph of "Air" fracture surface loaded with 250 s unloading, 500 s ramp, and 1 h static hold.

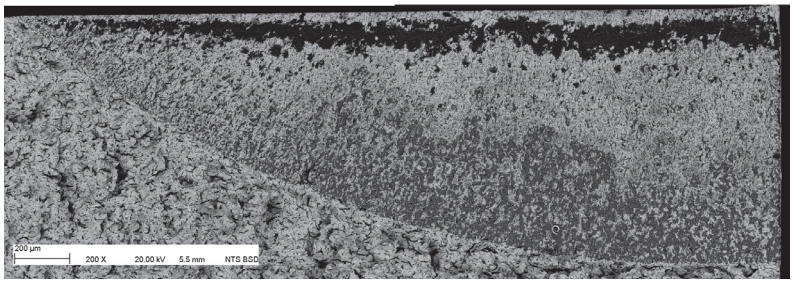

Figure B.14: SEM-BSD micrograph of "Exposed" fracture surface loaded with 250 s unloading, 500 s ramp, and 1 h static hold.

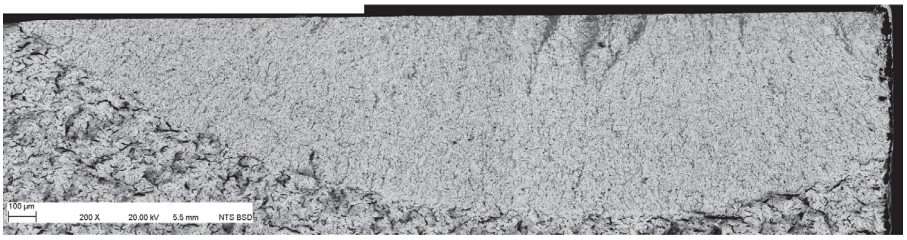

Figure B.15: SEM-BSD micrograph of "Hydrogen" fracture surface loaded with 250 s unloading, 500 s ramp, and 1 h static hold.

B.2 Fractography – Depth Growth Band

B.2.1 Sample J2 – 10 s ULH

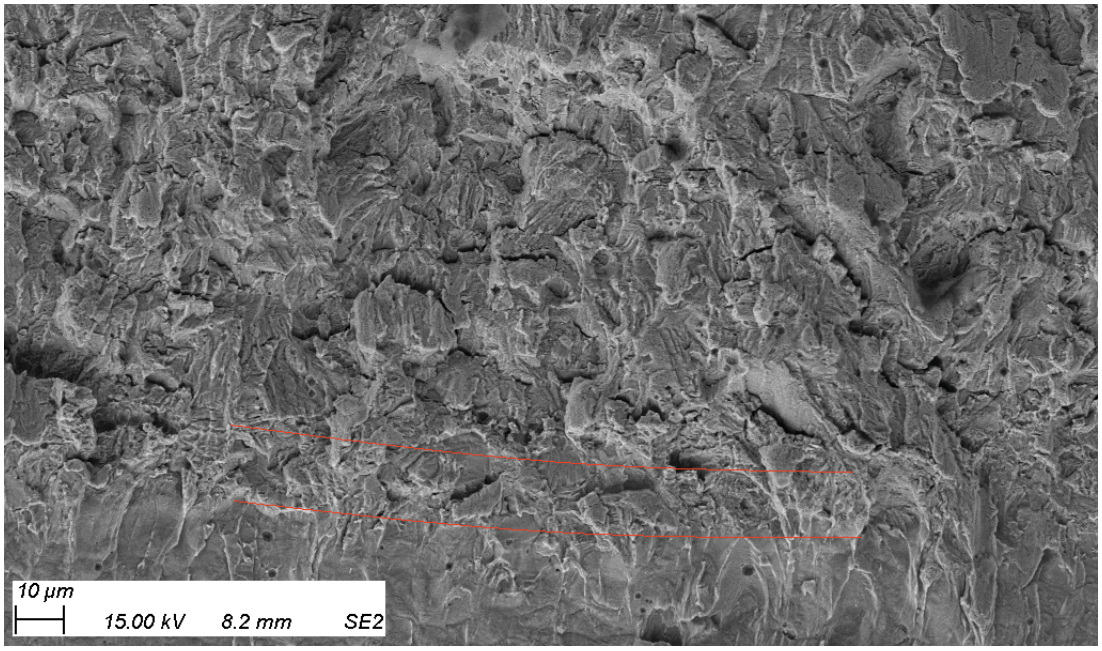

Figure B.16: SEM-SE micrograph of "Air" crack growth band at the depth loaded with 10 s unloading, 500 s ramp, and 1 h static hold. Red lines indicate growth. Micrograph was taken after oxide removal.

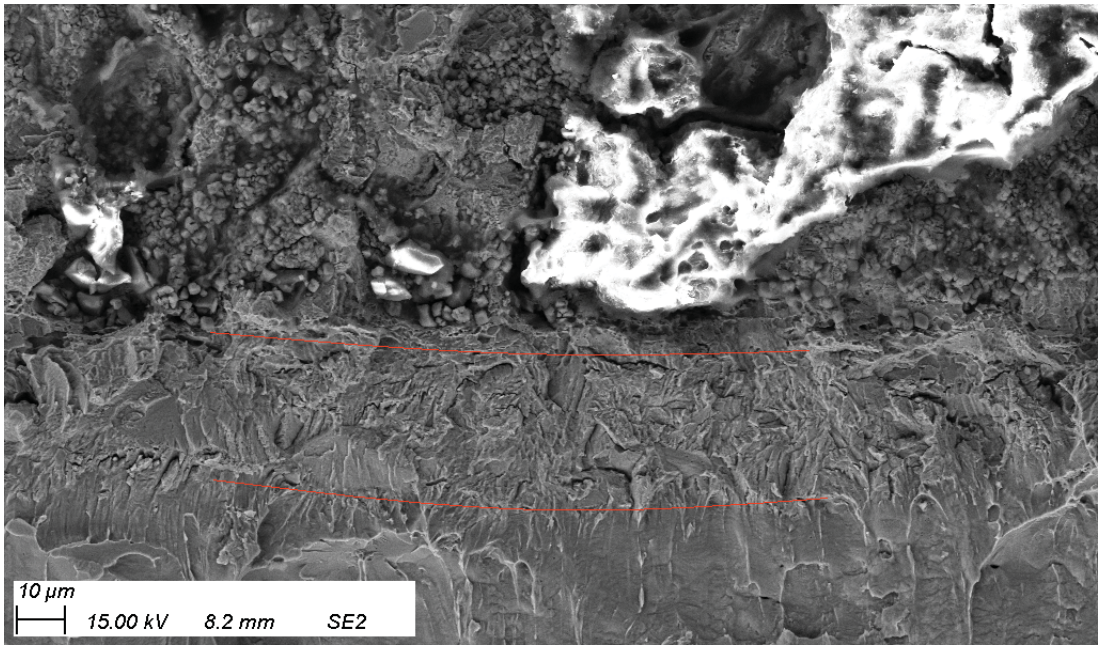

Figure B.17: SEM-SE micrograph of "Exposed" crack growth band at the depth loaded with 10 s unloading, 500 s ramp, and 1 h static hold. Red lines indicate growth. Micrograph was taken after oxide removal.

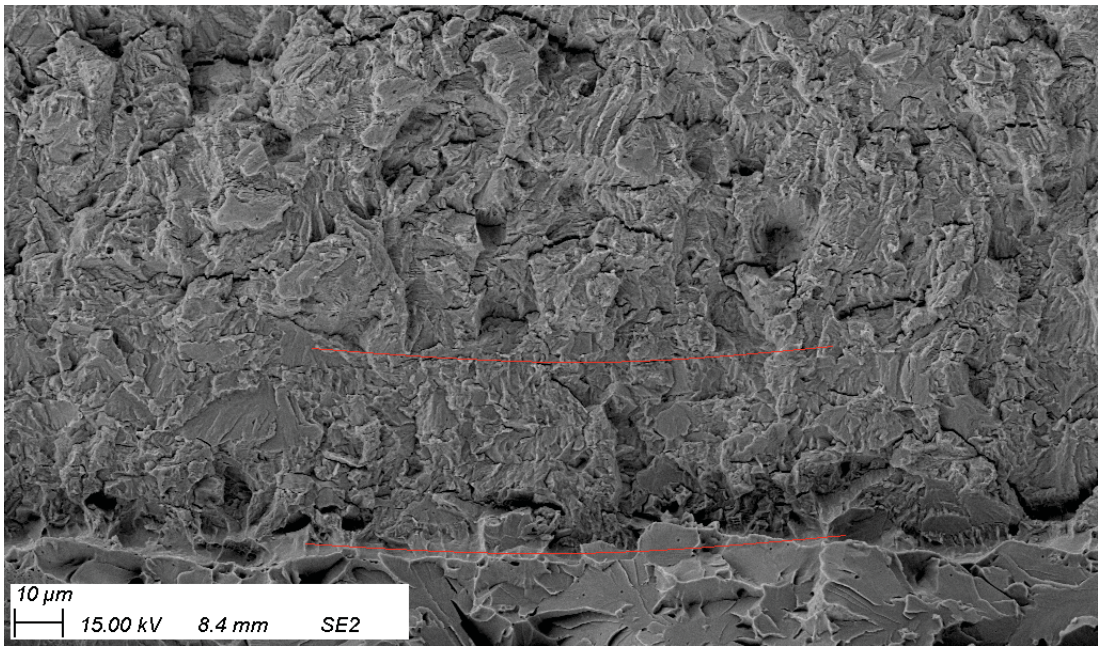

Figure B.18: SEM-SE micrograph of "Hydrogen" crack growth band at the depth loaded with 10 s unloading, 500 s ramp, and 1 h static hold. Red lines indicate growth. Micrograph was taken after oxide removal.

B.2.2 Sample J5 – 10 s CA; 500 s ULH

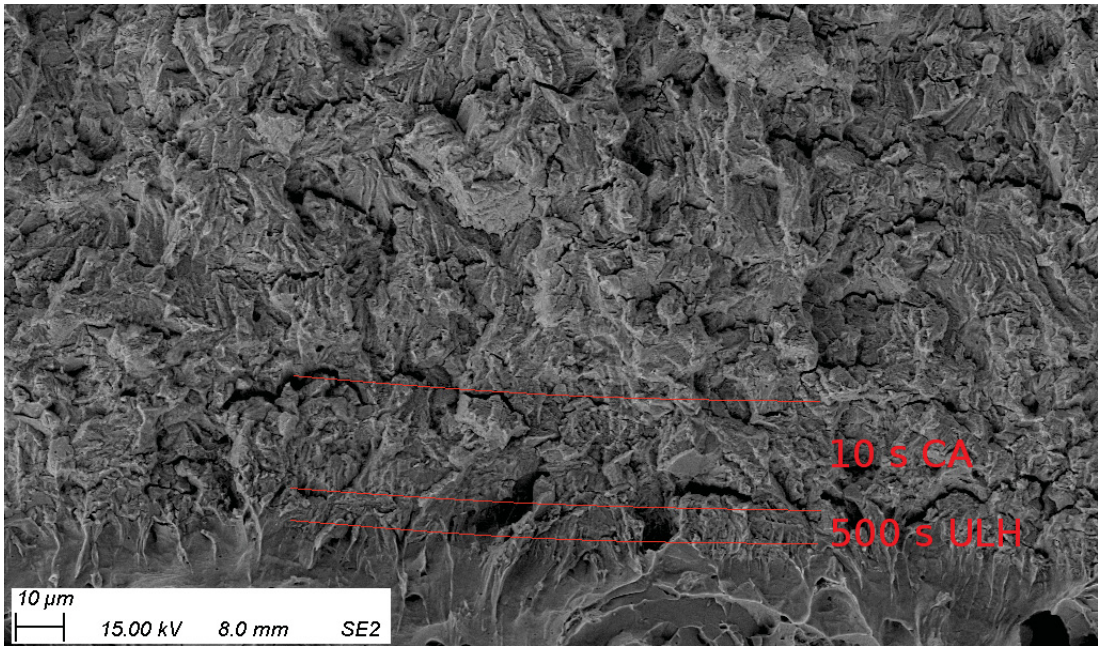

Figure B.19: SEM-SE micrograph of "Air" crack growth band at the depth. Loading conditions are indicated on the image. Red lines indicate growth. Micrograph was taken after oxide removal.

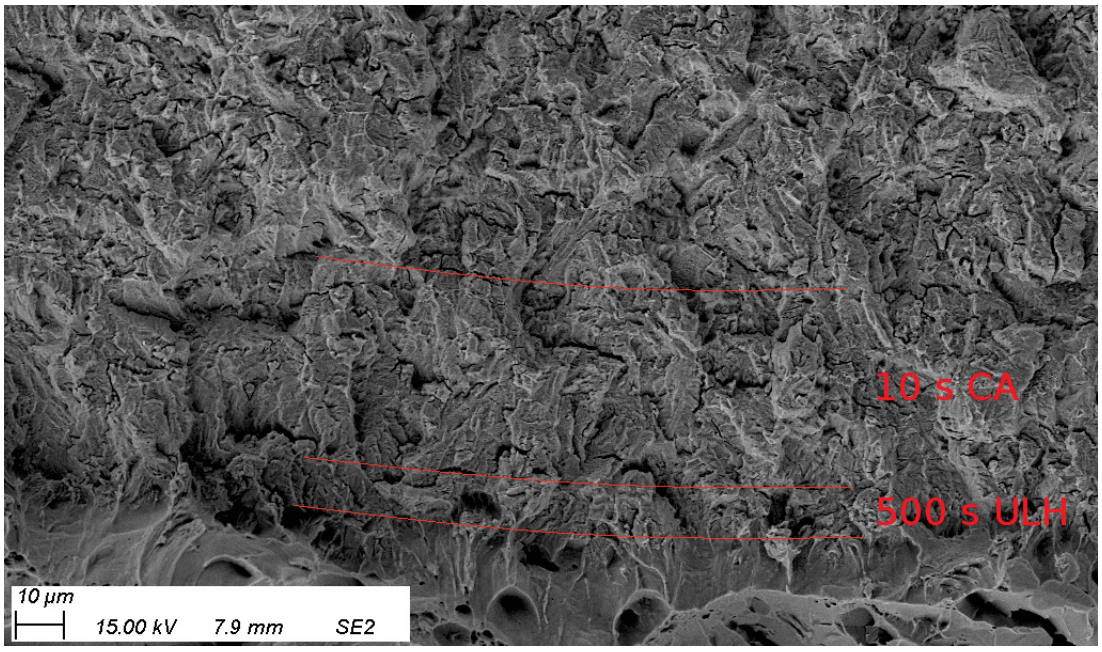

Figure B.20: SEM-SE micrograph of "Exposed" crack growth band at the depth. Loading conditions are indicated on the image. Red lines indicate growth. Micrograph was taken after oxide removal.

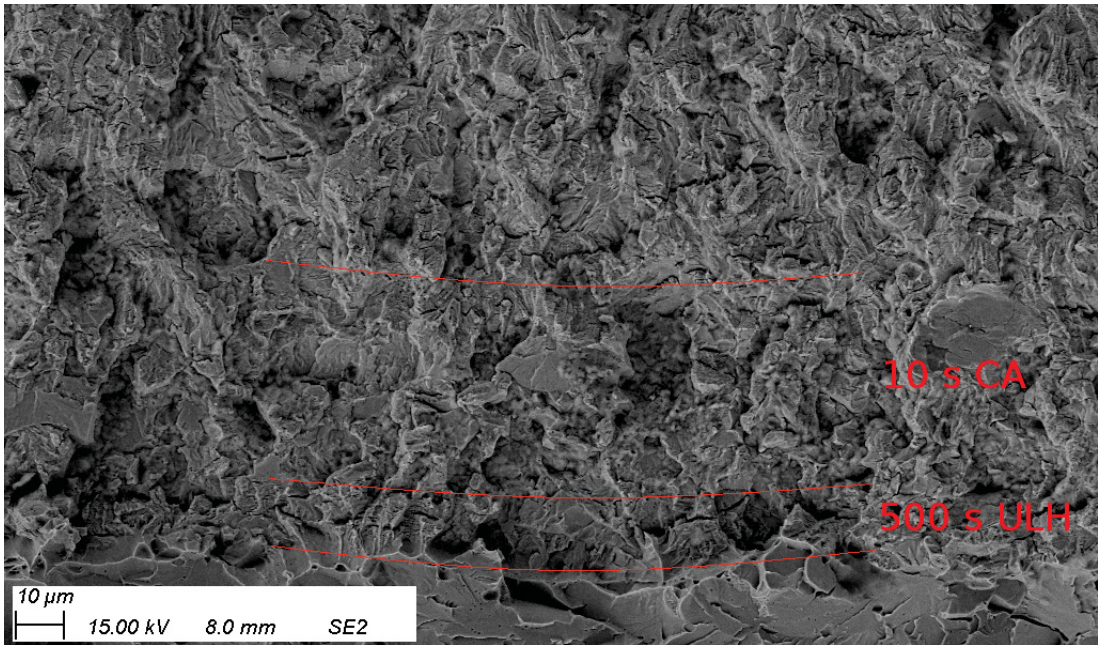

Figure B.21: SEM-SE micrograph of "Hydrogen" crack growth band at the depth. Loading conditions are indicated on the image. Red lines indicate growth. Micrograph was taken after oxide removal.

B.2.3 Sample J7 – 500 s CA; 30 s ULH

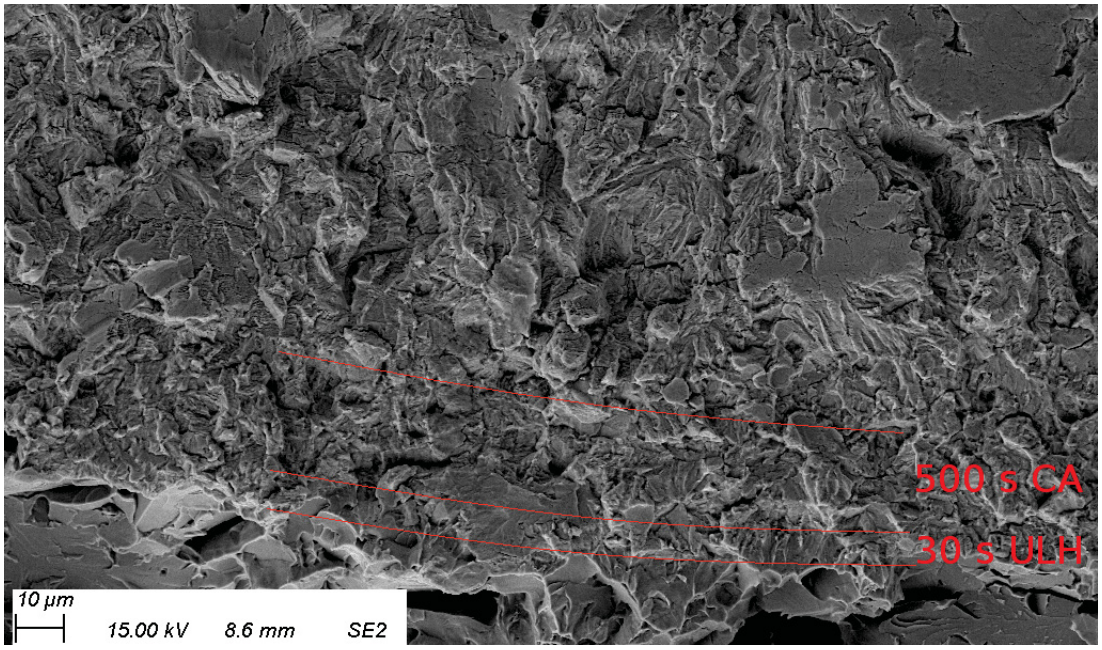

Figure B.22: SEM-SE micrograph of "Air" crack growth band at the depth. Loading conditions are indicated on the image. Red lines indicate growth. Micrograph was taken after oxide removal.

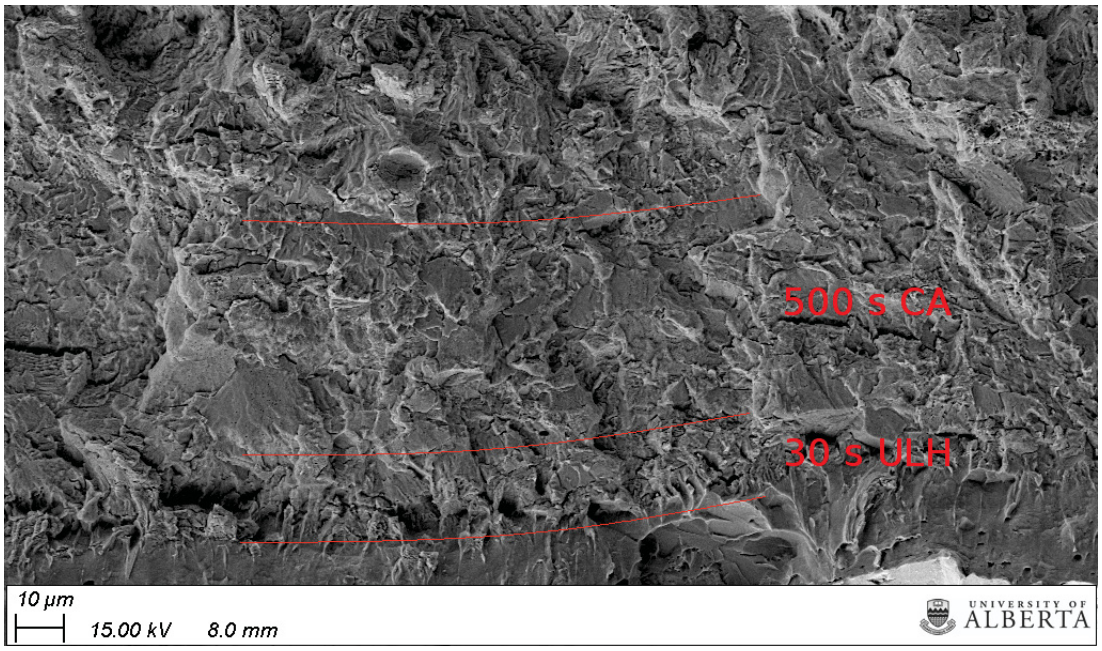

Figure B.23: SEM-SE micrograph of "Exposed" crack growth band at the depth. Loading conditions are indicated on the image. Red lines indicate growth. Micrograph was taken after oxide removal.

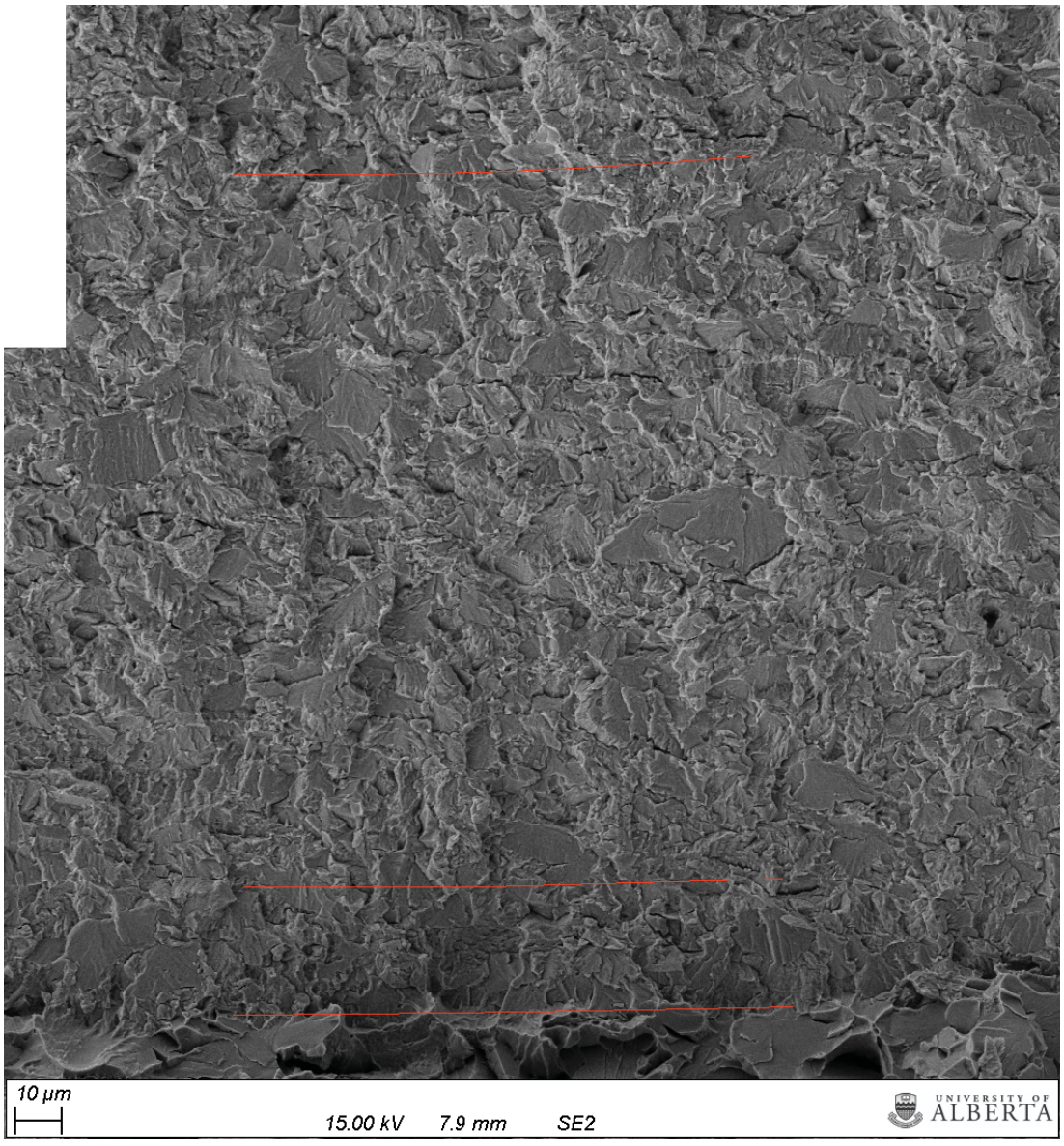

Figure B.24: SEM-SE micrograph of "Hydrogen" crack growth band at the depth. Loading conditions are indicated on the image. Red lines indicate growth. Micrograph was taken after oxide removal.

B.2.4 Sample J9 – 60 s ULH

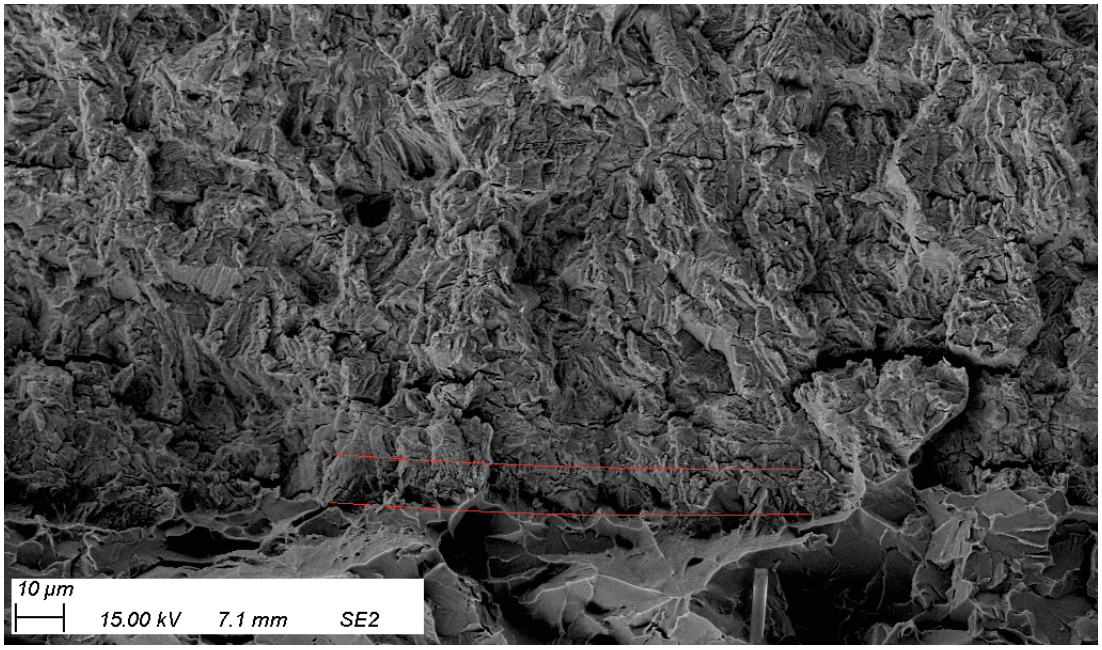

Figure B.25: SEM-SE micrograph of "Air" crack growth band at the depth loaded with 60 s unloading, 500 s ramp, and 1 h static hold. Red lines indicate growth. Micrograph was taken after oxide removal.

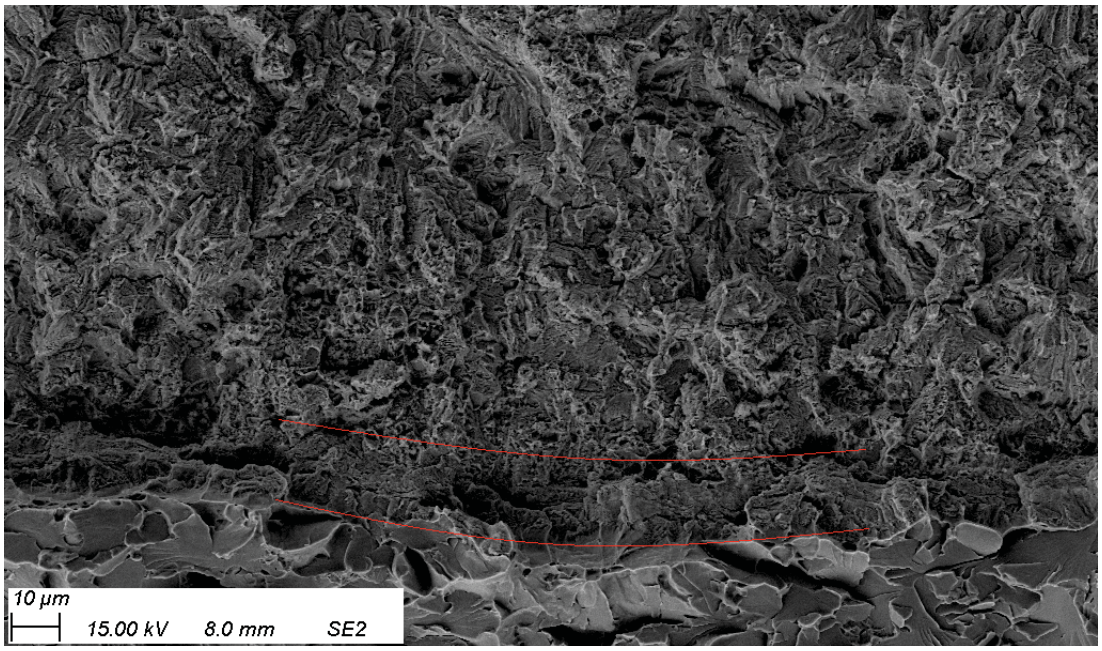

Figure B.26: SEM-SE micrograph of "Exposed" crack growth band at the depth loaded with 60 s unloading, 500 s ramp, and 1 h static hold. Red lines indicate growth. Micrograph was taken after oxide removal.

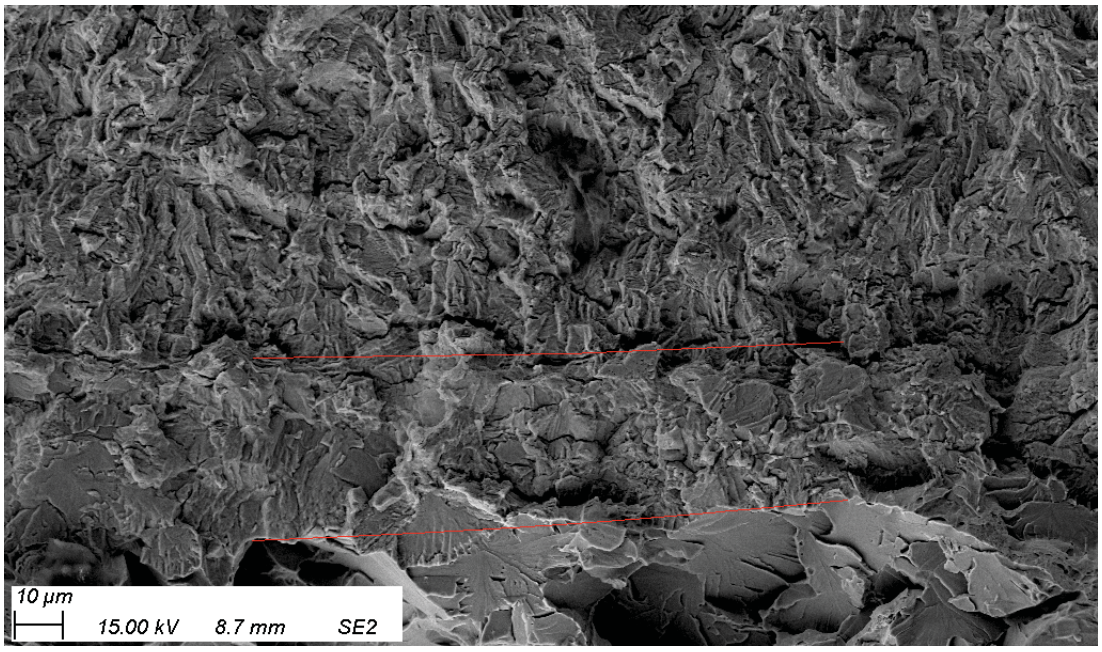

Figure B.27: SEM-SE micrograph of "Hydrogen" crack growth band at the depth loaded with 60 s unloading, 500 s ramp, and 1 h static hold. Red lines indicate growth. Micrograph was taken after oxide removal.

B.2.5 Sample J11 – 250 s ULH

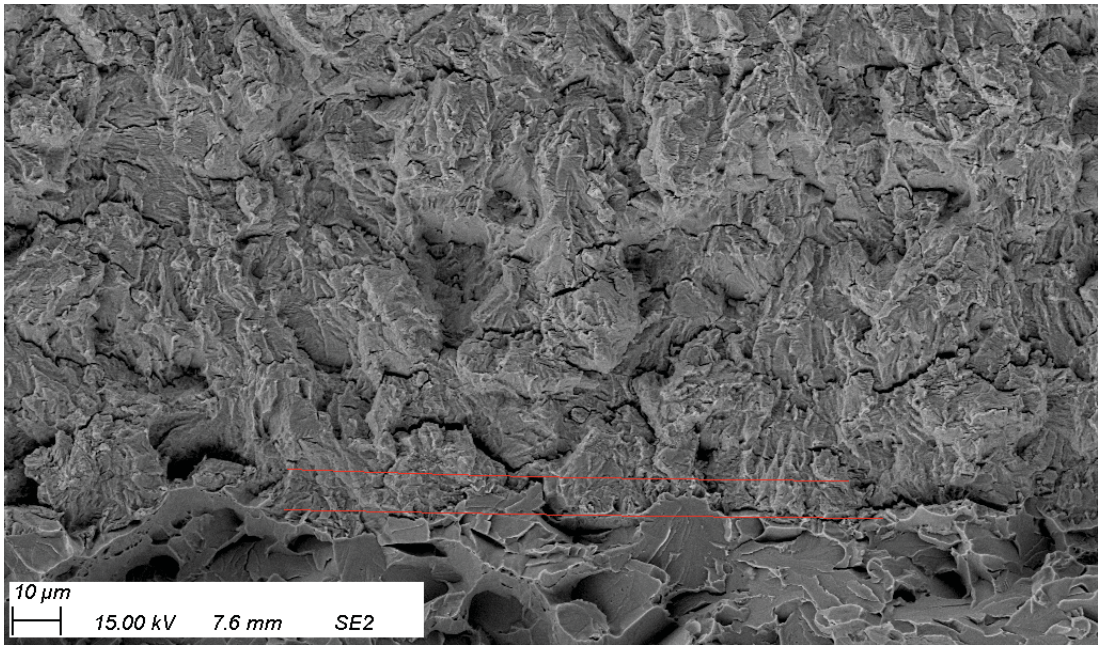

Figure B.28: SEM-SE micrograph of "Air" crack growth band at the depth loaded with 250 s unloading, 500 s ramp, and 1 h static hold. Red lines indicate growth. Micrograph was taken after oxide removal.

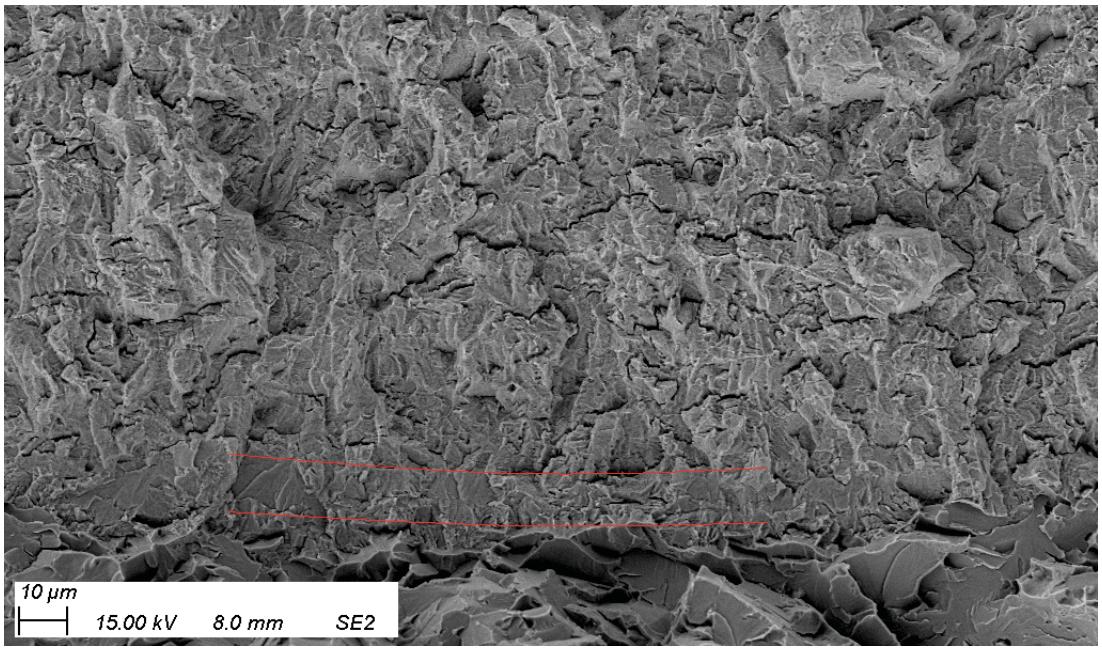

Figure B.29: SEM-SE micrograph of "Exposed" crack growth band at the depth loaded with 250 s unloading, 500 s ramp, and 1 h static hold. Red lines indicate growth. Micrograph was taken after oxide removal.

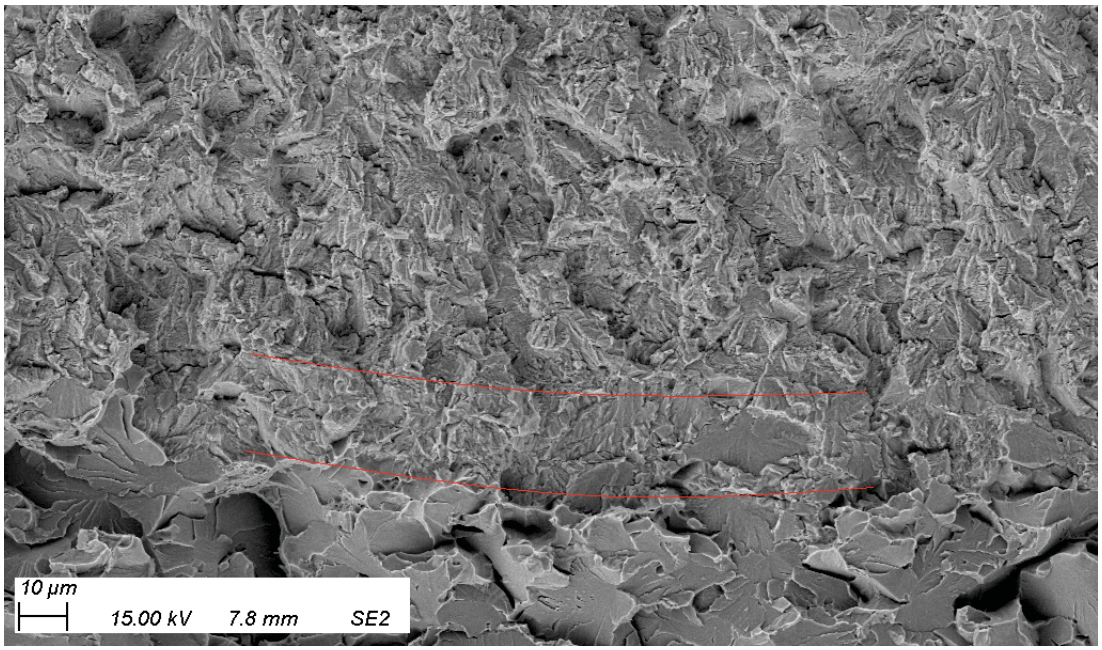

Figure B.30: SEM-SE micrograph of "Hydrogen" crack growth band at the depth loaded with 250 s unloading, 500 s ramp, and 1 h static hold. Red lines indicate growth. Micrograph was taken after oxide removal.

B.3 Depth Profiles

B.3.1 Sample J2 – 10 s ULH

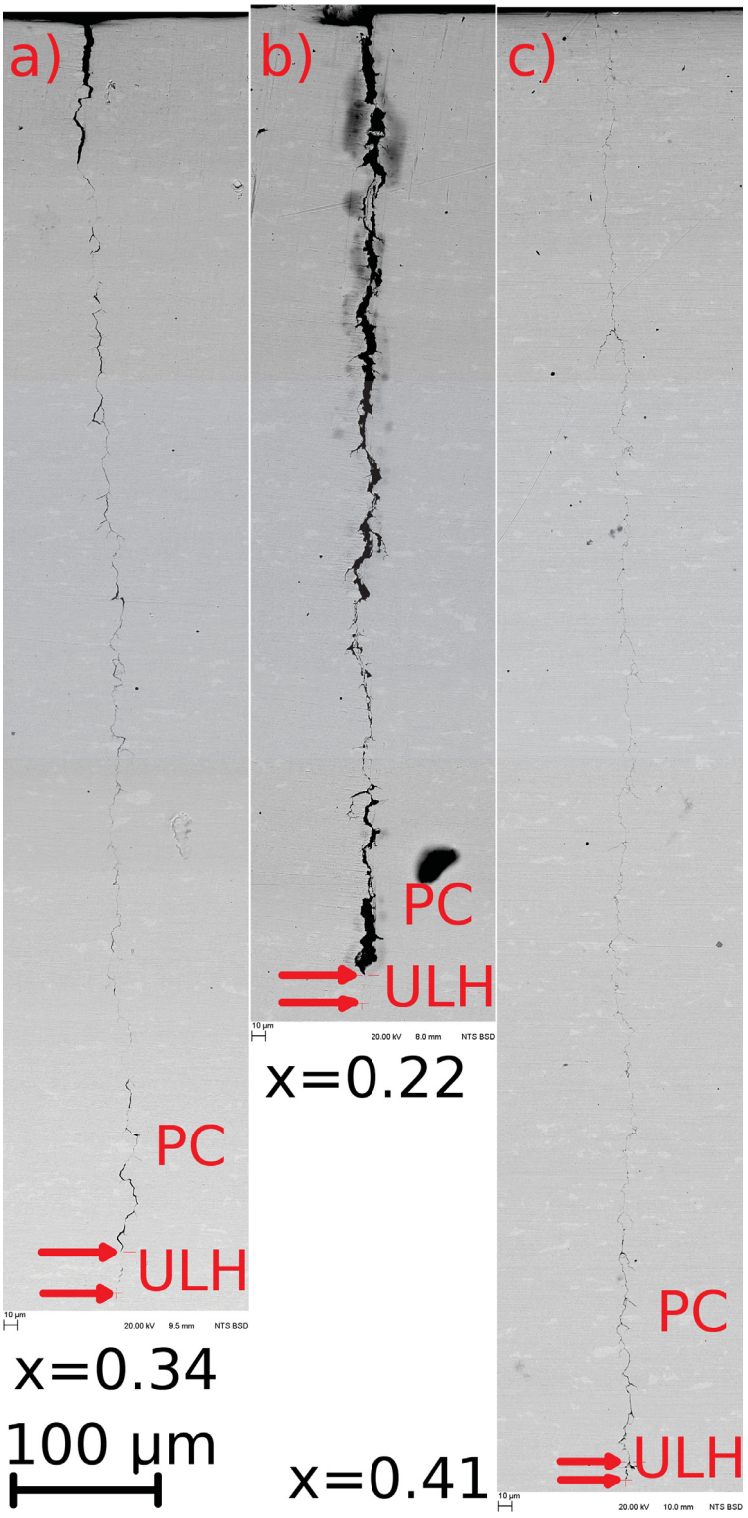

Figure B.31: SEM-BSD micrographs of (a) "Hydrogen", (b) "Exposed", and (c) "Air" crack depth profiles. Red arrows indicate the crack tip corresponding to precracking (PC) and 10 s unloading, 500 s loading, and 1 hour hold (ULH). The approximate length fraction x is indicated beside the corresponding images. Images were taken with an acceleration voltage of 20 kV and working distances were between 8.5 mm and 10.0 mm.

B.3.2 Sample J5 – 10 s CA; 500 s ULH

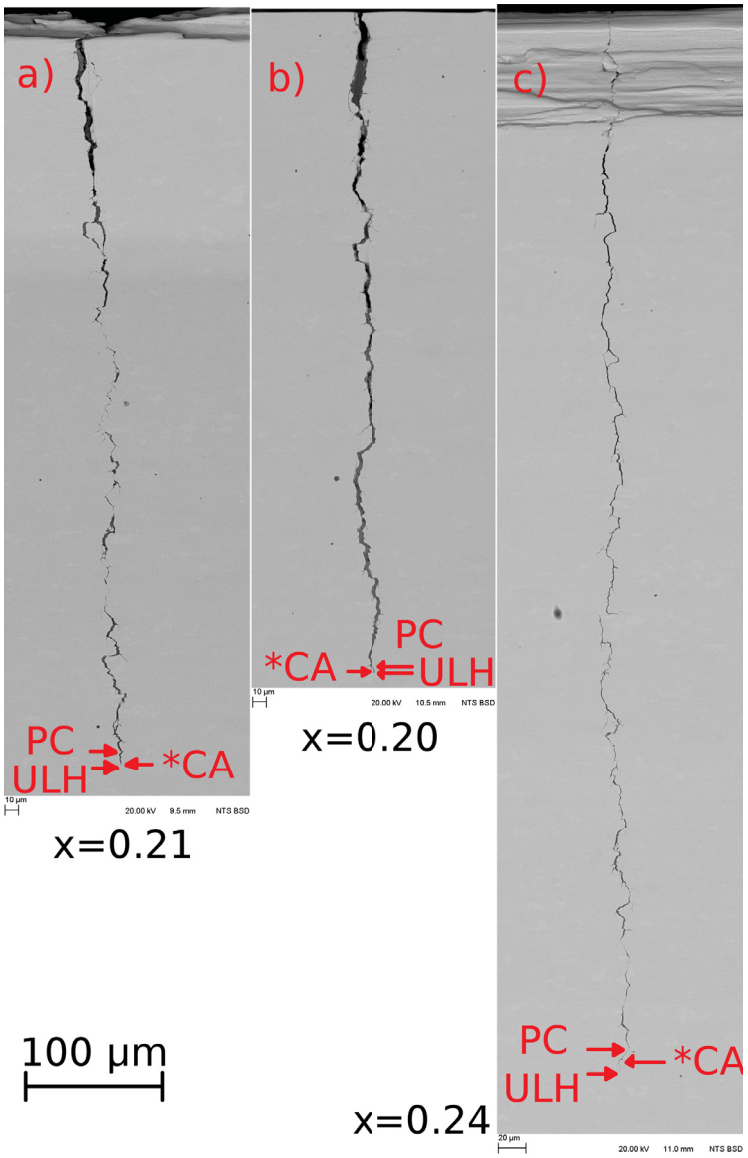

Figure B.32: SEM-BSD micrographs of (a) "Hydrogen", (b) "Exposed", and (c) "Air" crack depth profiles. Red arrows indicate the crack tip corresponding to precracking (PC); 10 s unloading and 500 s loading at constant amplitude (*CA); and 500 s unloading, 500 s loading, and 1 hour hold (ULH). The approximate length fraction x is indicated beside the corresponding images. Images were taken with an acceleration voltage of 20 kV and working distances were between 9.5 mm and 11.0 mm.